Sub-100 µm diameter PEDOT:PSS electrodes on PDMS

David Pieter van der Laan

Delft University of Technology

TU Delft

Sub-100 µm diameter PEDOT:PSS electrodes on PDMS

by

David Pieter van der Laan

to obtain the degree of Master of Science
at the Delft University of Technology,
to be defended publicly on Wednesday July 16, 2025 at 09:00 AM.

Student number:	5131669	
Project duration:	September 1, 2024 – July 16, 2025	
Thesis committee:	Dr. A. Savva,	TU Delft, supervisor
	Dr. M. Mastrangeli,	TU Delft
	Dr. T. G. Costa,	TU Delft

Cover: PEDOT:PSS electrodes and tracks on 8 μm thick PDMS.

An electronic version of this thesis is available at `http://repository.tudelft.nl/`.

TU Delft

Preface

This preface serves mainly as an expression of my gratitude to all the people that have assisted me during my MSc thesis.

First of all, to my supervisor Achilleas I would like to say "ευχαριστω!" Your enthusiasm and motivation sparked my interest in the subject of organic bioelectronics. Your personal familiarity with many professors worldwide was also impressive to me.

To Mustafeez, thank you for everything you have taught me in the cleanroom. You were like an older brother to me, who would patiently explain and guide me through the many challenging parts native to working in a cleanroom. Furthermore, I would like to thank you for the many fruitful discussion we have had. I will miss those.

To the rest of the ReBooT group, you guys are amazing. Thank you for the many interesting group meetings we have had and the constructive feedback we could provide each other with.

To my office mates, Limitha, Gandhi, and Maria, thank you for the wonderful persons you are. Your jokes, memes, or advice are some things that I will miss.

To everyone of the Bioelectronics group, thank you for being the best (and most social) group of EEMCS! I enjoyed the many lunches, activities, and table tennis matches that were part of this past year.

To my microtechnology thesis support group, you were a wonderful addition to the many circles I could enjoy for this past year. The interest in each other's projects, though sometimes wildly different than our own, was very special. Shoutout to Lars for smithing this group.

To both the EKL and Kavli cleanroom staff, my deepest gratitude for your hard work and dedication to keeping the cleanroom up and running. Often your work is underappreciated, but you really form the core of the most wonderful activity on this campus. The patience with which you guide newcomers (as I was) and the curiosity into any fabrication process have made a lasting impression on me.

The year was not without its hurdles, including many delays in cleanroom fabrication due to unforeseen circumstances, but I am happy to say that I enjoyed the past year immensely. My next adventure will be in Houston, Texas, and I am glad this thesis felt like a great preparatory exercise before starting my PhD there.

David van der Laan

Contents

1 Introduction

1.1. Background

Neural interfaces hold great potential for advancing neuroscience and clinical applications that combat neuropathological conditions. Interfacing with the nervous system opens up the complex processes underneath and provides a means of interaction, thus enabling clinical intervention if needed. Achieving a reliable neural interface, especially in vivo, is not without cost: biological media are chemically harsh environments and demand strict thermal regulation and high mechanical compliance. To connect the electronics to the human nervous system, the electrical, mechanical, and biological mismatch between the two should be bridged by neural interfaces. The success of neural interfaces was demonstrated almost three decades ago by Kennedy et al. [1] in letting a patient move a cursor up and down with his mind. More recently, Neuralink received attention for enabling a paralyzed patient to play a game of chess online [2]. Further examples of successful neural interfaces are retinal implants restoring vision [3], cochlear implants restoring hearing [4], and spinal cord implants restoring walking [5].

The potential of neural interfaces is amplified by an increasing need for improved neurological treatments. A recent study by Steinmetz et al. [6] showed that 3.4 billion people, or 43.1% of the global population, are impacted by a group of 37 conditions affecting the nervous system. Not only is the impact size concerning, but the burden, expressed in disability-adjusted life years (DALYs), is also increasing. The World Health Organization (WHO) recently initiated an Intersectoral Global Action Plan [7] to tackle the impact and burden of neurological disorders. Countries invested significantly in brain research in the past two decades. Examples include the BRAIN Initiative by the United States [8], the Human Brain Project by the European Union [9], or the China Brain Project [10]. It can safely be concluded that enough interest exists internationally for advancing neural interfaces.

Underlying all neural interfacing is a means of interacting with neurons, the fundamental cells of the human nervous system. Neurons have characteristic electrical behavior that is largely determined by the voltage across the cell membrane, or the voltage difference between the intracellular and extracellular environment. The membrane potential arises due to the concentration differences in and outside the cell of mainly sodium, potassium, and chloride ions. The concentration differences gives rise to a Nernst-potential that is well-defined at 70 mV for the neural cell membrane. The behavior follows an all-or-nothing principle: if the membrane voltage reaches a threshold, the neuron activates and fires an action potential along its axon. At the axon terminal, the electrical signal is converted to a chemical signal that crosses the synaptic cleft.

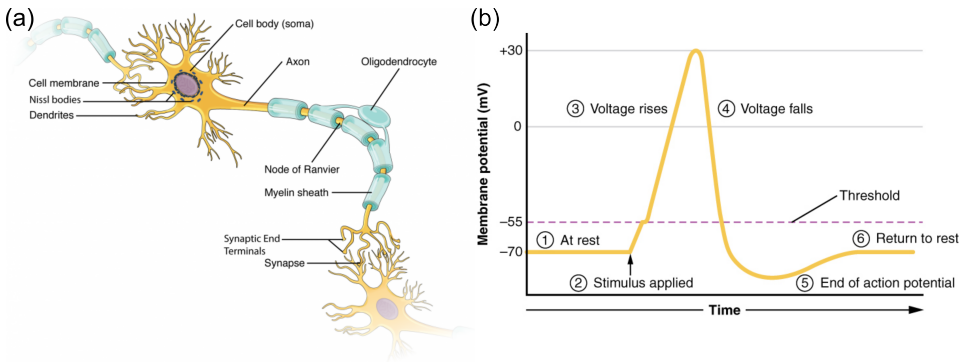

Figure 1.1: Principles of neurons with (a) the anatomy and (b) a chronovoltammetric diagram of an action potential [11].

Interaction with neurons can be separated into two parts: neural recording and neural stimulation. Neural recording is achieved in different ways using electrodes, magnetic sensors, functional magnetic resonance imaging, fluorescence imaging, voltage-sensitive dyes, or intrinsic optical signal imaging. Neural stimulation is achieved using electrodes, ultrasonic transducers, magnetic coils, or lasers. Electrodes stand out for their ability to form a bidirectional interface, meaning that microelectrode arrays can both record (“listen") and stimulate (“talk back") using the same interface. Microelectrode arrays are therefore among the most promising technologies for neural interfacing. A drawback compared to other technologies is that electrodes need to be placed close to the target tissue for accurate recording and stimulation.

Microelectrode arrays are by definition spatially in the micro-scale (10^{-6} m) to mirror the scale of neurons and measure individual units, use electrodes to measure the electrical activity, and consist of an array to create multiple interfacing channels. On an abstract level, the microelectrode array as neural interface can be divided into three main material parts: the electrodes, the passivation layer, and the conducting tracks leading to the back-end electronics. Figure 1.2 shows the abstraction of the MEA.

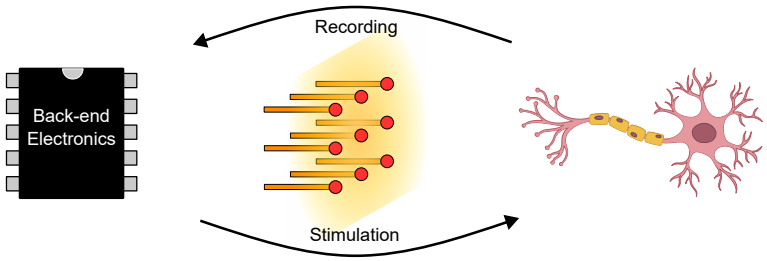

Figure 1.2: Abstraction of a microelectrode array with three components: the electrodes (red), the passivation layer (yellow), and conducting tracks (orange).

For each of these parts, the optimal material and design should be selected. The optimal selection should bridge three main mismatches: electrical, mechanical, and biological. First, there is an electrical mismatch between the neural environment and electronics, as the respective charge carriers differ. Neurons use ionic charge carriers, whereas electronics use electronic charge carriers. Though the unit of both charge carriers is the elementary charge e, their size and mass vastly differ, and consequently, their physical behavior. Furthermore, ions exist only in water in the body while advanced control of electrons demands solid materials. Electrodes translate the ionic signal directly to an electronic signal. The translation can occur in two processes: Faradaic, in which charge crosses the electrode-electrolyte interface, and non-Faradaic, in which no charge crosses the electrode-electrolyte interface. Faradaic processes often imply undesirable chemical reactions and are usually avoided in neural interfaces. The second mismatch is mechanical and arises due to the difference in rigidity between the neural environment and electronics. There are several ways of overcoming the mechanical mismatch, such as minimizing implant dimensions [12] or employing novel, more elastic materials [13]. The third mismatch is biological, as neurons are dynamic and respond to their surroundings in complexity beyond the scope of this discussion. The dynamic nature of neurons contrasts with the static nature of electronics, which can only respond in few preprogrammed ways. Overcoming the biological mismatch is complex and a myriad of dynamic chemical, electrical, and mechanical properties.

Poly-(3,4)ethylene-dioxy-thiophene:poly-styrene-sulfonate (PEDOT:PSS) is a conducting polymer that has established itself as prime candidate for electrode material. It boasts excellent conductivity, biocompatibility, electrochemical stability, and a capacitance that scales per volume instead per area, called the volumetric capacitance [14]. The last property makes PEDOT:PSS a unique electrode material since it can lower the interface impedance with two orders of magnitude compared to Pt [15]. The volumetric capacitance is even more interesting because it allows for mixed ionic-electronic conduction, meaning that ionic and electronic charge carriers flow in the same material. PEDOT:PSS forms therefore an electrical transition layer to accomodate the translation of charge carriers. Additionally, the large capacitance enables high charge storage capacity (CSC) and current-injection capacity (CIC) which are two important metrics for electrode performance [16]. PEDOT:PSS behavior is non-Faradaic, making it an electrochemical safe material. Figure 1.3 summarizes these key points and was made for a review written by our group.

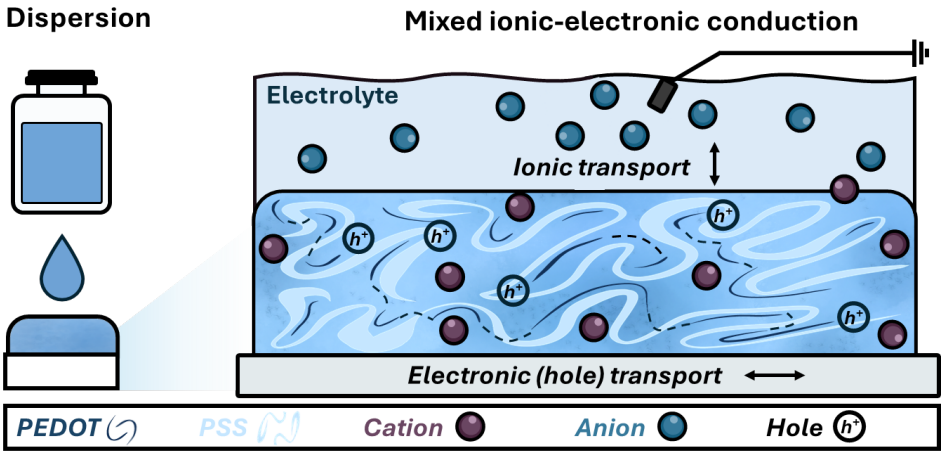

Figure 1.3: Illustration of the main principles of PEDOT:PSS. It is water-based nanoparticle dispersion and can be dispersed or spin coated on substrates. Once applied as layer, it interacts with an electrolyte by swelling and taking in ions (sometimes called 'breathing') which compensates for electronic charge. The ionic activity is reflected by hole activity and can be read out by the backside hole transport layer.

The passivation layer (often also the substrate) is another important component of microelectrode arrays. In the past five decades, silicon-based electronics experienced impressive scaling according to Moore's law and so enabled fabrication of complex devices at the microscale. Consequently, microelectrode arrays were also fabricated using silicon, leading to well-known examples as the Utah [17] or Michigan arrays. However, silicon-based microelectrode arrays suffer from the tissue response post-implantation [18] and long-term instability [19]. Resolving the issue of tissue response prompted exploring new materials to replace the silicon substrate with mainly organic materials. Organic substrate materials, such as parylene C (PaC) and polyimide (PI), were used to overcome the chronic tissue response [20], [21], [22]. Both materials have a lower Young's modulus than silicon, yet the Young's modulus is still several orders of magnitude larger than neural tissue. To enhance device stability and electrode yield while minimizing tissue response, a relatively underexplored avenue is selecting poly-dimethylsiloxane (PDMS) as substrate material for microelectrode arrays. PDMS is a stable elastomer and is used in FDA-approved applications, such as breast implants [23]. Though not a widespread choice as microelectrode array substrate material, PDMS is investigated in many bioelectronic applications where spatial resolution is not a stringent requirement. For example, microfluidic or organ-on-chip devices [24] or stretchable electronics [25] employ PDMS as substrate material. Furthermore, hydrogels have received attention for their ability to mirror the Young's modulus of neural tissue while creating microelectrode array interfaces [26], [27]. The choice of substrate material depends largely on the application in mind as the target tissue should be mimicked but can differ signficantly from another tissue [28].

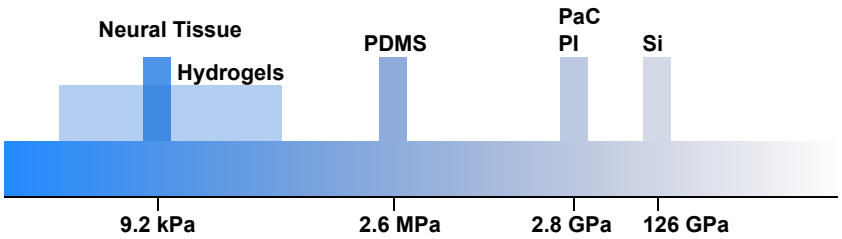

Figure 1.4: An illustration of the difference in the Young's modulus of substrate materials used for microelectrode arrays compared to the target neural tissue. Abbreviations: Si is silicon, PaC is parylene C, PI is polyimide, and PDMS is polydimethylsiloxane. For more information and references, see Table 2.1.

1.2. Aim of the MSc Project

The aim of this MSc thesis is to explore the materials PEDOT:PSS and PDMS for microelectrode array technology applicable to neural recording and stimulation in the central nervous system. Using the electrode material PEDOT:PSS and the substrate material PDMS combines the advantages of the two: the high capacitance of PEDOT:PSS and the high flexibility of PDMS. Additionally, creating a polymer-polymer (PEDOT:PSS-PDMS) interface could reduce delamination effects often observed in metal-polymer interfaces [29]. Previous attempts of fabricating all-polymeric microelectrode arrays using PEDOT:PSS and PDMS were made [30], [31], [32]. Though the all-polymeric microelectrode arrays show promising results in terms of cell viability and device flexibility, the approaches did not reach electrode dimensions smaller than 120 μm. The lack of spatial resolution and fundamental understanding of PEDOT:PSS and PDMS interactions limit the applicability of all-polymeric devices compared to the state-of-the-art, even though all-polymeric devices have great potential for enabling long-term stability. A thorough investigation into PEDOT:PSS and PDMS would therefore add an extra tool to the microelectrode array toolkit.

The objective of this MSc thesis project is to contribute to the understanding of PEDOT:PSS and PDMS and their application for microelectrode array technology. To achieve it, the following goals were set up for this project:

- Conduct a literature study on the microfabrication of PEDOT:PSS and PDMS for microelectrode arrays technology.
- Characterize PEDOT:PSS and PDMS layers and interface between the layers.
- Explore the lithographical patterning of PEDOT:PSS on PDMS and verify the compatibility with semiconductor microfabrication processes.
- Create an all-polymeric microelectrode array that can be tested for long-term stability and compared against metal-polymer microelectrode arrays.

1.3. Structure of the Report

The report starts with introducing the topic of microelectrode arrays, their clinical and societal relevance, and the challenges involved in engineering microelectrode array technology in this chapter, chapter 1. The literature study conducted for the MSc thesis is detailed in chapter 2. It discusses the materials PEDOT:PSS and PDMS, design considerations for microfabrication of microelectrode arrays, and state-of-the-art devices. It concludes with a specific research question that forms the basis for the rest of the research. Chapter 3 investigates spin coated layers of PEDOT:PSS and PDMS, their interface, and the effects on the material properties of PEDOT:PSS. Two crosslinkers are dissolved in PEDOT:PSS (GOPS and PEGDE) and the thin films are electrically, mechanically, and electrochemically characterized. Chapter 4 discusses the design choices for the final microelectrode array device. The device fabrication is detailed in the next chapter, chapter 5. Finally, major findings are discussed and the report is concluded in chapter 6.

2
Literature

The literature review focuses on the fabrication of PEDOT:PSS microelectrode arrays on PDMS substrates. First, design considerations for microelectrode arrays are explored. The main trends in designing microelectrode arrays are device miniaturization, signal recording quality optimization, and maximizing device bending stiffness and device lifetime. For implants, low power consumption and low thermal heating are also important criteria. However, since the microelectrode arrays are designed for microfluidic systems, the last two criteria are not discussed. Then the materials PEDOT:PSS and PDMS are discussed in detail and their applicability to microelectrode array fabrication. Relevant fabrication techniques are also discussed to provide context to the microfabrication process. Next, state-of-the-art devices are discussed and compared using a comparison table. Lastly, a summary with the main findings of the literature review are given and the specific research question that this project aims to answer.

2.1. Microelectrode array design considerations

Microelectrode arrays are neural interfaces and should therefore fulfill two important functions: record neural activity and stimulate neurons to achieve a desired neural response. These two functions are different but use the same electrodes. To discuss the design considerations for microelectrode arrays while keeping in mind the two different functions, equivalent circuit models for the two functions are helpful. The equivalent circuit for a neural recording setup is shown in Figure 2.1 and for a neural stimulation setup is shown in Figure 2.2. The circuit models are heavily simplified to emphasize the electrode interface. The electrode interface model is based on Randles circuit [33]. The resistor for Faradaic charge transfer is removed from the circuit model as Faradaic charge transfer is mostly undesirable in neural interfacing applications (with an exception of the stable charge transfer of iridium oxide).

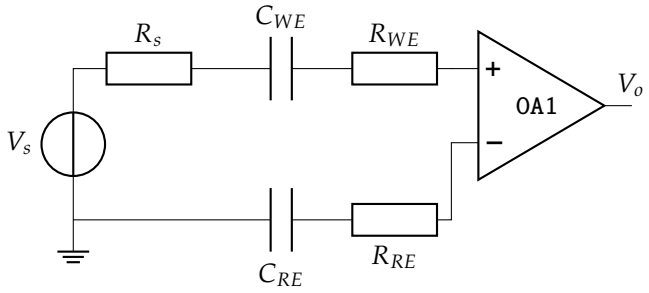

Figure 2.1: A simple circuit model for a neural recording setup. V_s is the source voltage, R_s is the source resistance, C_{WE} is the working electrode capacitance, R_{WE} is the working electrode resistance, C_{RE} is the reference electrode capacitance, R_{RE} is the reference electrode resistance, and V_o is the output voltage. The readout circuit is modeled as a differential amplifier without feedback loop to keep the model as simple as possible.

Recording neural activity is done by essentially measuring the ionic concentrations in the extracellular space which reflects action potentials of nearby neurons. Ions carry an intrinsic charge and electrodes can couple the ionic charge to electronic charges via either Faradaic or non-Faradaic processes. Recording setups measure the potential between the working electrode (WE) and the reference electrode (RE). Usually, the reference electrode is made much larger and placed far away to form a ground so the working electrode accurately measures the potential at its location. In that case, the elements C_{RE} and R_{RE} can be ignored in Figure 2.1.

Stimulation aims to activate nearby neurons by influencing their membrane potentials. The membrane

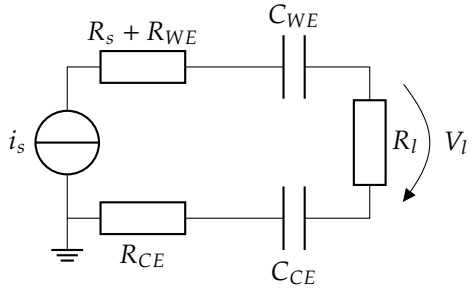

Figure 2.2: An equivalent circuit model for a neural stimulation setup. i_s is the source current, R_s is the source resistance, R_{WE} is the working electrode resistance, C_{WE} is the working electrode capacitance, R_l is the load resistance of the target tissue, C_{CE} is the counter electrode capacitance, R_{CE} is the counter electrode resistance. A current source is chosen since it current stimulation can control the load voltage independent of the electrode impedances.

potential arises due to the Nernst-potential of sodium, potassium, and chloride. By influencing the extracellular potential through electrodes, a membrane potential can become sufficiently depolarized to elicit an action potential. Attention should be paid that stimulation currents/voltages are within safe limits. High potentials across the electrode interface can cause harmful chemical reactions.

With the circuit models in place, the metrics used to compare microelectrode arrays and the reasons for these metrics are explored. The metrics also provide quantifiable goals for the design of microelectrode arrays. A metric is formulated as minimization or maximization of one aspect. Since the metrics are in tension with one another, trade-offs arise and should be investigated for optimal design. The five metrics are:

- The device dimensions shall be as small as possible.
- The signal recording quality shall be as high as possible.
- The stimulation capacity shall be maximal.
- The bending stiffness of the device shall be minimal.
- The lifetime and stability of the device shall be maximal.

2.1.1. Dimensions

The first and most straightforward consideration is the device dimensions. Smaller dimensions give an increased spatial resolution and higher electrode density. Electrode surface diameters must be in the range of 10-20 μm for high spatial resolution [16] and smaller in diameter than 100 μm to accurately record single units [34]. Furthermore, electrodes have to be in close proximity (100-200 μm) to the target to be able to electrically isolate action potentials [12]. The minimization of device size comes at the cost of higher interface impedances, since the impedance scales inversely with the area. The impedance of the working electrode in Figure 2.1 is mathematically expressed as

$$|Z| = \sqrt{(R_{WE})^2 + (\frac{1}{\omega C_{WE}})^2} = \sqrt{(\frac{V_{WE}}{J_{WE}A})^2 + (\frac{d}{\omega \epsilon A})^2} = \frac{1}{A}\sqrt{\frac{V_{WE}^2}{J_{WE}^2} + \frac{d^2}{\omega^2 \epsilon^2}} \tag{2.1}$$

where $|Z|$ is the electrode impedance magnitude, $\omega = 2\pi f$ is the radian frequency, V_{CE} is the potential across the electrode, J_{CE} is the current density through the electrode, A the area of the electrode, d is the electrode thickness, and ϵ is the electrical permittivity of the electrode.

Besides single unit isolation there is a necessity to monitor large numbers of single neurons for unraveling coordinated neural activity, which requires large arrays of multiplexed recording electrodes with minimal dimensions [35]. For in vivo applications, the device size is also important for acute tissue damage following implantation. Smaller sizes leads to less disturbance of the tissue, less injury due to insertion, and so safer devices [36], [37]. Besides the size, the geometry of the probes also influences the acute tissue damage and the chronic immune response [38], [39]. The difficulty lies in controlling device characteristics at smaller dimensions and fundamental limits may prevent further size reduction, analogous to the breakdown voltage or leakage phenomena in nanoscale semiconductor devices.

Polymers are a lesser established technology in microfabrication and are incompatible with some processes or machines in the cleanroom. As such, creating smaller devices than the state-of-the-art CMOS devices is unlikely. However, the all-polymeric devices shall still aim to be minimal in size, which provides valuable insight in the advantages and disadvantages of using polymers for microelectrode array technology.

2.1.2. Signal recording quality

The primary concern for neural recording is to retrieve the signal of interest as accurately as possible. The standard metric for recording quality is the signal-to-noise ratio (SNR). It is defined as

$$SNR = 10log(\frac{P_s}{P_n}) = 20log(\frac{\bar{V}_s}{\bar{V}_n}) \tag{2.2}$$

where P_s is the signal power, P_n is the noise power, $\bar{V}_s$ is the voltage root-mean-square (RMS) value of the signal, and $\bar{V}_n$ is the noise RMS voltage. The unit is in decibel, or dB.

The signals of interest in neural recording are the spiking activity of individual neurons and the local field potentials generated by large groups of neurons. The frequency of spiking activity is around 1 kHz. The frequency of local field potentials is in the range of 1-10 Hz. Both signals are voltage signals, meaning that the voltage in neural tissue should be measured to retrieve the signals. Voltage levels are measured with respect to a reference or ground level and so always taken at two points.

Practically, an infinite input impedance is not feasible. Due to the high impedance of the electrode interface ($10^5\Omega$), the input impedance of the readout circuit should be sufficiently large so that negligible signal attenuation occurs over the electrode impedances. The Metrohm Autolab PGSTAT302N or PalmSens4 were used as readout circuit and both have an input impedance of ($10^{12}\Omega$), which is deemed sufficiently large compared to the electrode impedance. Conclusively, the electrode impedance is hypothesized to not contribute to signal attenuation.

The other factor in the signal-to-noise ratio is the noise. Noise can be defined as the disturbances that occlude the signal of interest. Importantly, it is distinct from interference which originates from man-made and predictable sources. The following types of relevant noise sources can be identified:

- Thermal noise, or Johnson-Nyquist noise, arises due to the thermal motion of charge carriers.
- Shot noise comes from charge carriers crossing a boundary, for example the charge depletion region in a diode.
- Pink noise, or 1/f noise, has no well-defined source but is visible in almost all electronic circuits. It has a characteristic 1/f curve, so at lower frequencies the noise power is higher.
- Biological noise in neural tissue is caused by the background activity of neurons, such as a distant neuron firing.

Literature provides detailed reviews of noise in electrodes by [40] and noise in the neural environment by [41]. Biological noise is the dominant noise source but not easily characterized. The second dominant noise source and important for design is the thermal noise. Therefore, only thermal noise will be explored in depth.

Thermal noise is caused by the irregular thermal motion of charge carriers and is mathematically described as

$$\bar{V_n^2} = \sqrt{4k_BTR\Delta f} \tag{2.3}$$

where $\bar{V_n^2}$ is the root-mean-square noise voltage, k_B the Boltzmann constant, T the temperature, R the resistance, and Δf the bandwidth of interest. Since the bandwidth of interest is not near the corner frequency of the high-pass filter transfer function of Figure 2.1, the thermal noise is taken as white noise. For justification, please refer to Appendix A.

The minimization of thermal noise for microelectrode arrays cannot be achieved by reducing the temperature as the temperature in biological media is set to a small range. Reducing the bandwidth of interest is optional, yet adds complexity and entails discarding information. It leaves reducing the resistance. Since the source resistance cannot be altered, the electrode resistance should be minimized. The electrode resistance includes influences on the biological side such as the foreign body response.

In literature, the reduction of electrode impedance has been topic of discussion. Neto et al. [42] argued that the thermal noise was not the dominant noise source in vivo, but rather the biological noise. They continued that lowering impedance, and thus thermal noise, is therefore unnecessary, especially since successful spike sorting could be achieved regardless of lowered interface impedance. Mierzejewski et al. [40] disagreed on the basis of theoretical spike sorting limits. Thermal noise is a limiting factor and reducing thermal noise should contribute to improved spike sorting. They also mention that biological noise can be reduced pharmalogically and is therefore not fundamental. Additionally, in vitro applications may benefit from thermal noise reduction since they do not suffer from biological noise as much as in vivo. Lewis et al. [15] added to it by demonstrating that electrode impedance is systematically related to recording quality and that optimizing electrode design includes minimizing electrode impedance. Interestingly enough, Lewis et al. do not distinguish between the real and imaginary component of the impedance, though only the real component adds to power and signal loss. Also, their signal-to-noise calculations take interference from a 50 Hz powerline as dominant noise source, which is not a good practice since interference can and should be avoided whereas noise is a fundamental limiting factor.

2.1.3. Stimulation capacity

The stimulation capacity is largely material-dependent and determines what charge densities can be injected before undesired or harmful side-effects occur. Stimulation can be done in unipolar, bipolar, or multipolar configurations [37]. Two metrics are used to characterize the stimulation performance of electrodes: the maximum charge injection capacity (CIC_{max} [μcm^{-2}]) and the maximum charge storage capacity (CSC [μCcm^{-2}]). For high-density electrodes, unipolar stimulation is usually performed. A biphasic charge-balanced current signal is injected in the electrodes and results in a voltage excursion as in Figure 2.3.

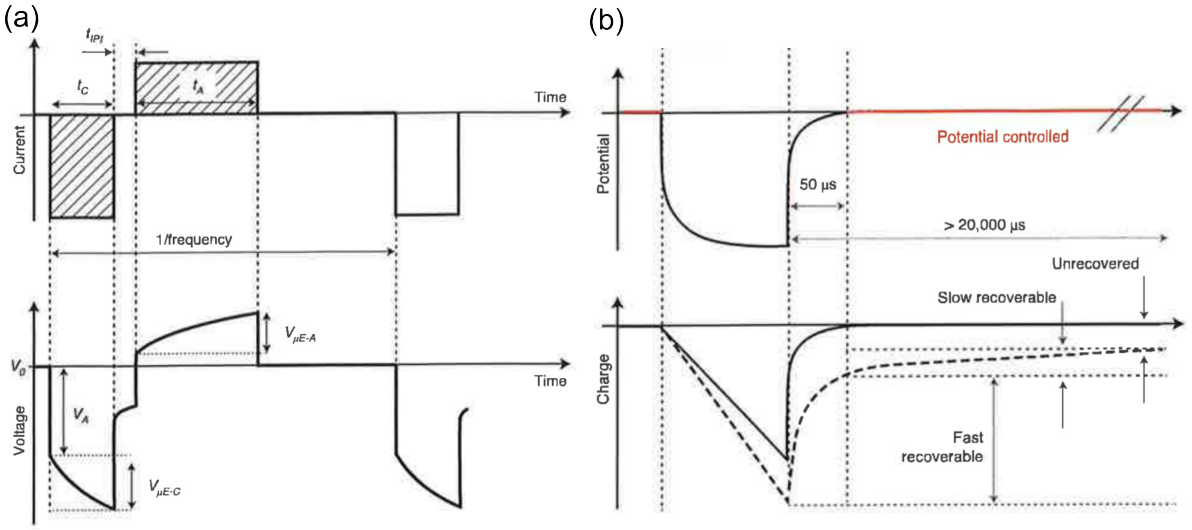

Figure 2.3: A (a) biphasic current pulse and the corresponding voltage response and (b) limitations of biphasic current stimulation is that not all charge is recovered after a pulse from [16].

Boehler et al. [16] gave two definitions of the maximum charge injection capacity (CIC_{max} [μcm^{-2}]): the current at which $V_{\mu E}$ (from Figure 2.3a) reaches the water window or measuring with the pulse-clamp method in Figure 2.3b for what current level the injected charge is not fully recovered.

The charge storage capacity can be determined from a cyclic voltamettry diagram by integrating the current from the cathodic sweep. However, this practice may not be as good an indicator of electrode performance as the CIC_{max} [16].

2.1.4. Flexibility

Another aspect of microelectrode array design is device flexibility and elasticity, quantified as bending stiffness and Young's modulus. Bending stiffness is the product of the Young's modulus and the second moment of inertia, so device flexibility and elasticity are related. Distinctive is that the Young's modulus is purely a material property, whereas the bending stiffness is also influenced by the geometry.

State-of-the-art devices aim to be as flexible and conformable as possible. The reason for minimal bending stiffness is found in the chronic immune response to implants. The foreign body response (FBR) is the device encapsulation by immune cells and is one of the stages of the chronic immune response. Biran et al. [18] demonstrated that a chronic immune response causes a reduction of nerve cells surrounding a silicon implant. Additionally, they observed that immunoreactive cells covered the device surface. Both contribute to a reduction of signal recording quality or even signal loss. Barrese et al. [19] investigated the stability of silicon microelectrode arrays over a time span of sixteen years. They identified several failure modes, including chronic failure due to encapsulation caused by the immune response. Out of 62 devices, 9 failed due to a chronic immune response. Devices aiming for long-term clinical use should overcome the issue of the chronic immune response.

While the signal is captured by the electrode, the immune system responds to the complete device. As such, techniques for optimizing signal recording through enhanced and biocompatible electrode materials do not negate the immune response to the device. Ludwig et al. [43] studied microelectrode arrays with silicon substrate and PEDOT:PSS coated iridium electrodes for a period of six weeks in vivo. They demonstrated an improved signal-to-noise ratio for PEDOT:PSS coated electrodes compared to uncoated electrodes. However, Ludwig et al. also observed a significant increase in impedance during the first week after implantation. They attributed the increase in impedance to an immune response. After three weeks, the impedance stabilized but remained significantly higher than directly after implantation.

It should be noted that the immune response in the central nervous system (CNS) and the peripheral nervous system (PNS) are different. Immune cells in the circulatory system cannot enter the central nervous system through the blood-brain-barrier (BBB). Hence, the central nervous system has a distinctive immune response. The exact functioning is beyond the scope of this project, but it has been reviewed well by [36] and [44]. The peripheral nervous system also exhibits a characteristic immune response and is reviewed by [44] and [45]. Since the goal of this project is to fabricate microelectrode arrays for neural recording of (developing) neurons in the central nervous system, the immune response in the peripheral nervous system will be disregarded.

Returning to device flexibility and elasticity, Kozai et al. [46] summarized the influence of mechanical strain on the immune response. They conclude that shear strain leads to neurite loss and cell death around the implant, followed by a chronic immune response. Minimizing the shear strain entails overcoming the mechanical mismatch between implant and the surrounding tissue, resulting in the well-known push towards more elastic devices using materials with a lower Young's modulus. Nguyen et al. [47] showed that increased device compliancy leads to a reduced chronic immune response. They implanted two geometrically identical probes with the different materials, one rigid and one compliant, and observed the immune response. Seymour and Kipke [48] researched the influence of the device geometry on the chronic immune response and found that device geometry influences the immune response. Conclusively, not only material considerations, the Young's modulus, should be considered, but also the geometry in which it is applied. It leads to minimizing the bending stiffness of implants and it can be achieved in two ways: (1) selecting a substrate material with a lower Young's modulus and (2) optimizing the device geometry to conform to the target tissue, which includes making the device smaller.

For the literature study, state-of-the-art examples seldom report the bending stiffness of the device. The analysis of bending stiffness is often ignored and an analysis of the tissue damage after in vivo testing is done, mostly using cell staining techniques. Tissue damage does not provide an easily quantifiable unit however, whereas bending stiffness does. Therefore it is opted to analytically estimate the bending stiffness of state-of-the-art devices using

$$D = \frac{Eh^3}{12(1-v^2)} \tag{2.4}$$

where D is the bending stiffness (or flexural stiffness), E the Young's modulus of the substrate material, h the substrate material height, and v the Poisson's ratio of the substrate material [44]. The bending stiffnesses of state-of-the-art devices are calculated and shown in Table 2.2.

2.1.5. Device lifetime

Device lifetime is defined as the time for which the microelectrode array device is functional as intended. Ideally, the device lifetime should be infinite. Realistically, this is not achievable. Since the intended use of the microelectrode array is to interact with the neural tissue, optimal lifetime assessment is done in vivo (for example [15], [49]). However, this does not provide a standardized procedure with which different devices can be readily compared. Guidelines on device lifetime assessment was given by [16], suggesting the following accelerated aging setup: immersion of the device in phosphate-buffered saline (PBS) at $60°C$. After an aging experiment, the device should be characterized with electrochemical impedance spectroscopy (EIS), cyclic voltammetry (CV), and high resolution imaging.

2.2. PEDOT:PSS

Poly-(3,4)-ethylene-dioxythiophene:poly-styrene-sulfonate (PEDOT:PSS) is a colloidal nanodispersion, meaning that the nanoparticles consists of two polymers dissolved in water: polymer chains of (3,4)-ethylene-dioxythiophene (EDOT) and chains of styrene-sulfonate (SS). The monomer units within the polymer chains are shown in Figure 2.4a and 2.4b.

Figure 2.4: Chemical structure of (a) (3,4)-ethylene-dioxythiophene (EDOT) and (b) styrene-sulfonate (SS).

The development of PEDOT:PSS was achieved in steps. A more extensive review on PEDOT:PSS is written by our group and under review for publication [50]. The polymer (3,4)-ethylene-dioxythiophene (PEDOT) was synthesized for the first time in 1992 and reported by Heywang et al. [51]. They noted the extraordinary conductivity and electrochemical stability of PEDOT. However, creating stable PEDOT required $FeCl_3$, a toxic counterion. Yamato et al. [52] were the first to stabilize PEDOT using poly-styrene-sulfonate and so created PEDOT:PSS, emphasizing its potential for biosensor applications. It led to electrochemical deposition of PEDOT:PSS on silicon neural probes by Cui and Martin [53], who tested the probes in guinea pigs. They found that higher signal amplitudes could be recorded using coated electrodes. The discovery of superior performance by PEDOT:PSS coated electrodes ignited incredible innovation in microelectrode array technology. In Figure 2.5, a timeline of the chemical synthesis and application of PEDOT:PSS is shown.

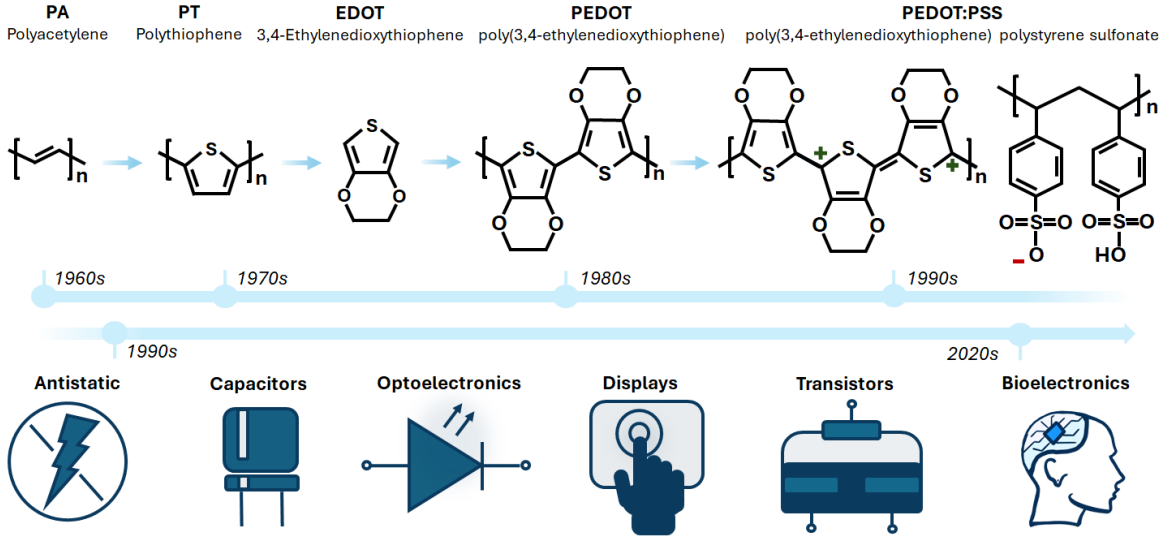

Figure 2.5: The chemical synthesis of PEDOT:PSS over the years and its evolution as material in various applications. Recently, PEDOT:PSS emerged as promising material, heralding the era of organic bioelectronics [54]. The figure is taken from the review paper written by our group [50].

PEDOT:PSS belongs to the class of conducting polymers and has mixed ionic-electronic conductivity, meaning that it conducts both ionic and electronic charge carriers. Materials with such behavior are called organic mixed ionic-electronic conductors (OMIECs). Paulsen et al. [55] provide an overview of various types of OMIECs and what characterizes them.

Conductivity describes the rate of charge transport in any material as a result of applied electric fields and is mathematically notated as

$$\sigma = \frac{J}{E} = \mu n q \tag{2.5}$$

Where σ is the conductivity with unit S m^{-1}, J the current density with the unit A m^{-2}, E the electric field with unit V m^{-1}, μ the mobility of the charge carrier, n the number of charge carriers, and q the charge of the carrier (often the elementary charge $e = 1.6 \cdot 10^{-19}$C). J and E are taken along the axis of interest.

In silicon semiconductors, doping is used to add free charge carriers to the silicon lattice. III/V materials, such as boron or phosphorus, are implanted in the silicon lattice. Due to different covalent bonding, electrons or holes in the outer shell are left and function as majority charge carriers. Doping thus increases the conductivity by increasing n in Equation 2.5. For PEDOT:PSS, the charge carrier density remains constant [56], but the mobility of charge carriers can be varied. The term μ in Equation 2.5 is thus of importance when discussing the conductivity of PEDOT:PSS.

In Figure 2.6 (a), the chemical formula for PEDOT and PSS are shown. The majority electronic charge carriers in PEDOT are holes, which arise from delocalized bonds along the polymer backbone. The oxidation level, i.e. generation of holes per monomer, is around 33% but can be altered with electrochemical techniques [56]. The holes can hop from one localized site to another along the polymer backbone. PEDOT chains are usually 10-20 monomer units long, meaning that holes cannot indefinitely propagate through the material along a single backbone. However, the PEDOT chains are stacked on top of each other through $\pi - \pi$ bonds and are so interconnected. These stacks of PEDOT chains aggregate into grains, small morphological islands that are rich in PEDOT. Since PEDOT itself is not charge-neutral and unstable, it needs the support of a negatively charged counter-ion. For PEDOT:PSS, PSS is the counterion. The chemical structure of PSS is shown in Figure 2.6 (a). PSS is an insulating material and forms a matrix around the PEDOT grains, effectively insulating these grains from one another. Surprisingly, the holes can still move through the material and hop from one grain to another through efficient tunneling [57]. The efficiency of the tunneling is inversely proportional to the distance between the grains.

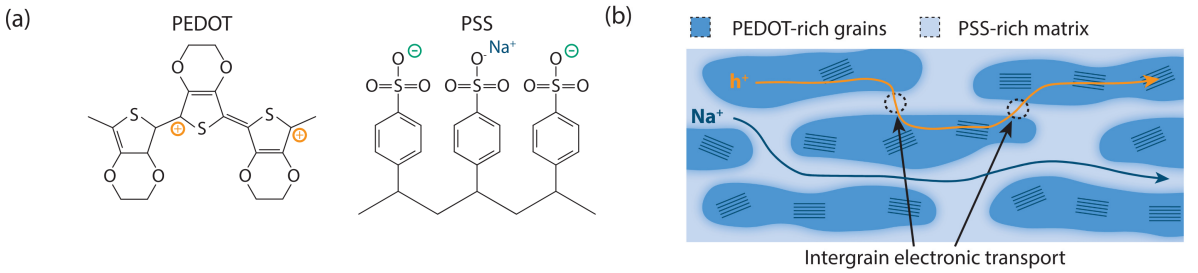

Figure 2.6: Illustration of the origin of charges in the chemical structure of PEDOT and PSS (a) and the charge transport between PEDOT-rich grains and PSS-rich matrix in PEDOT:PSS (b). Adapted from [57].

The electronic conductivity of PEDOT:PSS can be altered by manipulating the PEDOT-rich grains and PSS-rich matrix. The first work to discuss the origin of the improved conductivity of PEDOT:PSS was done by Crispin et al. [58]. They investigated how the addition of ethylene glycol (EG) as a solvent enhanced the electronic conductivity. Atomic force microscopy (AFM) revealed more phase segregation of PEDOT-rich grains and PSS-rich matrix, making for longer conduction paths and less effective insulation of PEDOT grains by PSS. Shi et al. [59] reviewed the various treatments and techniques that increase or decrease the electronic conductivity of PEDOT:PSS. Notable is the work done by Kim et al. [60] that investigated H_2SO_4 treatment of PEDOT:PSS. They discovered that post-treatment with H_2SO_4 induced crystallization and nanofibril formation and could improve the electronic conductivity to $\sigma_h = 4380$ S/cm, only one order of magnitude smaller than most metals and comparable to that of indium-tin-oxide (ITO). The claim that the H_2SO_4-induced crystallization causes the largest mobility is in tension with [61], claiming that not crystallinity but more efficient transport is key to improving the mobility. More efficient transport makes the material more tolerant to the inevitable lattice disorder of the polymer. Hosseini et al. [62] found that H_2SO_4 post-treatment of PEDOT:PSS films mixed with dimethylsulfoxide (DMSO) and ethylene glycol (EG) actually reduces the electronic conductivity. They confirmed through spectroscopy and AFM that the intergrain connectivity and not intragrain crystallinity is responsible for increasing the electronic conductivity. The increased conductivity in [60] is therefore more likely to be caused by the removal of PSS instead of PEDOT crystallization, which the authors also recognized as a contribution to the improved conductivity. Combining techniques to both

selectively improve and decrease conductivity allows for patterning, such as in [27], where a resolution of 6 μm was achieved through laser-induced phase separation.

While electronic transport occurs mostly in the PEDOT-rich grains, ionic transport occurs mostly in the PSS-rich matrix. Stavrinidou et al. [63] measured the mobility of ions in PEDOT:PSS and found that the ionic mobility is enhanced by electro-osmotic behavior in the PSS-rich regions. Ions travel into the material and couple to a localized charge site while ejecting a hole. Keene et al. [64] investigated the relationship between the ionic and electronic charge transport and found that holes and ions have a leader-follower relationship caused by the difference in mobility. The holes can rapidly rearrange under changing electric fields, while the ions respond slowly to the electric field.

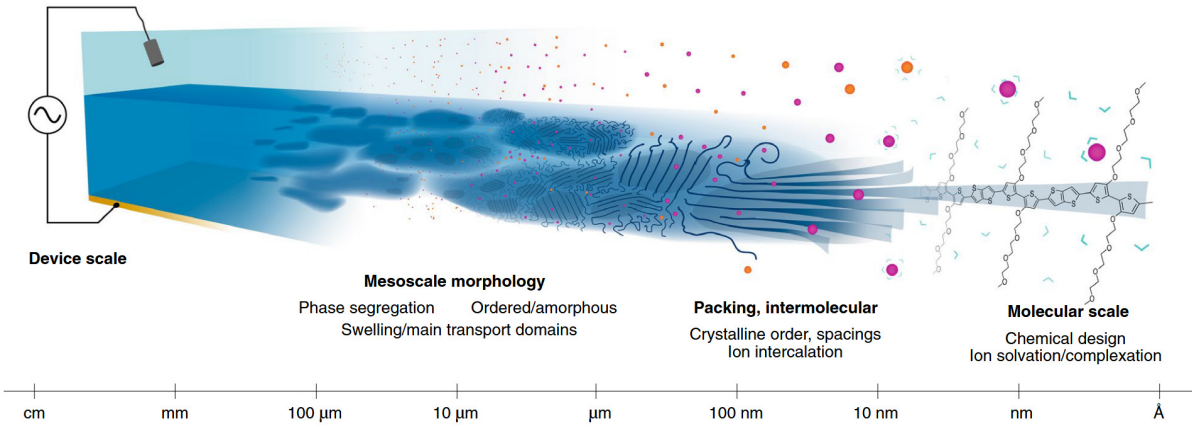

Figure 2.7: Illustration from [55] showing the different aspects of mixed ionic-electronic conductors at various spatial orders of magnitude, highlighting the molecular, intermolecular, morphological, and device scale. PEDOT:PSS shows remarkable processing-induced material property changes, especially at the morphological scale. The dark blue lines indicate PEDOT chains, the light blue regions indicate the PSS-rich matrix, and the pink and orange spheres indicate positive and negative ions.

Morphology plays an important role in the mobility of both the holes and the cations. On one side, electronic transport occurs in PEDOT-rich grains and increases with smaller intergrain distance. On the other side, ionic transport happens in the PSS-rich matrix and benefits from larger channels for the ions to move through. Rivnay et al. [65] were the first to explore the trade-off between the ionic and electronic mobility for organic electrochemical transistors (OECTs). Upon contact with an electrolyte, the morphology changes due to swelling caused by water uptake. Savva et al. [66] investigated the influence of water uptake on OECT performance and found that an optimal water uptake exists, which balances electronic and ionic mobility. Thicker films were found by [67] to have lower coupling efficiency between ions and holes, and not all ions participate in ion-to-electron conversion. While thickness itself is not strictly a morphological phenomenon, STEM measurements showed that thick films contain less crosslinking. The reduced crosslinking makes the material less tolerant to swelling-induced disorder, losing electronic conductivity and reducing ionic-electronic coupling efficiency. Another aspect is the long-term stability of ionic and electronic mobility in PEDOT:PSS thin films. Kim et al. [68] found that sulfuric acid-induced crystallinity is important in long-term stability for PEDOT:PSS OECTs. The crystallized PEDOT:PSS films had minimal water uptake and so minimal induced stress, enabling long-term stability.

The conductivity enhancement through solvents is a widely explored research topic, as discussed earlier in this chapter. Most notable are the solvents ethylene glycol (EG) and dimethyl sulfoxide (DMSO). Additionally, the solvent dodecylbenzene sulfonic acid (DBSA) is used for improving the thin film formation. Crosslinkers can be used to functionalize surfaces, though in most microfabrication literature crosslinkers are mixed with PEDOT:PSS. (3-glycidyloxypropyl) trimethoxysilane (GOPS) is used for crosslinking PEDOT:PSS and enables stability when immersed in water. The chemical structure of GOPS is shown in Figure 2.8a. Poly(ethylene glycol)diglycidyl ether (PEGDE) is also used as crosslinker by [69] and stabilizes PEDOT:PSS in water. The chemical formula of PEGDE is shown in Figure 2.8b. An important difference between GOPS and PEGDE is that GOPS has a silane group, whereas PEGDE does not. The silane group indicates stronger adhesion to silicon-based materials, such as PDMS. By choosing between different crosslinkers, the adhesion to other materials can be influenced. For example,

PEDOT:PSS with PEGDE might be used as a lift-off layer since it has hypothetically worse adhesion to silicon.

Figure 2.8: Chemical structures of two crosslinkers, (a) GOPS and (b) PEGDE.

A key benefit of PEDOT:PSS is its *volumetric* capacitance. Since the chains of conducting polymers are loosely connected, electrolyte can penetrate into the bulk of the material. This is fundamentally different from electrolyte interactions with rigid materials, where interactions are limited to the contact surface. The significance of this difference was first expressed by [70] and led to the term volumetric capacitance in [14]. As implied in the name, the volumetric capacitance scales with material volume instead of contact surface. PEDOT:PSS doped with EG, DBSA, and GOPS, demonstrates a consistent volumetric capacitance of 39 F/cm^3. Treating PEDOT:PSS with sulfuric acid also increases the volumetric capacitance to 113 F/cm^3 [68]. Consequently, the capacitances for small areas can be significantly larger than metals, resulting in improved electrode stimulation performance [71] and lower interface impedance that can lead to higher SNR [15].

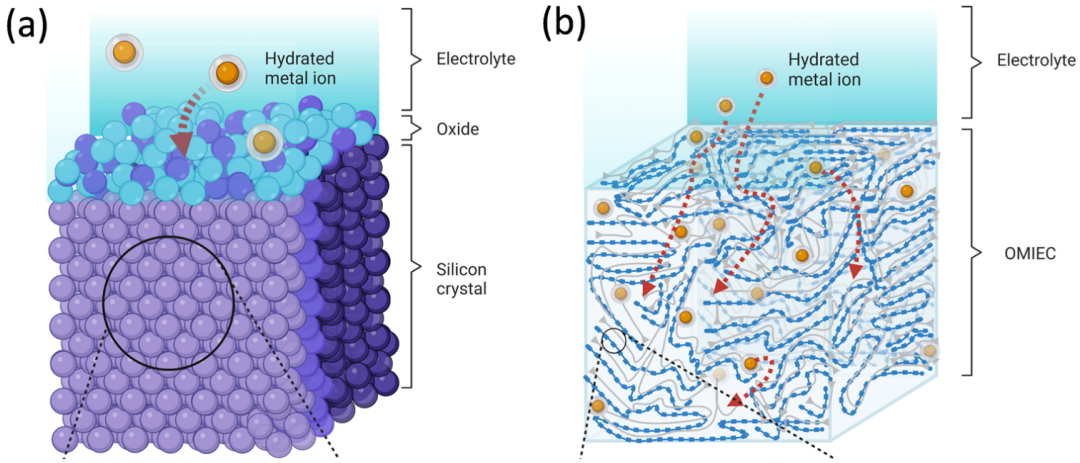

Figure 2.9: An illustration from [39] shows the difference between conventional rigid electrode materials, in this case (a) silicon, and (b) novel conducting polymeric electrodes. Ions can travel into the bulk of organic mixed ionic-electronic conductors, compared to interactions limited to the surface.

Miniaturization of PEDOT:PSS microelectrode arrays is challenging. Small area PEDOT:PSS electrodes (diameter <100 μm) are achieved in two ways in the state-of-the-art: using a parylene C lift-off technique from [72], [73], [74] or electrodeposition on conductors [75], [76]. The first method fixes the choice of substrate to at least include parylene C, whilst the second requires a conductor before PEDOT:PSS can be applied. Metals delaminate over time from polyimide [77], parylene C [29], or PDMS [78] and are therefore less desirable to create long-term stable devices. The non-covalent bonding and weaker adhesion of PEDOT:PSS to other materials limited the applicability, though the adhesion can be significantly improved using several techniques. Poly-utherane (PU) can be used as an adhesive layer [79] and preserves the electrical and mechanical properties of PEDOT:PSS. PEDOT:PSS has a poor long-term adhesion to several metals (Pt, PtIr, Au), but the addition of iridium oxide (IrOx) as layer between Pt and PEDOT:PSS creates a stable interface [75]. Additionally, increasing the contact area between Pt and PEDOT:PSS through laster structuring improves the long-term stability [80]. The adhesion of PEDOT:PSS onto parylene C outperformed Au electrodes and tracks under accelerated aging conditions for electrical stimulation [29]. An important factor may be that PEDOT:PSS swells upon contact with water [67] and can be controlled through solvent addition, whereas metals do not. The swelling of PEDOT:PSS can be tailored to mirror swelling of for example, PDMS.

2.3. PDMS

Poly(dimethyl-siloxane), or PDMS, is a viscoelastic polymer boasting a low Young's modulus (2.5-4.5 MPa [81]). PDMS is a well-established material, easy to process, and is found in FDA-approved applications [23]. The chemical structure of a polymer chain is shown in Figure 2.10.

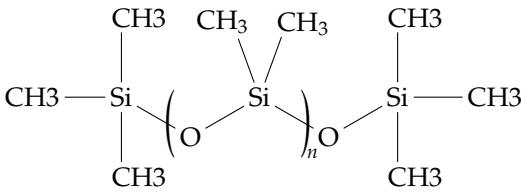

Figure 2.10: Chemical structure of PDMS.

Two methyl groups are visible in its chemical structure and are connected to a siloxane chain. Due to the absence of hydroxy groups, PDMS is a hydrophobic material. The hydrophobicity can problematic during processing. For example, spin coating PEDOT:PSS on PDMS produces poor results since PEDOT:PSS is hydrophilic and PDMS is hydrophobic. However, the hydrophobicity of PDMS can be reversibly transformed with a surface oxygen plasma treatment and maintained up to several weeks if stored in deionized water [82]. The increased wettability is attributed to a chemical transformation and subsequent exposure of $SiOH$ and CH_2OH groups [83]. Lipomi et al. [84] investigated surface treatments of PDMS to enhance spin coating of PEDOT:PSS and found that oxygen plasma treatment produced irreversibly cracking. The power of the oxygen plasma was relatively high however (150 W) and the effects of lower power were not explored. Lower power may produce less severe surface modification than reported.

Other substrate materials used for microelectrode arrays are parylene C [20], [73], [85] and polyimide [76], [86]. PDMS is a silicone and has substantial water ingress [87]. The water ingress does not leave PDMS irrelevant as coating material for implants as it prevents degradation of integrated circuits [88]. Parylene C and polyimide have substantially less water vapor permeability, as shown in Table 2.1. Other relevant material properties, such as the Young's modulus, Poisson's ratio, and dielectric constant are shown in Table 2.1 as well. Ideally, a substrate should have a Young's modulus and Poisson's ratio equivalent to the one of neural tissue and a low dielectric constant to minimize crosstalk. The substrate should also be biocompatible, meaning minimal negative side-effects at the site of implantation [89]. The biocompatibility of materials is established through in vivo experiments found in literature.

Material	**Young's modulus** [Pa]	**Poisson's ratio [-]**	**Water vapor permeability** $[(g\ mm)m^{-2}day^{-1}]$	**Dielectric constant**	**Reference**
Silicon	$165 \cdot 10^9$	0.22	0.0	11	[90]
Parylene C	$2.76 \cdot 10^9$	0.4	0.08	3.1	[91]
Polyimide	$2.76 \cdot 10^9$	0.34	17.5	3.5	[92]
PDMS	$1.32 \cdot 10^6$	0.5	181.4	2.7	[81], [93]
Neural tissue	$9.2 \cdot 10^3$	0.46	-	-	[94]

Table 2.1: The Young's modulus and Poisson ratio of substrate materials used for neural interfaces compared to the properties of neural tissue. Softer substrate materials mimic more accurately neural tissue and are hypothesized to cause a less severe chronic tissue response.

A widely used form of PDMS is Sylgard 184 (Dow Corning). It is made by mixing two chemicals: a silicone agent and a curing agent mixed (often) in a ratio of 10:1. Addition of silicone oils to Sylgard 184 can lower its flexibility [81]. PDMS is a viscous material before curing, after which it becomes elastomeric. Spin coating PDMS can lead to thicknesses of 8 μm [95]. Due to the viscoelasticity of PDMS, thinner layers through spin coating alone are not feasible. However, diluting PDMS with hexane can result in 100 nm thin layers [96]. The thickness of PDMS is problematic for forming a passivation layer, which ideally is as thin as possible.

2.4. Processing techniques

2.4.1. Spin coating

Spin coating is a fabrication technique used to produce uniform thin films. It is done by rapidly rotating a surface covered by a solution. The solution has to contain the material to be deposited, which restricts the materials that can be deposited. The result is a uniform thin layer of viscous material, which should be baked afterwards to solidify the layer.

When discussing spin coating, it is helpful to divide the process into four stages: (1) dispensation, (2) acceleration, (3) outflow, (4) evaporation. Dispensation covers the substrate surface with the spin coating liquid. Rotational acceleration of the substrate starts the spin coating and brings the liquid to the edge of the surface. Outflow occurs when liquid leaves the surface under high rotational speed. Evaporation of the liquid happens due to the airflow on the surface.

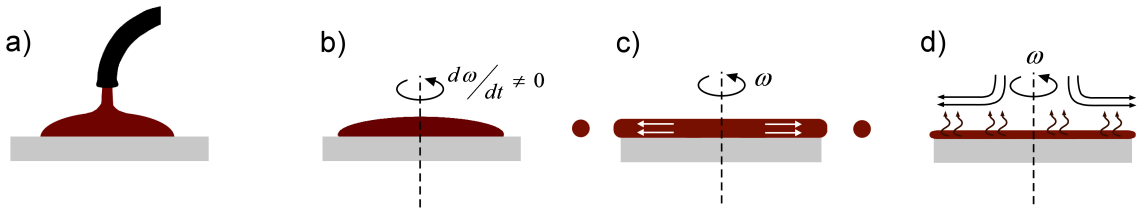

Figure 2.11: The four stages of spin coating: (a) dispensation, (b) acceleration, (c) outflow, and (d) evaporation. The figure is adapted from [97].

Following Hellstrom [97], spin coating can be analytically approximated. The following assumptions have to be made:

- The rotating surface is horizontal so that radial gravitational components can be ignored.
- The liquid layer thickness is so small that differences in gravitational potential normal to the surface can be neglected.
- The radial velocity is small enough that Coriolis forces can be ignored.
- The liquid layer is so thin that evaporation is assumed independent of height.
- The total volume of the liquid is the sum of the solvent and solute.
- The evaporation rate is constant.

Equating the viscous and centrifugal forces produces

$$-\eta \frac{\delta^2 v}{\delta z^2} = \rho \omega^2 r \tag{2.6}$$

with the viscosity η, the radial velocity v, the liquid density ρ, the spin speed ω, all defined at coordinates (r, θ, h).

$$\frac{dS}{dt} = -c \frac{1}{r} \frac{\delta(rq)}{\delta(r)} = -2Kh^3 c \tag{2.7}$$

$$\frac{dL}{dt} = -2Kh^3(1-c) - e \tag{2.8}$$

$$(1-c)\frac{2\omega^2 h^3}{3\beta} = e \tag{2.9}$$

$$h_f = S_f \approx c_0 h_{\frac{1}{2}} \approx \left(\frac{3\beta_0 e}{2\omega^2(1-c_0)}\right)^{\frac{1}{2}} c_0 \tag{2.10}$$

$$h_f = k c_0 (1-c_0)^{-\frac{1}{3}} \omega^{-\frac{1}{2}} \beta_0^{\frac{1}{3}} \tag{2.11}$$

filling in $c_0 = 0.01$ and $\beta = \frac{\eta}{\rho} = 1.5 \cdot 10^{-5} m^2 s^{-1}$ for PEDOT:PSS (Clevios PH1000) allows fitting of one parameter k to experimental data.

Spin coating is widely used for creating thin layers of PEDOT:PSS due to its uniformity, ease of use, and process adaptability. Other options include spray coating, chemical vapor deposition, electrodeposition, inkjet printing, and doctor blading [39]. These techniques do not achieve the same uniformity and sometimes require bulky equipment, which is not readily available for PEDOT:PSS at the TU Delft.

2.4.2. Oxygen plasma

Oxygen plasma is a surface treatment technique that is used for different purposes. High-power oxygen plasma can strip photoresists and thus clean wafers. Low-power oxygen plasma can create hydroxyl groups on the surface of apolar substrates and increase their hydrophilicity. Fundamental to the oxygen plasma treatment is the creation of an oxygen plasma through high radio frequency (RF) power at low pressures. Oxygen gas is pumped into a low-pressure chamber and energized, usually at 13.56 MHz. The energized oxygen ions are highly chemically active and react especially well with carbohydrates, creating water vapor and carbon dioxide, which is pumped out of the low-pressure chamber. Important parameters for oxygen plasma treatment are the gas flow, the RF power, and the duration of the treatment. Gasflow is expressed in standard cubic centimeters per minute (SCCM), RF power in Watts (W), and duration in seconds (s).

2.4.3. Lithography

Lithography is a technique to create microscale or even nanoscale patterns into photoresist solutions. Photoresist often consists of a polymer that alters its solubility upon exposure at a certain frequency and intensity. Positive photoresist is normally insoluble and becomes soluble in its corresponding developing chemical. Negative photoresist is normally soluble and becomes insoluble upon exposure. Photoresists are usually a few micrometers thick, though some types can become thicker than 10 μm [98]. Before exposing, the photoresist needs to be soft baked to make it hardened after its liquid deposition. Exposure is performed and follows the Beer-Lambert law

$$I = I_0 e^{-\alpha d} \tag{2.12}$$

where I is the intensity [mJ/cm^2] at depth d [μm] in the resist, I_0 [mJ/cm^2] is the intensity at the surface, and α [μm^{-1}] is the absorption coefficient at the exposure wavelength. After exposure, the photoresist needs to be baked once more (so-called post exposure bake) to improve the exposed concentration pattern [99].

2.4.4. Atomic force microscopy

Atomic force microscopy (AFM) is an imaging technique through scanning with a physical probe. It can attain resolutions up to several nanometers. It is useful for imaging surfaces beyond the optical diffraction limit. Additionally, AFM has been used to investigate the phase separation in PEDOT:PSS [58] and uniformity [39]. The working principle of AFM is that a cantilever with a tip is oscillated at its eigenfrequency to make contact with the sample surface. Upon contact, the probe, having a diameter between 2-12 nm [100], touches surface on the nanoscale while its effects become visible in the beam oscillation at the microscale. The microscale effects are translated by measuring the reflection of a laser shone upon the top side of the silicon beam.

2.4.5. Four point probe

A four-point-probe is a method to measure sheet resistance or sheet conductivity. Four equally spaced metal probes are placed on the material to make contact. The outer two probes apply a defined current while the inner two probes measure the voltage. The sheet resistance ρ can be computed from the measured resistance R_m by

$$\rho = \frac{\pi}{ln(2)} R_m t = \frac{\pi}{ln(2)} \frac{\Delta V}{I} t \tag{2.13}$$

where t is the layer thickness. The $\frac{pi}{ln(2)}$ comes from assuming the thickness of the layer to be negligible compared to the probe spacing. Additionally, for small samples the diameter of the sample can influence the conductivity measurement [101]. It is therefore not as accurate as a Van der Pauw structure for sheet conductivity but widely employed in literature [58], [60], [69], [79], [102].

2.5. Previous microelectrode array devices

In this section, state-of-the-art microelectrode array devices are discussed. The devices are categorized in three groups: PDMS-substrate without PEDOT:PSS, PEDOT:PSS electrode (coatings) without PDMS substrate, and PEDOT:PSS electrodes with PDMS substrate. In Table 2.2, a comparison of state-of-the-art flexible microelectrode array devices is shown.

2.5.1. PDMS based microelectrode arrays

Other researchers have applied PDMS as substrate material for microelectrode arrays. Guo et al. [103] used PDMS as substrate material and demonstrated recording of feline muscle activity. PDMS is a difficult material for obtaining thin films due to its high viscosity and chemical inertness after curing. For example, spin coating PDMS at 8000 rpm produces a film of 8 μm thick [95]. Guo et al. [104] proposed a via fabrication technique that allows thin layers to via through PDMS by guiding them down a PDMS patterned slope. This comes at a cost of spatial density however. Zia et al. [105] demonstrated PDMS-based microelectrode arrays capable of in vivo recording electromyography signals in songbirds. They created 3D electrode structures using a photoresist reflow technique to overcome the PDMS layer thickness. The relatively large minimal thickness is problematic for the microfabrication process: 2D thin films cannot be readily deposited on PDMS to form microelectrode arrays, since no reliable connection can be made over such step heights or the electrodes will be spaced further away from the neurons.

2.5.2. PEDOT:PSS based microelectrode arrays

Since 2003, PEDOT:PSS has been applied in microelectrode array devices, both in academic and industrial settings. Substrate materials are parylene C, polyimide, and silicon. Figure 2.12 summarizes the evolution of PEDOT:PSS microelectrode array technology and emphasizes highlights.

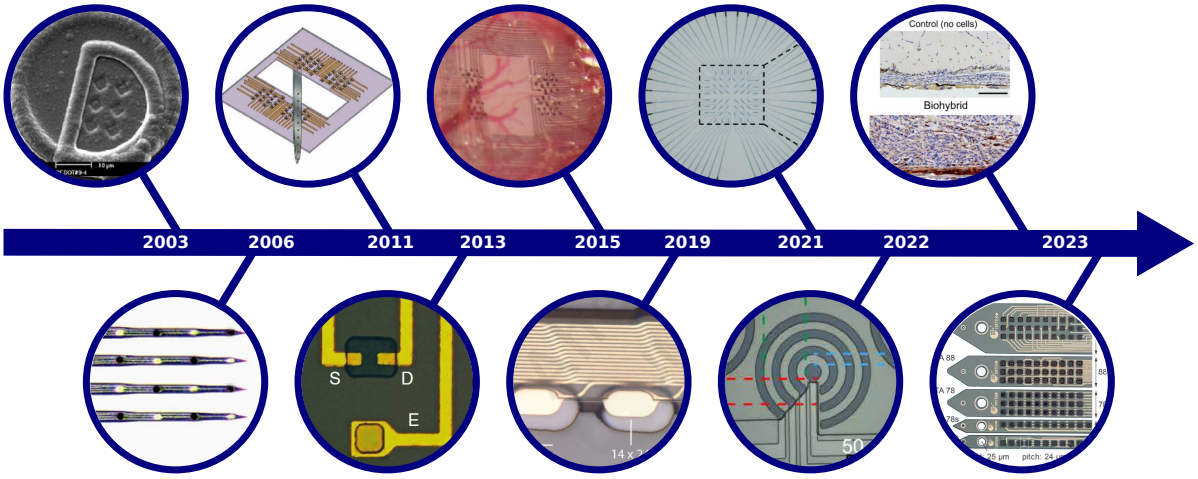

Figure 2.12: An illustrative timeline of microelectrode array technology using the conducting polymer PEDOT:PSS. In chronological order: in 2003, Cui and Martin [53] were the first to electrochemically deposit PEDOT:PSS on neural probes. In 2006, Ludwig et al. [43] performed the first chronic recordings using PEDOT:PSS coated electrodes and compared it to uncoated electrodes. Khodagholy et al. enhanced PEDOT:PSS microfabrication for electrode arrays [72], in organic electrochemical transistor configuration [106], and optimized the process in NeuroGrid [73]. Neuralink [107] investigates PEDOT:PSS microelectrode array fabrication in 2019, signaling interest of the industry. Transparent devices are demonstrated by Middya et al. [102] in 2021. Uguz and Shephard [20] show novel bipolar stimulation using PEDOT:PSS microelectrodes in 2022. In 2023, Rochford et al. [108] demonstrate a successful biohybrid microelectrode array. The same year, multilayered and more compact structures are fabricated by Boehler et al. [76].

2.5.3. PEDOT:PSS/PDMS based microelectrode arrays

In literature only two microelectrode arrays were found that employed a combination of PEDOT:PSS and PDMS [30], [31]. Blau et al. [30] fabricated microchannels in PDMS using a two-level replica-forming strategy. The channels were coated with PEDOT:PSS for electrodes and a mixture of PEDOT:PSS and graphite particles for the tracks to enhance conductivity. They measured epidural, epicortical, and acute cardiac neural activity with their device containing 60 electrodes. Filho et al. [31] patterned channels in PDMS using a mold and then filled the channels with a ink of PEDOT:PSS mixed with dimethyl-sulfoxide (DMSO). To isolate channels, another slab of PDMS was thermally bonded on top. The device with 4 electrodes measured local-field potentials in Wistar rat brains. Additionally, PEDOT:PSS and PDMS were combined in a stretchable resistor that measures contractility and neural activity by Oldroyd et al. [32]. During the thesis project, another article was published that combined PEDOT:PSS and PDMS for microelectrode array technology [109]. Using a silicon mold, PDMS micropillars with diameters of 4 μm or 7 μm were fabricated. On top of the micropillars, gold was evaporated and then PEDOT:PSS was electrodeposited. One pillar did not form one electrode however. With a SU-8 patterning technique, they fabricated $\approx$100 μm diameter electrodes. Due to mechanical mismatch, the Au layer on PDMS showed cracking (see Figure 2.13h). The obtained SNR was almost 40 dB higher than other examples of the state-of-the-art. This is puzzling, though the approaches for computing the SNR, usage of anasthetics, and spike sorting algorithms differ between research groups and might account for this large disrepancy. These devices are pictured in Figure 2.13. The devices did not reach electrode diameters smaller than 100 μm and substrate thicknesses smaller than 500 μm (and 80 μm for [109], as was discovered halfway during the project). Filho et al. reported in vivo neural recordings and did cell staining to determine the chronic immune response to the implant. These results in themselves are promising and demonstrate the biocompatibility of PEDOT:PSS and PDMS devices, yet lack the spatial resolution and performance to compete with state-of-the-art based on parylene C or polyimide. Addressing the issue of spatial resolution of PDMS microelectrode array devices has been researched for longer [27], [103], [110]. Other materials, such as parylene C, are difficult to use as passivation layer on top of PDMS due to poor adhesion.

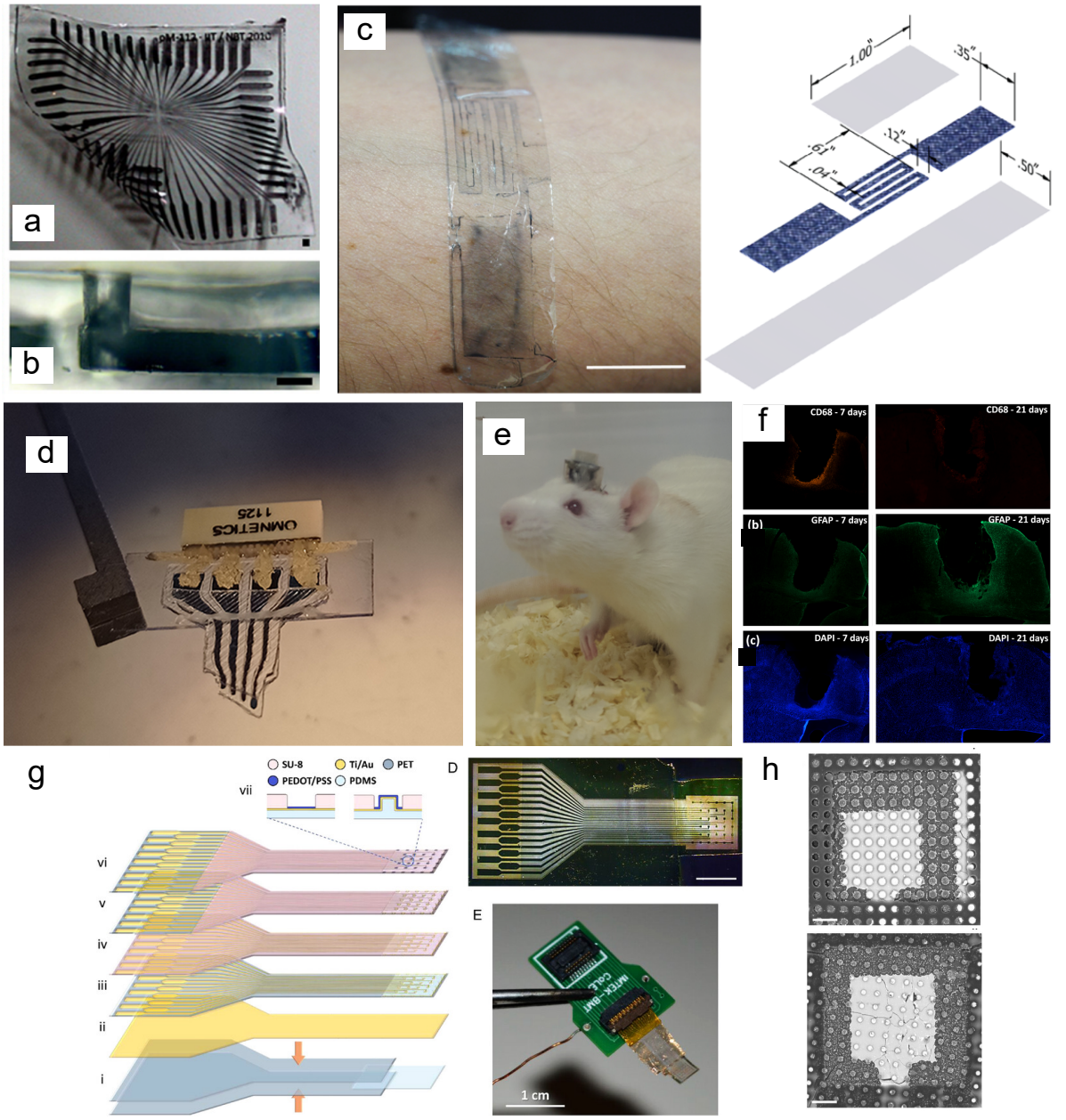

Figure 2.13: Microelectrode arrays in literature that combine PEDOT:PSS and PDMS into an all-polymeric device. Blau et al. [30] 3d printed (a-b) a PEDOT:PSS and PDMS MEA. Oldroyd et al. [32] created a (c) stretchable sensor for measuring gut electrophysiology and contractility. Filho et al. made (d) four PEDOT:PSS microelectrodes on PDMS, (e) implanted them in mice and recorded action potentials, (f) imaged the immune response through cell staining, (g) the Neural Pillars from Lunghi et al. [109], and (h) a SEM image of the pillars on top of one of their electrodes.

Mode	Substrate material	Flexural stiffness $[Nm^{-2}]$	Electrode material	Electrode area $[cm^2]$	Impedance @ $1kHz$ [Ω]	Impedance area $[\Omega cm^2]$	CIC $[\mu Ccm^{-2}]$	SNR	Tests	Reference
R	PDMS	$1.08 \cdot 10^{-4}$	PEDOT:PSS	$1.13 \cdot 10^{-4}$	$1.2 \cdot 10^{6}$	135.71	-	4.00	in vitro	[30]
R	PDMS	$1.87 \cdot 10^{-7}$	Au	$1 \cdot 10^{-2}$	$5.8 \cdot 10^{3}$	58.0	-	-	in vitro	[103]
R	PDMS	$5.55 \cdot 10^{-5}$	PEDOT:PSS	$1.26 \cdot 10^{-3}$	$7.40 \cdot 10^{3}$	9.30	-	12.00	in vivo	[31]
R & S	PDMS	$4.3 \cdot 10^{-8}$	PEDOT:PSS	$1 \cdot 10^{-4}$	$2 \cdot 10^{3}$	0.2	-	60	in vivo	[109]
R & S	PaC	$4.74 \cdot 10^{-8}$	PEDOT:PSS	$7.07 \cdot 10^{-6}$	$9.0 \cdot 10^{5}$	0.64	340	-	in vivo	[20]
R & S	PI	$3.06 \cdot 10^{-8}$	PEDOT:PSS	$3.24 \cdot 10^{-6}$	$3.32 \cdot 10^{4}$	0.11	32	3*	in vivo	[76]
R	PI	$6.37 \cdot 10^{-10}$	PEDOT:PSS	$4.91 \cdot 10^{-6}$	$7.0 \cdot 10^{5}$	3.44	-	12.05	in vivo	[22]
R & S	PaC	$4.78 \cdot 10^{-8}$	PEDOT:PSS	$4.91 \cdot 10^{-6}$	$3.89 \cdot 10^{4}$	0.35	-	7.70*	in vivo	[85]

Table 2.2: Comparison table for state-of-the-art microelectrode arrays. The arrays are ordered for mode (R = recording, S = stimulation), substrate material, simulated flexural stiffness using equation 2.4, electrode material, electrode area, electrochemical impedance at 1 kHz, the normalized impedance area, charge injection capacity (if reported), demonstrated signal-to-noise ratio (SNR), and whether testing was done in vitro or in vivo. * SNR was not reported in the article but approached from spike activity diagram.

2.6. Summary

The objective of the literature study is to identify key findings and gaps in understanding of the fabrication of PEDOT:PSS microelectrode arrays on PDMS substrates. The application in mind for this technology is the integration of microelectrode arrays in microfluidics or organ-on-chip devices. From the literature review, it was observed that especially the spatial resolution of PEDOT:PSS electrodes on PDMS are outperformed by PEDOT:PSS electrodes on other substrates. Additionally, quantitative analysis shows that single-unit activity recording of neurons requires electrodes with diameters smaller than 100 μm [34]. In literature, the smallest PEDOT:PSS electrode on PDMS currently is 120 μm in diameter. Therefore, the main research question of the MSc thesis is formulated as:

How can sub-100 μm diameter PEDOT:PSS-only electrodes be fabricated on PDMS substrates thinner than 70 μm for neural interface applications?

The requirement of PDMS being thinner than 70 μm comes from desired competitiveness of device flexibility compared to state-of-the-art 4 μm-thick parylene C or 4 μm thick polyimide, which flexural stiffness is in the range of $3 - 5 \cdot 10^{-8}$ Pa s. Following Equation 2.4, PDMS reaches a bending stiffness of $5 \cdot 10^{-8}$ at a thickness of $\approx 70\,\mu m$.

Another important question, supporting the main research question, is

What solvents should be added to PEDOT:PSS for optimal microelectrode array performance on a PDMS substrate?

The variety of solvents and treatment techniques is large, so optimizing the solvents for microfabrication of microelectrode arrays on PDMS is of importance.

Other main takeaways from the literature review are listed below:

- The morphology of PEDOT:PSS is crucial for its electrical properties. Great care should be spent to optimize and understand the control of these properties.
- Various solvents are used to change the characteristics of PEDOT:PSS, both mechanical and electrical. Often, solvents induce a change in morphology that influences PEDOT:PSS material properties. For example, GOPS is a silane and can hypothetically create strong bonds between silane based materials, such as PDMS, and PEDOT:PSS.
- PEDOT:PSS significantly increases the electrochemical capacitance due to volumetric interactions with the electrolyte. The increase of capacitance is beneficial for reducing the electrode impedance in the frequency domain of interest, which can improve signal recording quality.
- PDMS is a relatively thick material. Spin coating can reach thicknesses >5 μm. Dilution with hexane can create thin PDMS films of 100 nm, but hexane is not readily available in the cleanroom. A method to connect thin films through the thick PDMS layer is paramount for device fabrication.
- Surprisingly few microelectrode array devices exist that combine PEDOT:PSS and PDMS. A gap is left in understanding the material interactions and the impact on the microfabrication of such devices.

3
Layer characterizations

3.1. Methodology

One of the starting points was the characterization of layers of PEDOT:PSS and a selection of its solvents on different substrates, among which PDMS. The literature study yielded many investigations into PEDOT:PSS with EG (5% v/v), GOPS (1% v/v), and DBSA (0.5% m/m). However, PEGDE instead of GOPS was little researched even though it has potential in microfabrication processes due to its chemical difference to GOPS. It led to the first explorative experiment that characterizes spin coated layers of PEDOT:PSS on SiO2 (borosilicate glass), Au, and PDMS. The layers are illustrated in Figure 3.1.

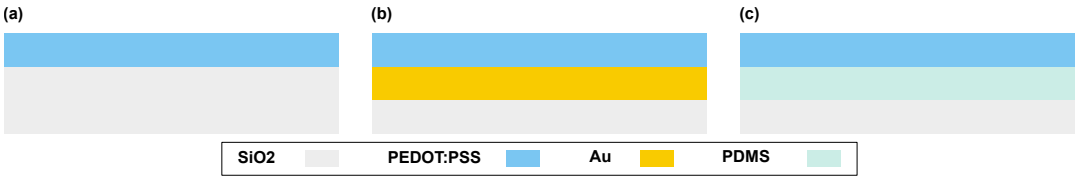

Figure 3.1: Illustration of the different combinations of PEDOT:PSS and substrate materials. PEDOT:PSS is prepared with different crosslinkers, respectively GOPS and PEGDE. PEDOT:PSS is spin coated on borosilicate glass, see (a), on Au evaporated on borosilicate glass, see (b), and on spin coated PDMS on borosilicate glass, see (c).

The material properties of PEDOT:PSS are influenced by added solvents. To explore applicability of GOPS and PEGDE and their necessity for a wettability agent such as DBSA, the experiment aims to characterize:

- The thickness and uniformity of the spin coated layers of PEDOT:PSS and PDMS. For precise dimensional control, highly uniform and thin layers are required.
- The conductivity of the PEDOT:PSS layer. Minimizing the electrode impedance requires high conductivity.
- The electrochemical impedance of PEDOT:PSS and phosphate-buffered saline (PBS). Cyclic voltammetry and electrochemical impedance are figures-of-merit for electrode performance [16].
- The adhesion of PDMS and PEDOT:PSS. For long-term stability, strong adhesion is required.

The corresponding cleanroom flowchart can be requested by mailing the author or the corresponding supervisor. First, a 4-inch borosilicate glass wafer (University Wafers) is cut into 2 cm x 2 cm dies and the dies are cleaned with 99% HNO_3 for 10 minutes. Then the dies are rinsed in deionized water for 10 minutes and blow dried using a nitrogen gun. The dies are stored in ISO 5 wafer boxes. PEDOT:PSS was bought from Hereaus (PH-1000) and mixed first with EG (5% v/v) and DBSA (0.5% m/m). Due to the high viscosity of DBSA, volume control is expected to be difficult. Therefore, mass control is chosen for DBSA only using a weighing scale. The v/v ratios translate directly into m/m-ratios since DBSA has a density of 1.03 g/cm^3. The mixture is thoroughly mixed and degassed using an Thinky ARE-250 for 2 minutes at 2000 rpm. Subsequently the crosslinker, GOPS or PEGDE, is added in 1% v/v. The mixture is then again mixed and degassed for 2 min at 2000 rpm. Additionally, the SiO_2 surface is activated using oxygen plasma (Diener Atto) at 50 SCCM and 70 W for 60s. The die is then placed on the chuck in the spin coater and kept in place by a vacuum or water adhesion. The PEDOT:PSS mixture with solvents is filtered with a 0.45 μm polytetrafluoroethylene (PTFE) filter directly before applying it on the substrate. The substrate is then spin coated at one rotational speed for 60 seconds, excluding a starting ramp time of 5 seconds with a speed increasing at 100 rpm/s. The spin coating process is repeated on different wafers for other rotational speeds to retrieve a spin curve of PEDOT:PSS on borosilicate glass. After spin coating, a soft-bake at 110°C for 1 minute is performed on a hotplate, followed by a hard bake at 110°C for 60 minutes in an oven (Memmert).

For the PEDOT:PSS on Au, 10 nm Ti and 200 nm Au is evaporated on a clean borosilicate glass wafer using an e-beam evaporator (CHA Std.). After evaporation, the wafer is cut into 2 cm x 2 cm dies using the precision glass cutter outside the cleanroom. The dies are taken into the cleanroom and cleaned again using HNO_3. The process of spin coating is performed similar to the PEDOT:PSS layer on SiO_2. For PEDOT:PSS on PDMS, a layer of PDMS (Sylgard 184, Dow Corning) is applied on a clean borosilicate glass wafer. First, the silicone agent is mixed with the curing agent in a 10:1 ratio. Then the mixture is degassed and mixed using the Thinky ARE-250. Subsequently, the mixture is spin coated on the SiO_2 wafer. The process is repeated on different wafers at other rotational speeds. After spin coating, the PDMS is degassed in a vacuum chamber for 2 hours to remove trapped air bubbles. The PDMS is then cured at 90°C for 60 minutes. The reason for selecting a wafer size substrate for PDMS was that only wafer-size chucks were available at the time. PDMS is hard to clean or remove from small holes, so other approaches were not suitable for sustainable cleanroom practices.

Having fabricated the layers, they are ready to be characterized. The layers are first inspected under a microscope (Olympus). Then the transmittance is measured (LAMBDA 950, Perkin Elmer). The transmittance spectrum of PEDOT:PSS can be related to the thickness as in [102]. Subsequently, a scratch test is performed while still in the cleanroom. To measure the thickness of the PEDOT:PSS or PDMS layer, a scratch is made in the layer, reaching the SiO_2 substrate. The scratches are made at different radii to gain insight into the uniformity of the surface. The PDMS wafers used for a scratch test cannot be used to spin coat PEDOT:PSS on top, so a duplicate wafer with equally thick PDMS wafer is used, i.e. spun at the same rotational speed with the same PDMS mixture. The step height of a scratch is measured using a profilometer (Bruker Dektak 8). The step height is taken as average between the higher and lower plane. The variance of the higher plane is taken as measure of the non-uniformity of the substrate. The sheet conductivity of the PEDOT:PSS layer is measured using a four point probe setup (Osilla). The electrochemical impedance is measured using a three electrode setup with Ag/AgCl reference electrode and Pt mesh counter electrode, connected to a Metrohm Autolab PGSTAT100N. It is shown in Figure 3.2. The electrochemical impedance spectrum (EIS) and the cyclic voltammetry (CV) diagram are extracted. The samples are cleaned using DI water after tests and a dehydration bake at 110°C for 10 minutes is performed.

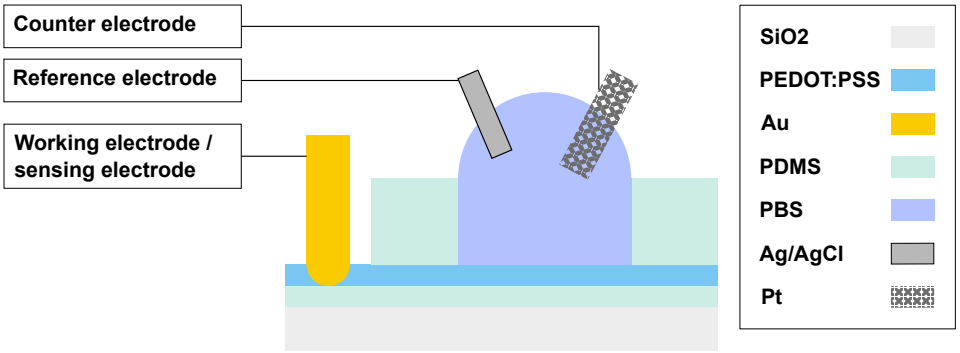

Figure 3.2: Schematic of the electrochemical setup used to measure the electrochemical impedance spectrum and the cyclic voltammetry diagram.

The adhesion between PEDOT:PSS and PDMS is tested through a Kapton tape test. A matrix of 4x6 squares of 5 mm x 5 mm are cut in only the PEDOT:PSS and PDMS layers using a precision glass cutter (Utile). Kapton tape is applied on the matrix and pulled off in one motion. The sample is inspected afterwards to see what percentage of the squares is left on the substrate and whether the Kapton tape pulled off any material. This characterization does not provide mechanically well-quantified data but rather an indication of the adhesion strength between the two layers.

The experiment aimed to fabricate thin films of 100 nm and 300 nm thick. The PEDOT:PSS solutions were spin coated at 2000 rpm and soft baked at 80°C to achieve a layer thickness of 100 nm. For 300 nm, the procedure was repeated three times so to stack three layers of 100 nm on top of another. This method was also reported by [85] and [20], though at different soft bake temperatures.

3.2. Results

The results of the experiment are detailed here. The results include microscope images, thickness, transmittance, conductivity, cyclic voltammetry diagrams, and electrochemical impedance spectra.

3.2.1. Microscope images

The microscope images were taken with an Olympus microscope. The samples were placed on a blue cleanroom tissue while imaged in a monochromatically lighted area. The transparent samples on SiO_2 have therefore a yellow and green coloring, though outside the cleanroom the transparency and faint blue color can clearly be observed, see Appendix B.1.

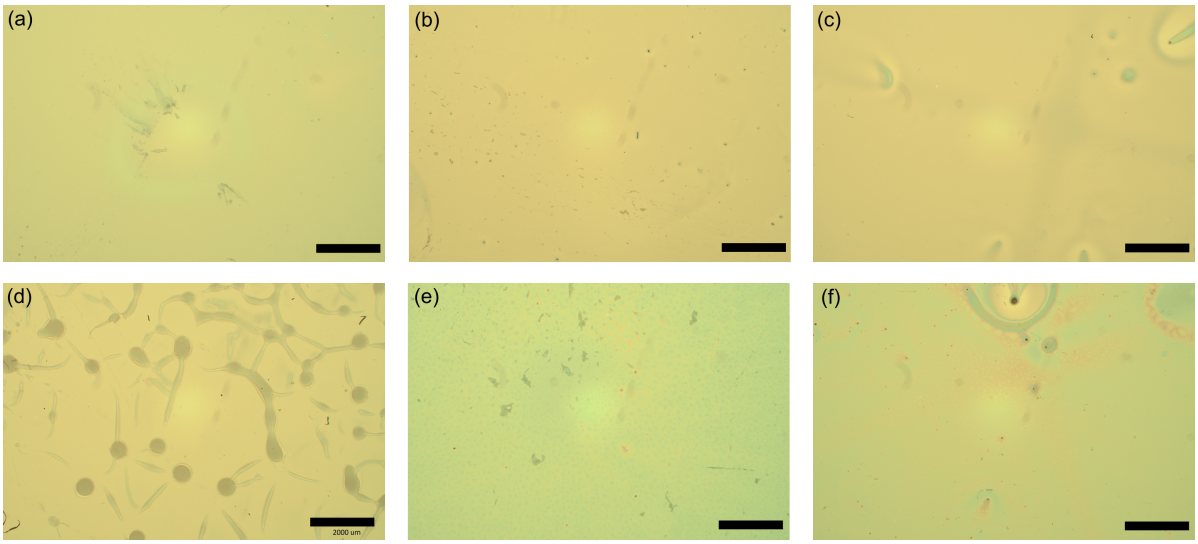

Figure 3.3: Microscope images of the samples on SiO_2 with magnification 2.5x. PEDOT:PSS is spin coated 1x at 2000 rpm and mixed with (a) EG, GOPS, and DBSA, (b) EG, PEGDE, and DBSA, (c) EG and PEGDE, (d) EG and GOPS, and spin coated 3x at 2000 rpm and mixed with (e) EG, PEGDE, and DBSA, (f) EG and PEGDE. The samples with PEDOT:PSS/GOPS were not spin coated three times due to shortage of the mixture. PEDOT:PSS/GOPS without a wettability agent (see d) produces poor film results since the surface tension of PEDOT:PSS causes it to aggregate. The sample is therefore discarded for further characterizations. PEDOT:PSS/PEGDE without DBSA shows bubble formation in the film. The black scale bar is 2 mm.

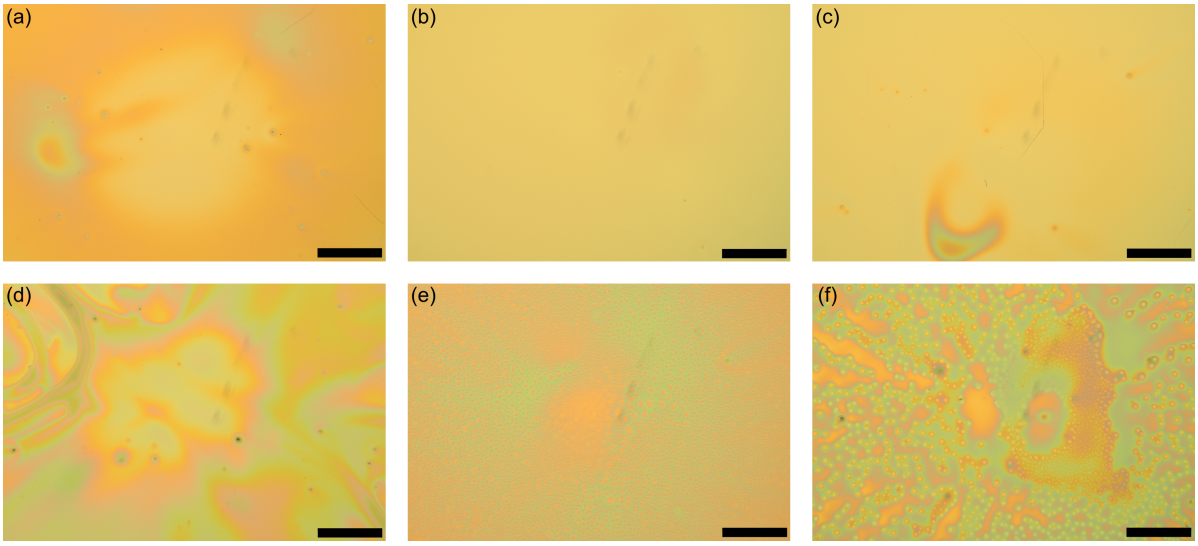

Figure 3.4: Microscope images of PEDOT:PSS on Au with magnification 2.5x. PEDOT:PSS is spin coated 1x and mixed with (a) EG, GOPS, DBSA, (b) EG, PEGDE, DBSA, (c) EG and PEGDE, and spin coated 3x mixed with (d) EG, GOPS, DBSA, (e) EG, PEGDE, DBSA, (f) EG and PEGDE. 1x spin coating leads to evenly colored images, indicating uniform layers. 3x spin coating leads to comet-like patterns, indicating non-uniformities. The black scale bar is 2 mm.

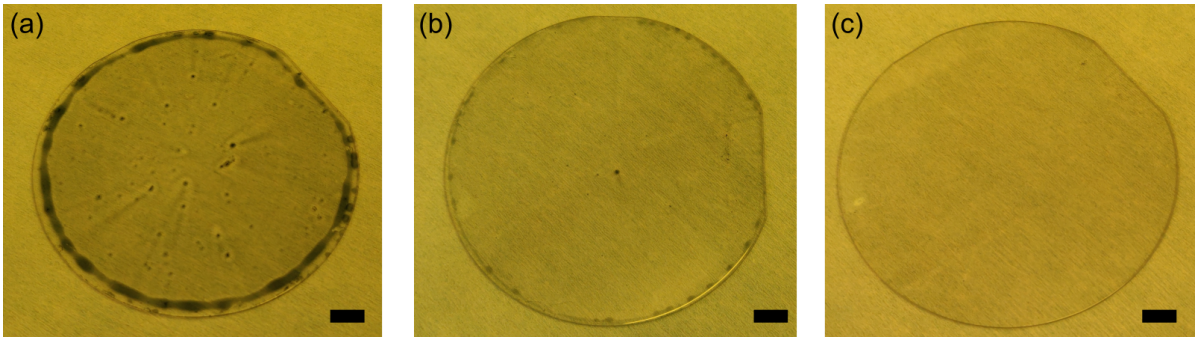

Figure 3.5: Pictures of SiO_2 wafers with first PDMS and then PEDOT:PSS on top. PDMS was spin coated at 2000 rpm and PEDOT:PSS was spin coated at (a) 500 rpm, (b) 1000 rpm, and (c) 1500 rpm. No microscope images were taken since it would zoom in on an arbitrary part of the wafer. The scale bar is 1.0 mm.

3.2.2. Transmittance spectrum

The first characterization of the PEDOT:PSS layers on SiO_2 was a transmittance spectrum measurement. Light at specific wavelengths is shone through the sample and, after several reflection stages, measured by a detector. The detected radiation power is related to the initial power, from which the transmittance is determined. The formula for transmittance is

$$T = \frac{P_{transmitted}}{P_0} \tag{3.1}$$

where T is the transmittance, $P_{transmitted}$ the transmitted radiation power, and P_0 the initial radiation power. Since PEDOT:PSS becomes less transparent as the thickness increases, the transmittance can be related to the thickness. PEDOT:PSS should be treated as distinct materials for different dissolved crosslinkers due to its major effect on material structure.

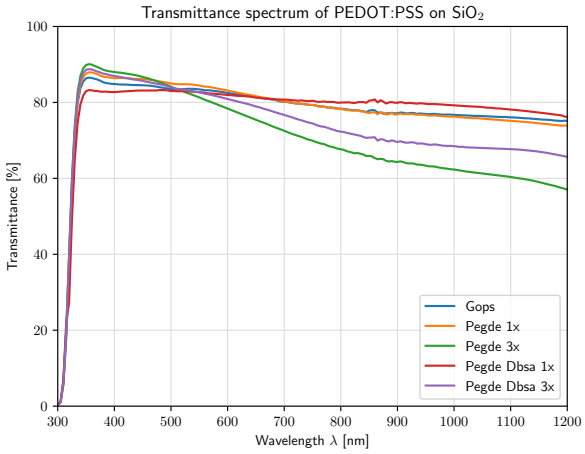

Figure 3.6: The transmittance profile of the spin coated PEDOT:PSS layers with different solvents and processes. PEDOT:PSS is denoted by the crosslinker and wettability agent.

From Figure 3.6, it is indicated that PEDOT:PSS/PEGDE without DBSA has lower transmittance than PEDOT:PSS/PEGDE with DBSA, even though the latter is around 30-50 nm thicker. One explanation is that the bubble formation in PEDOT:PSS/PEGDE without DBSA, and thus lower uniformity, diffracts light or causes higher absorption. The transmittance values are 10-15% lower than [102], but comparable with [111]. Access to the transmittance measurement system was limited, so transmittance is not used in further characterizations. It was also the reason that the PEDOT:PSS on PDMS samples are not measured.

3.2.3. Thickness measurement

After curing, the thickness of the material is determined via a scratch test. PEDOT:PSS and PDMS are relatively soft materials and can therefore be easily removed using sharp objects. It was found that a 20G (0.9 mm) needle worked best to create a sharp edge without debris. The layer thickness was measured using a profilometer (Veeco DEKTAK 150). The thicknesses for PEDOT:PSS mixtures are shown in Figure 3.7. For PDMS, a spin curve was obtained by spinning at 1500, 2000, and 2500 rpm. A spin curve of PEDOT:PSS/GOPS+DBSA was already obtained by M. Shah, a PhD candidate from our section. The theoretical model of Hellstrom [97] was fitted to the data points and is and is shown in Figure 3.8 for PEDOT:PSS and PDMS.

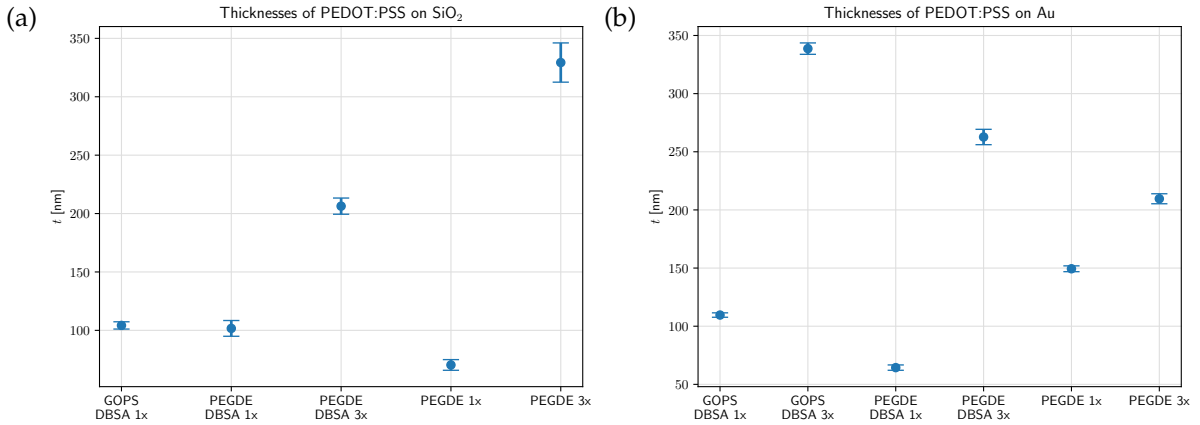

Figure 3.7: The layer thickness determined by a scractchtest and a profilometer. Comparing the PEDOT:PSS layers on (a) SiO_2 and (b) Au, it is interesting to note that PEDOT:PSS/PEGDE on SiO_2 is almost a third of the thickness of PEDOT:PSS/PEGDE on Au. An opposite trend is observed for PEDOT:PSS/PEGDE+DBSA: on SiO_2, PEDOT:PSS/PEGDE+DBSA is thicker than on Au.

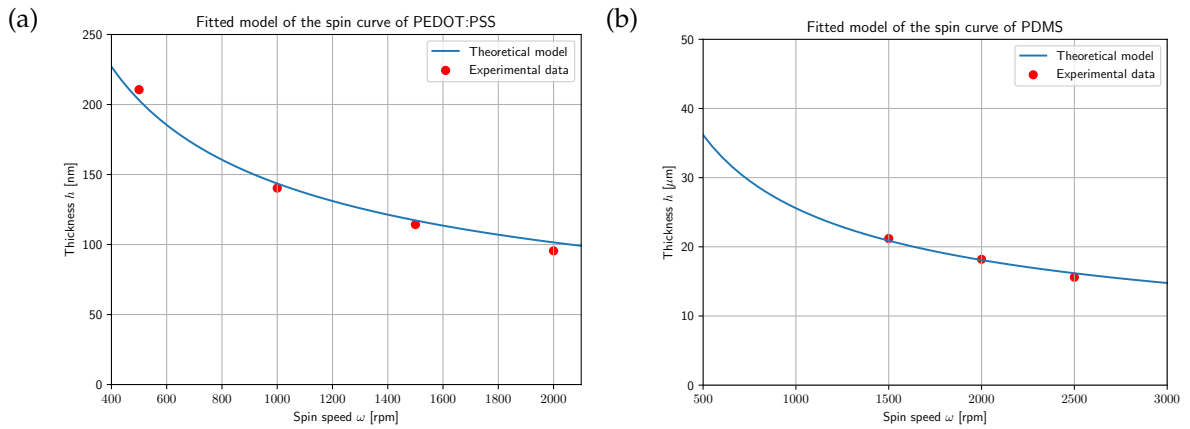

Figure 3.8: Theoretical model of Hellstrom [97] fitted to experimental data of (a) PEDOT:PSS and (b) PDMS. For PEDOT:PSS, the evaporation constant (and fitting parameter) is $k = 0.945 \cdot 10^{-3}$ and gives $R^2 = 0.9852$. For PDMS, the evaporation constant is $k = 1.3436 \cdot 10^{-4}$ and gives $R^2 = 0.9717$.

As can be seen in the model for PDMS, the thickness that can be achieved with higher spin speeds appears to approach an asymptote. The asymptotic behavior is experimentally confirmed by [95], meaning that achieving PDMS layers thinner than 8 μm is not feasible through spin coating.

The layer of PEDOT:PSS on PDMS was measured using a scratch test as well, but surprisingly yielded a thickness of 0.8 μm. Closer investigation with focused-ion beam scanning electron microscopy (FIB-SEM) did not yield satisfactory images due to the high charging of PEDOT:PSS and low conductivity of PDMS. The images taken are shown in Appendix B.2. The transmittance of the sample is comparable to the sample of PEDOT:PSS/GOPS+DBSA at 100 nm, which led to believe that the PDMS layer may have been thicker due to variance from spincoating, which is a sensitive process to small pertubations.

Originally, the intention was to measure at least two samples per PEDOT:PSS mixture. However, a major

limitation of these results is the fact that in most cases, only one sample was measured. The reason for this was the absence of a die-level chuck for spin coating. It resulted into spin coating with a different approach for securing the sample to the chuck using water adhesion. The yield of this method was not great, as the die could fly off during spin coating if the water adhesion was too weak.

3.2.4. Conductivity

The conductivity of the spin coated PEDOT:PSS layers on SiO_2 was measured using a four-point-probe setup. The conductivity of PEDOT:PSS layers on gold could not be measured with a four point probe, since the probes would make contact with the Au substrate and mainly measure the conductivity of Au, which is $4.5 \cdot 10^5$ S/cm. The results are shown in Figure 3.9a. The results are in line with [69], where PEGDE results into higher conductivity than GOPS as crosslinker. The wide variance makes the conductivity harder to interpret accurately, since variance of the four point probe measurement and of the thickness measurement add up for computing the conductivity.

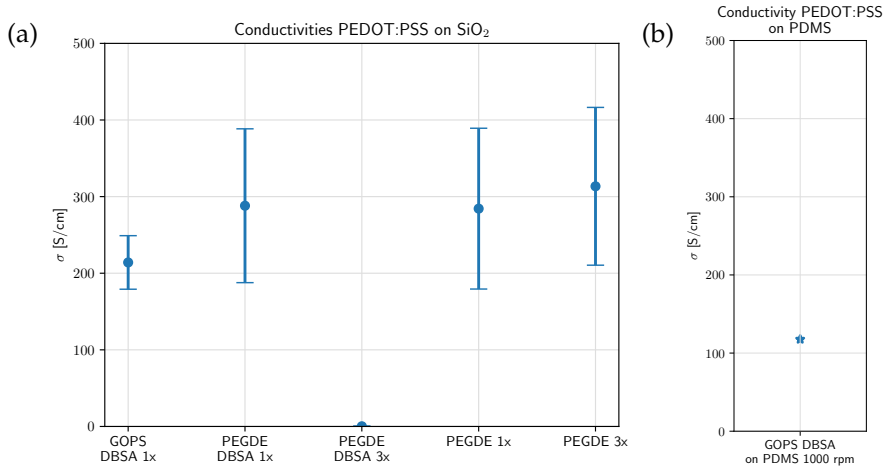

Figure 3.9: The conductivities of (a) PEDOT:PSS on SiO_2 with the solvents GOPS+DBSA, PEGDE+DBSA, and PEGDE and (b) on PDMS. The resistance values were measured with a four point probe and converted to conductivity using Equation 2.13 and $\sigma = \frac{1}{\rho}$. The sample of PEDOT:PSS/PEGDE+DBSA (3x) showed almost zero conductivity and was consistent across different four point probe machines. The source of sample failure is unknown, but could be caused by damage during handling or degredation during storage. Reliable connection with the PEDOT:PSS layer on PDMS was difficult, giving only two measurements, so the datapoint (star) shown is the average of the two.

3.2.5. Cyclic voltammetry

The PEDOT:PSS film was electrochemically characterized using a three-electrode setup. The cyclic voltammetry diagram was obtained by sweeping a DC voltage from -0.4 V to +0.4 V at a speed of 0.1 V/s. The PEDOT:PSS film on PDMS is compared to the film on SiO_2 and on Au. From the CV curves, the charge storage capacity can be computed (CSC) by integrating the current passed during the cathodic phase (from +0.4 V to -0.4 V). The mathematical description is found in Appendix C. They are only computed for single-time spun coated samples. All PEDOT:PSS mixtures have EG added 5% v/v, so EG is omitted in the Table below.

Mixture	CSC SiO_2 [$\mu C mm^{-2}$]	CSC Au [$\mu C mm^{-2}$]	CSC PDMS [$\mu C mm^{-2}$]
PEDOT:PSS/GOPS+DBSA	0.5	0.5	0.25 (1500 rpm)
PEDOT:PSS/PEGDE+DBSA	1.0	1.1	-
PEDOT:PSS/PEGDE	1.5	1.0	-

These values are a factor 5-10 lower than [71]. The unit of CSC is charge per area, which might not be fully descriptive in the case of PEDOT:PSS due to its volumetric interaction. The difference between these results and [71] is presumably caused by a difference in PEDOT:PSS thickness, which does not

reflect on the CSC since it is taken by area. Ganji et al. [71] spin coated at 650 rpm, whereas it was spin coated at 2000 rpm here.

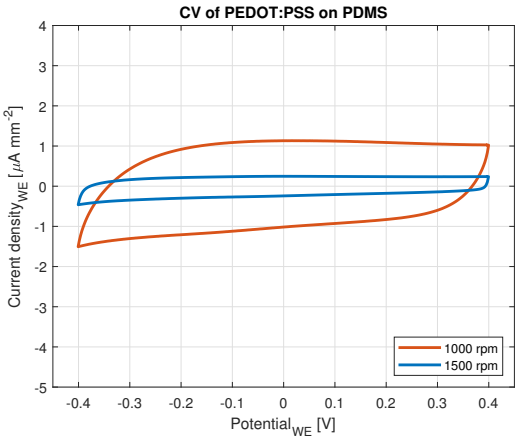

Figure 3.10: Cyclic voltammetry diagram of PEDOT:PSS, crosslinked with GOPS, on a PDMS substrate. The electrode size was 28 mm^2. The vertical axis shows current density. Comparing to Figure 3.11a and 3.12a, the CV-characteristics are similar though attenuated.

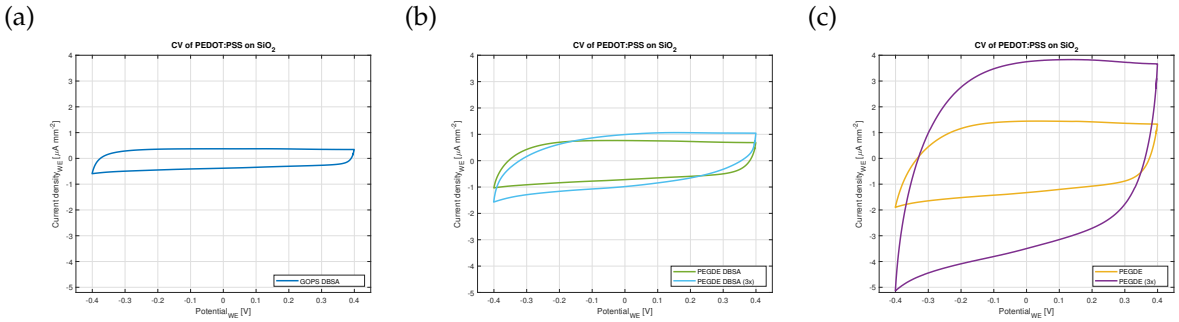

Figure 3.11: Cyclic voltammetry diagrams of PEDOT:PSS on SiO_2 mixed with **(a)** GOPS (1% v/v), DBSA (0.5% m/m), **(b)** PEGDE (1% v/v), DBSA (0.5% m/m), and **(c)** PEGDE (1% v/v). The electrode size was 28 mm^2. The vertical axis shows the current density. The fabrication of a 3x spin coated thin film of PEDOT:PSS with GOPS as cross-linker failed and is not shown.

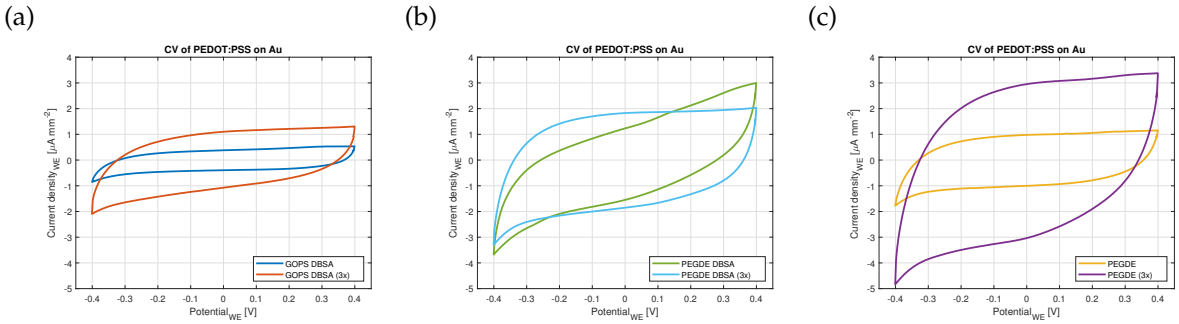

Figure 3.12: Cyclic voltammetry diagrams of PEDOT:PSS on Au substrates mixed with **(a)** GOPS (1% v/v), DBSA (0.5% m/m), **(b)** PEGDE (1% v/v), DBSA (0.5% m/m), and **(c)** PEGDE (1% v/v). The electrode size was 28 mm^2. The vertical axis shows the current density. Using GOPS as cross-linker decreases the current density compared to PEGDE, with or without DBSA as surfactant. PEGDE without DBSA results in a higher current density compared to PEGDE with DBSA for layer thickness of 300nm. For 100nm, PEGDE with DBSA showed more linear/resistive behaviour compared to PEGDE without DBSA, which showed the expected capacitive behaviour of PEDOT:PSS.

3.2.6. Electrochemical impedance spectra

The electrochemical impedance was obtained by applying a small sinusoidal signal (peak-to-peak 10 mV) to a three electrode setup. The EIS of the different PEDOT:PSS mixtures are compared for different substrates. For PDMS, only PEDOT:PSS/GOPS at two spin speeds was available, since the spin coating on PDMS was done at wafer scale; not all mixtures could be made for on wafer scale at this stage due to the higher material usage and implied costs.

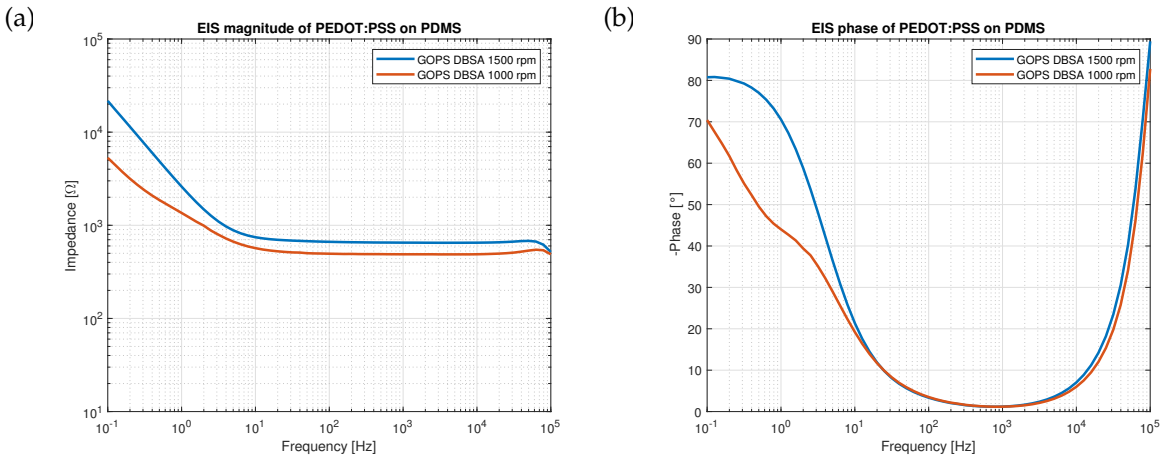

Figure 3.13: The EIS of PEDOT:PSS on PDMS with (a) the magnitude and (b) the phase response.

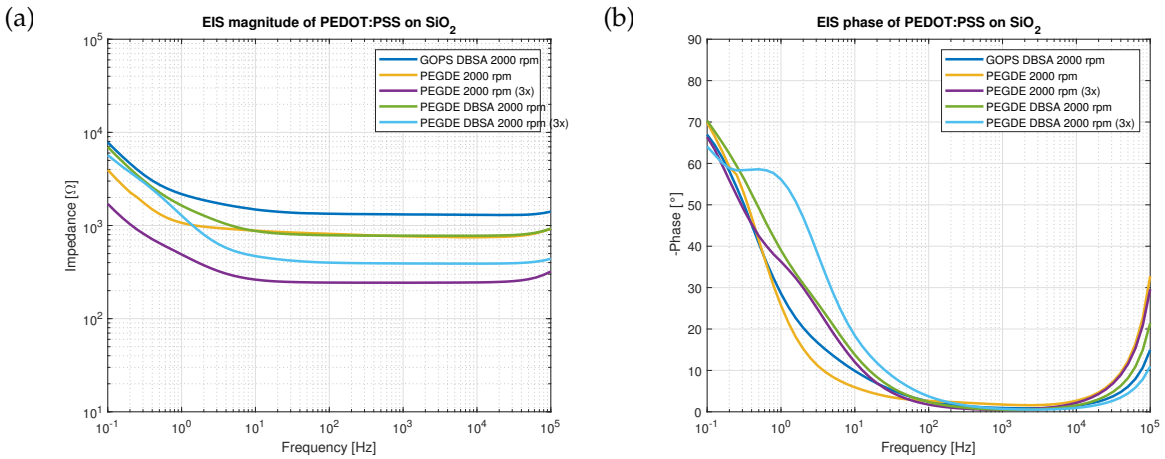

Figure 3.14: The EIS of PEDOT:PSS on SiO_2 with (a) the magnitude and (b) the phase response.

The EIS of PEDOT:PSS on all substrates shows a characteristic RC-behavior. An important difference between the samples on SiO_2,PDMS and Au is the corner frequency f_c and the resistance value. For SiO_2 and PDMS, the resistance value is around 1k Ω and for Au, it is around 50 Ω. An explanation is that current paths for the holes go through PEDOT:PSS for the non-conducting substrates SiO_2 and PDMS, while the hole current goes through Au for the Au substrates. Since the conductivity of Au is three orders of magnitude higher, it is expected that the resistance floor is significantly lower. Another interesting remark is that the response of the PEDOT:PSS/PEGDE+DBSA (3x) sample is comparable to the other responses, even though its conductivity was very low (see Figure 3.9a). It can be explained by that the conductivity measurements were performed after the electrochemical measurements, which may have affected the sample. Since it concerns only one sample, no significance can be claimed. An important conclusion from both electrochemical results is that PEDOT:PSS on PDMS has similar behavior to PEDOT:PSS on glass or substrates. The capacitance values can be extracted and compared to literature.

The samples on SiO_2 and Au can also be compared to one another in Figure 3.16. Since PEDOT:PSS/GOPS+DBSA is commonly used in literature, PEDOT:PSS/GOPS+DBSA is compared on

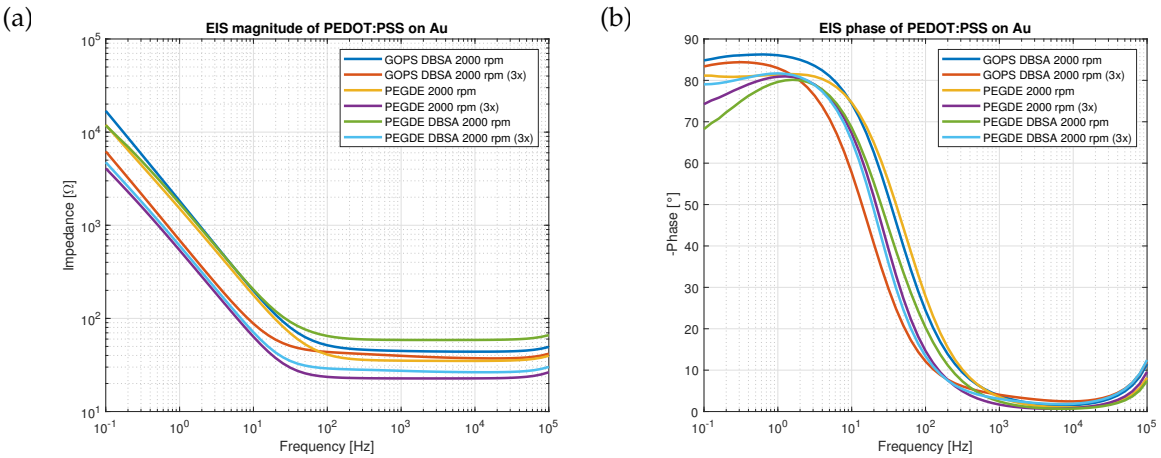

Figure 3.15: The EIS of PEDOT:PSS on Au with (a) the magnitude and (b) the phase response.

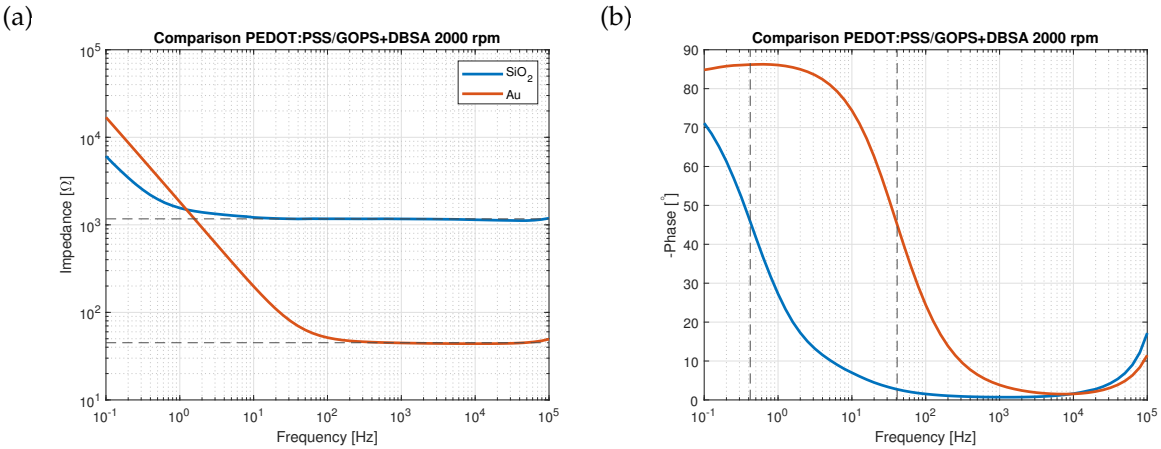

Figure 3.16: A comparison of the EIS with (a) the magnitude and (b) the phase response of PEDOT:PSS on Au and on SiO_2. The dotted black lines indicate the resistance R_{series} in (a) and the corner frequency in (b).

SiO_2 and Au. Both samples show the characteristic RC-behavior, which arises from a simplified circuit derived from the circuit in Figure 3.17. An important difference is the corner frequency f_c: for SiO_2, $f_c = 0.42Hz$ and for Au, $f_c = 41Hz$. The value R_{series} is extracted from the magnitude response: for SiO_2, $R_{series} = 1170\,\Omega$ and for Au, $R_{series} = 45\,\Omega$. The capacitance C_{WE} can be approximated by taking the impedance at 0.1Hz and dividing 1 by the impedance times the radial frequency. The thickness of the layers was also known, so the volumetric capacitance can be computed as well.

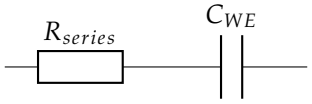

Figure 3.17: A simplified RC-circuit from Figure 2.2 to fit the observed behavior from PEDOT:PSS. R_{series} represents all the series resistances (source, electrode, and electrolyte) and C_{WE} is the capacitance of the working electrode. The parameters R and C can be extracted from the EIS and compared for the different substrates.

$$\text{SiO}_2 \quad C_{WE} = \frac{1}{|Z|2\pi f}|_{f=0.1Hz} = 265\mu F \quad C* = \frac{C_{WE}}{At} = 91.0\,C/cm^3 \tag{3.2}$$

$$\text{Au} \quad C_{WE} = \frac{1}{|Z|2\pi f}|_{f=0.1Hz} = 93.6\mu F \quad C* = \frac{C_{WE}}{At} = 30.4\,C/cm^3 \tag{3.3}$$

The volumetric capacitances $C*$ can be compared against the state-of-the-art ($39F/cm^3$). The capacitance

of PEDOT:PSS/GOPS+DBSA on SiO_2 is a factor 2.3 larger than the state-of-the-art and on Au it is a factor 0.78 lower. The disrepancy for SiO_2 is possibly caused by the approximation of C_{CE}: the phase has not settled yet at around 90° for SiO_2. However, even if it reached 90°, the slope would not increase beyond -20dB/dec and would therefore not catch up with the slope of PEDOT:PSS on Au. The disrepancy can therefore not be explained in full. Non-linear influences or processing differences may be a cause as well, though unlikely.

3.2.7. Adhesion strength

The PEDOT:PSS/GOPS+DBSA on PDMS wafer, spin coated at 500 rpm, was used for an adhesion strength measurement. Using the precision glass cutter, a matrix of 24 squares was cut. For example, in case two squares let go, the adhesion strength can be quantified as $\frac{22}{24}$ = 91.7%.

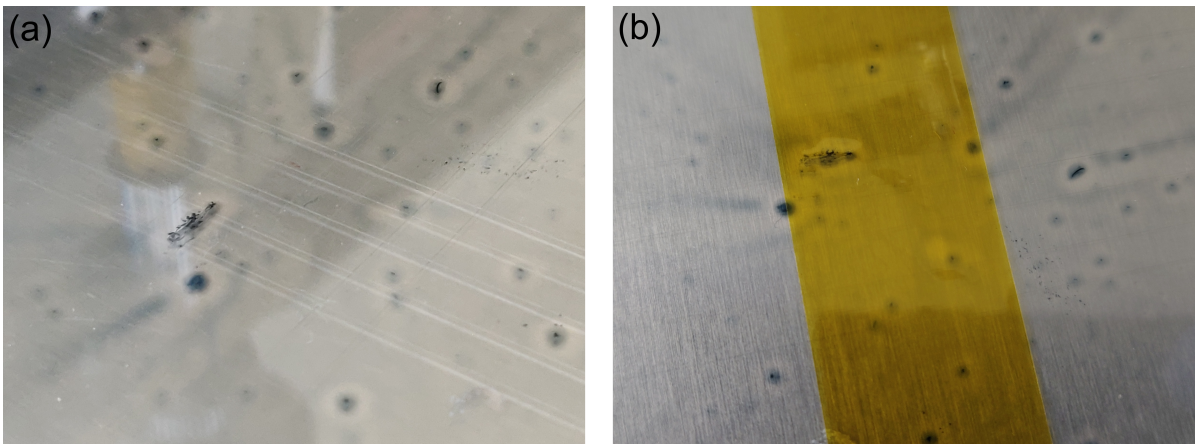

Figure 3.18: The Kapton adhesion strength test for PEDOT:PSS/GOPS+DBSA on PDMS using a 4x6 matrix with (a) the sample before the Kapton test and (b) directly after the Kapton test.

The Kapton test was performed and the sample was inspected. No squares from the matrix were pulled off and no damage was observed. The adhesion strength was therefore 100%, indicating a strong adhesion between PEDOT:PSS and PDMS. Another experiment was performed, where PEDOT:PSS/GOPS+DBSA and PEDOT:PSS/PEGDE+DBSA were spin coated on a SiO_2 die of 2 cm x 2 cm first and then PDMS was spin coated on top. It was done to test the adhesion between PEDOT:PSS/PEGDE+DBSA and PDMS and compare it to PEDOT:PSS/GOPS+DBSA, as it was hypothesized that the epoxide groups of PEGDE could not bond well with PDMS. As can be seen in Figure 3.19, PEDOT:PSS/PEGDE+DBSA has poor adhesion to PDMS and comes off after being immersed in DI water for 5 minutes.

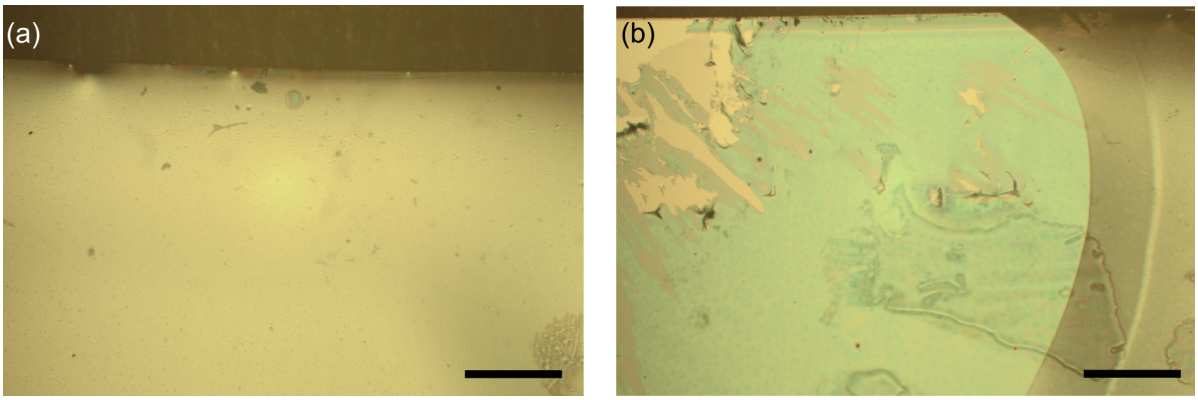

Figure 3.19: The samples of PEDOT:PSS mixtures with PDMS on top after immersion in DI water for 5 minutes. PEDOT:PSS is mixed with (a) EG, GOPS, DBSA, and (b) EG, PEGDE, DBSA. (a) did not show any signs of delamination, not even at the edges, while (b) delaminated in a few minutes and could be pulled further off by tweezers. The black scale bar is 2 mm.

3.3. Reliability & failure mechanisms

An important failure in microelectrode array devices is delamination [38]. To gain insight into the long term reliability of the PEDOT:PSS/GOPS and PDMS layer interface, a small accelerated aging test was conducted: three materials, being PEDOT:PSS/GOPS (spincoated), Au (evaporated), and PDMS (spincoated), were stacked in different configurations, as shown in Figure 3.20.

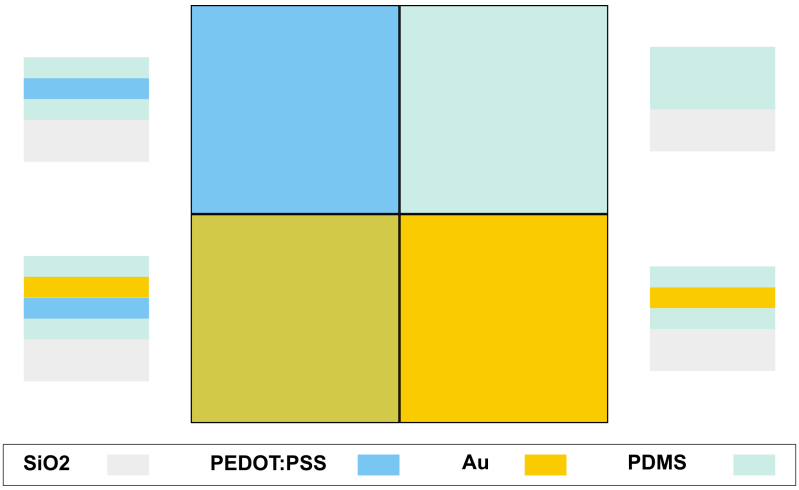

Figure 3.20: The layer stacking configurations for the accelerated aging test. PDMS encapsulates either PEDOT:PSS/GOPS, Au, or PEDOT:PSS/GOPS with Au on top.

A wafer was first coated with PDMS, Sylgard 184 (ratio 10:1), at 2000 rpm and cured at 90°C for one hour. Then PEDOT:PSS (Hereaus Clevios PH1000) was mixed with ethylene glycol (EG) at 5% v/v and 4-dodecylbenzenesulphonic acid (DBSA) at 0.5% m/m. The mixture was mixed and degassed in a Thinky ARE-250. Then (3-glycidyloxypropyl)trimethoxysilane (GOPS) was added as crosslinker (1% v/v) and the mixture was mixed and degassed again using the ARE-250. The degassing was necessary to get rid off bubble formation due to DBSA. The PEDOT:PSS mixture was then spin coated on the PDMS layer at 2000 rpm. Three stripes were manually made by removing PEDOT:PSS with a swab and DI water. The wafer was then baked at 110°C for one hour. Kapton tape was added to form three stripes (orthogonal to the PEDOT:PSS removed stripes) to form a grid. 10 nm Ti and 100 nm Au was evaporated with an e-beam evaporator (CHA std. solutions). After evaporation, the Kapton tape was removed and a roughly patterned grid of PEDOT:PSS, PDMS and Au is made. Another layer of PDMS was spincoated on top at 3000 rpm. The wafer was cut into smaller rectangular pieces. The long side was 2 cm long side, short side was variable and dependent on the patterned grid. The pieces each contained a square as depicted in Figure 3.20.

The aim of the experiment is to gain insight into the adhesion strength and possible delamination of PEDOT:PSS/GOPS compared to Au on PDMS. The pieces with layer stacks were placed in phosphate-buffered saline (PBS) at 60°C and sonicated lightly ('degas' mode on Fisherbrand Select 30) to add energy to the system and act as accelerated aging factor. Two pieces were taken out every 15 minutes till 105 minutes had passed. The results do not show a quantitative answer, but provide insight in comparing delamination of PEDOT:PSS and Au. A shortcoming of the experiment is that the layer stacks were exposed on the sides to PBS, which does not correctly represent a fully encapsulated device. The results are still insightful however and indicate that PEDOT:PSS/GOPS has a strong adhesion, not showing any indication of delamination, compared to gradual detoriation of the Au/PDMS or Au/PEDOT:PSS interface. The explanation for strong adhesion between PEDOT:PSS/GOPS and PDMS is that GOPS, which is a silane, can bond strongly to the silicon bonds in PDMS. Au does not however, and even using Ti as adhesion layer does not avoid rapid delamination in this experiment.

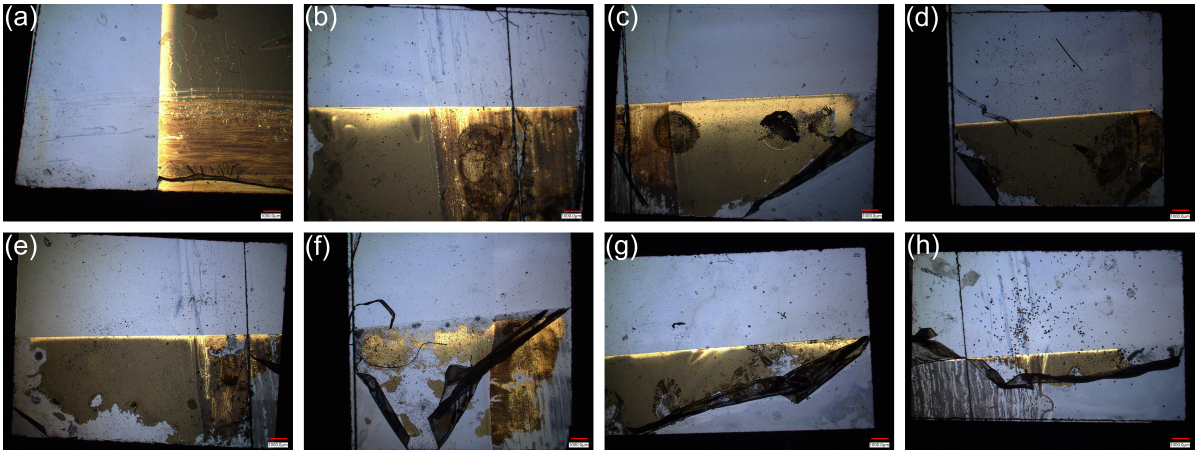

Figure 3.21: The results of the accelerated aging experiment. Every 15 minutes, samples were taken out and visually compared with (a) after 15 minutes, (b) after 30 minutes, (c) after 45 minutes, (d) after 60 minutes, (e) after 75 minutes, (f) after 90 minutes, (g and h) after 105 minutes.

3.4. Summary

In this chapter, the spin coated material layers of PEDOT:PSS and PDMS were characterized. Important properties for the microfabrication process were investigated, including thickness and uniformity, conductivity, cylic voltammetry and electrochemical impedance spectra. It was found that PEDOT:PSS had a conductivity around 200 S/cm with GOPS as crosslinker and 300 S/cm for PEGDE. The electrochemical behavior of PEDOT:PSS/GOPS+DBSA on PDMS was similar to PEDOT:PSS on SiO_2 and Au. Using GOPS as crosslinker caused a strong adhesion between PDMS and PEDOT:PSS, whereas using PEGDE as crosslinker resulted in poor adhesion between PDMS and PEDOT:PSS. For long-term reliable microelectrode arrays employing PEDOT:PSS and PDMS, GOPS is preferred over PEGDE due to its stronger adhesion at the cost of lower conductivity. With the materials characterized, the next step into microelectrode array design can be taken.

4

Device design

4.1. Design overview

Before diving into the details of the microelectrode array design, an overview is given. Subsequently, the three main parts of the microelectrode array, i.e. the electrodes, the tracks, and the back-end connection, are discussed. In Figure 4.1, the full design is shown. It consists of back-end connection pads of Au, Au tracks that transition into PEDOT:PSS tracks and finally the PEDOT:PSS electrodes. The dimensions of the connection pads were determined by the back-end connector and is discussed in section 4.4. Six of these devices fit on one 4-inch wafer. The pattern for the full wafer can be found in Appendix D.1.

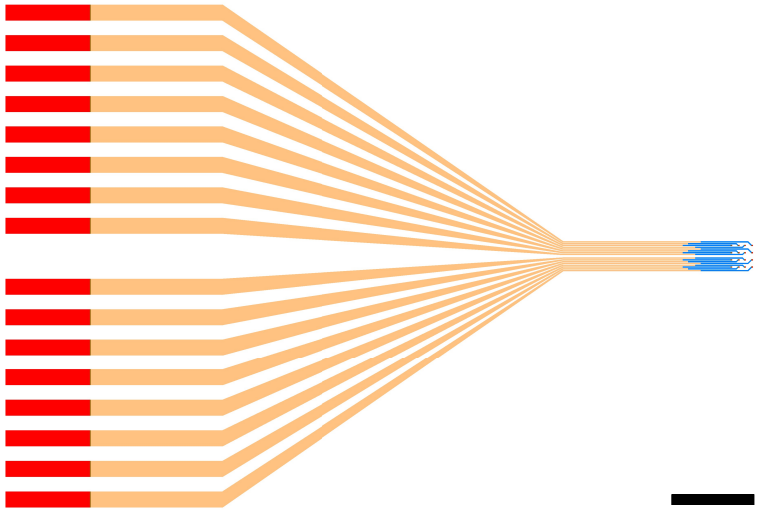

Figure 4.1: The design of the a single full device. The red pads are according to the dimensions of the Omnetics connector. The metal track lengths vary but are negligible in their contribution to the total electrode impedance. The gold connection pads (red) lie on SiO_2 and then connect to the gold layer on PDMS (orange). The gold tracks transition into PEDOT:PSS tracks (blue) on PDMS and go through the PDMS layer to form electrode sites (red). The scale bar is 10 mm.

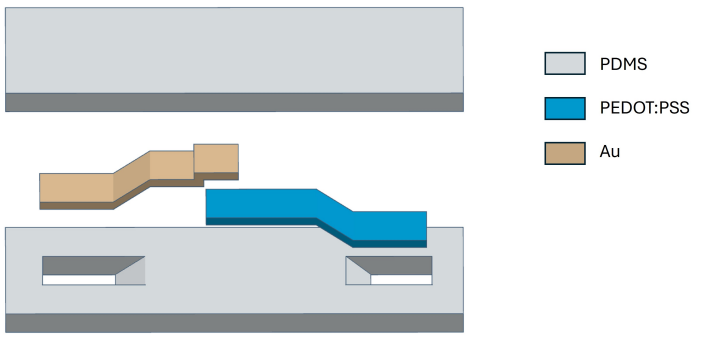

Figure 4.2: A 3D model of the proposed device design, showing that a thin film connection is made twice through the PDMS for Au and for PEDOT:PSS. The dimensions are not to scale.

4.2. Electrodes

A standard in literature for electrode dimensions is 30 μm since it matches the dimensions of a neuron soma closely. The 30 μm size is taken as a starting point for the electrode design. A challenge in using PDMS as insulation layer is its thickness: the most common microfabrication technique for PDMS, spin coating, reaches an asymptote of 8 μm. Comparing to thin PEDOT:PSS films of several hundreds of nanometers thick, a problem arises. The thin films will most probably break or lose connection over a drop of 8 μm. Two approaches can solve this problem: the first is to accept that the drop is not possible and pattern PEDOT:PSS as two-dimensional layer on PDMS. Filho et al. [31] chose this approach and patterned PEDOT:PSS ink manually. Insulation from channels was done by applying PDMS (400 μm thick) layer on top of the channels. A critique of this approach is that the electrodes are placed distantly from the target tissue, since a thick passivation layer lies on top. This could cause loss of signal and dimensional control is difficult as well.

Another approach is to create a via connecting layers on both sides of the PDMS passivation layer. Guo et al. [104] demonstrated such an approach by creating a via for gold using negative photoresist. The via is created by patterning a large overhanging photoresist structure, thereby an inverse slope. When PDMS is subsequently applied and spin coated, it forms around the overhanging photoresist structures. Upon removal of the photoresist, a slope remains in the PDMS layer over which other, thinner layers can be patterned.

In continued work, Guo et al. [103] claim to use the effect of aperture diffraction to achieve the overhanging structure. However, inspecting the Frauenhofer condition in their microfabrication process casts some doubt upon the origin of the Gaussian-like intensity profile. The Frauenhofer condition is defined as

$$R >> \frac{a^2}{\lambda} \tag{4.1}$$

with R the shortest distance between an aperture point and the point of observation, a the largest dimension of the aperture hole, and λ the wavelength. In the case of Guo et al. [103], [104], $R \approx 1$mm, $a = 100\mu$m, and $\lambda = 365$ nm. Computing the equation yields

$$R = 1 \cdot 10^{-3} >> \frac{a^2}{\lambda} = \frac{(100 \cdot 10^{-6})^2}{365 \cdot 10^{-9}} = 27.4 \cdot 10^{-3} \tag{4.2}$$

The inequality and so the Frauenhofer condition is not met. Attributing the intensity profile to aperture diffraction is therefore unlikely. However, an assumption in the Frauenhofer condition is that the incident light is a planar wave. In case of not entirely uniform waves, the intensity profile may be earlier observed than the Frauenhofer condition is satisfied.

The approach offered by Guo et al. to pattern PDMS using overhanging photoresist structures is promising. However, due to the uncertainty of the working principle and the low directionality, using aperture holes to pattern the PDMS is not selected. Grey-scale lithography is a relatively new technique in which a 3D profile can be patterned in photoresist. It requires a single-point exposure technique to control lithography accurately, such as in a laser writer. Alternating the intensity profile of the laser while patterning allows for various depths of crosslinking in the resist. During development, the profile becomes apparent and can be used for further processes. The process is illustrated in Figure 4.3.

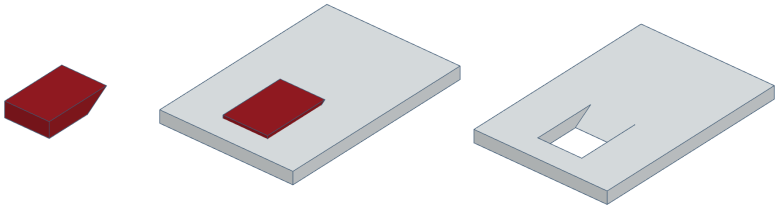

Figure 4.3: The PDMS patterning technique as envisioned using grey scale lithography. First, negative photoresist is patterned with an overhanging structure. Then PDMS is spin coated and flows around the photoresist structure. After curing the PDMS, the photoresist structure is removed and patterned PDMS remains.

Grey-scale lithography is performed using a Heidelberg MLA 150 laser writer. The input file is in `.dxf` format. The file contains a schematic with layers corresponding to one intensity level, shown in Figure 4.4. The intensity levels are specified in the software of the MLA150 through linear interpolation of the maximal dose, indicated by a value between 0 (no dose) and 255 (maximal dose). The photoresist selected for this application is AZNLOF2070 (MicroChemicals GmbH) since it can reach layers thicker than 10 μm. The minimal crosslinking intensity and the absorption coefficient are important to determine the intensity profile. For AZNLOF2070, the minimal crosslinking intensity I_{min} is 15 mJ/cm^2 and the absorption coefficient α is 0.3-0.4 μm^{-1} [98]. The Beer-Lambert law relates intensity to the depth light traveled into a material. Rewriting it to compute the required minimal dose to crosslink AZNLOF2070 at the desired depth profile gives

$$I_0 = I_{min} e^{\alpha d} \tag{4.3}$$

where I_0 is the required starting intensity for the laser writer and d the depth at which the intensity should reach 15 mJ/cm^2. Computing the profile along the horizontal plane gives Figure 4.4b.

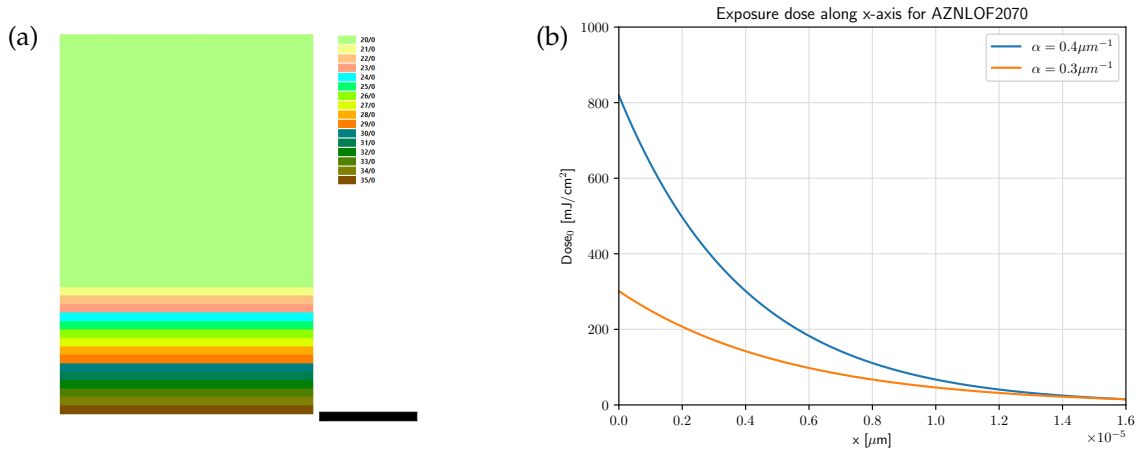

Figure 4.4: The technique to pattern an overhanging photoresist structure using grey-scale lithography, with (a) the electrode with overhang pattern in KLayout Editor and (b) the dose profile to create a linear overhang at 45°. $x = 0$ corresponds to the start of the rainbow pattern (layer 20) in (a) and $x = 16 \cdot 10^{-6}$ to the end of the rainbow pattern (layer 35).

Quantizing the values of the curve in Figure 4.4b to the layers in Figure 4.4a gives the values between 0 and 255 from Table 4.1. These values are relative and needed for the grey-scale lithography.

layer	20	21	22	23	24	25	26	27	28	29	30	31	32	33	34	35
value	255	199	154	120	94	73	57	44	35	27	21	16	13	10	8	6

Table 4.1: Grey scale values between 0 and 255 corresponding to the desired intensity percentage for each layer.

4.3. Tracks

The conductivity of PEDOT:PSS was found to be 200 S/cm and the conductivity of Au is known to be $452 \cdot 10^3$ S/cm. The conductivities differ three orders of magnitude! Implementing a track of 1 mm length, 30 μm width and 200 nm for PEDOT:PSS and 100 nm for Au results in:

$$R_{Pp} = \frac{\rho l}{wt} = \frac{\frac{1}{2.0 \cdot 10^4 S/m}(1 \cdot 10^{-3} m)}{(30 \cdot 10^{-6} m)(200 \cdot 10^{-9} m)} = 8.3 \cdot 10^3\,\Omega \tag{4.4}$$

$$R_{Au} = \frac{\rho l}{wt} = \frac{(22.14 \cdot 10^{-9} \Omega m)(1 \cdot 10^{-3} m)}{(30 \cdot 10^{-6} m)(300 \cdot 10^{-9} m)} = 2.5\,\Omega \tag{4.5}$$

where R_{Pp} is the resistance of the PEDOT:PSS track, ρ_{Pp} the resistivity of PEDOT:PSS, R_{Au} is the resistance of the Au track, ρ_{Au} the resistivity of Au, l the length of the track, w the width of the track, and t the thickness. As expected, the resistances mirror the three order magnitude difference in resistivity. Hence, the part of the tracks that is only PEDOT:PSS is chosen to be no longer than 1 mm to balance the track resistance and the area in which microelectrode array is transparent. An exploded view of the final proposed layer structure for an PEDOT:PSS electrode on PDMS substrate is shown in Figure 4.6.

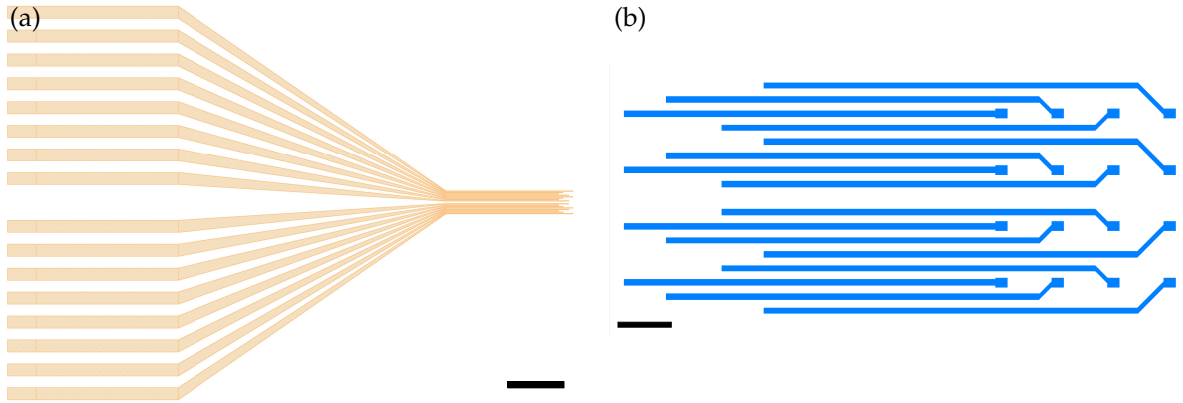

Figure 4.5: The design of the sixteen electrodes and the tracks leading away from them. (a) The metal tracks leading to the microelectrode array, designed to connect to a back-end connector which will be soldered to it. The black scale bar is 3mm. (b) PEDOT:PSS tracks with a length of 1 mm to provide a transparent window for imaging. The black scale bar is 200 μm. A 1 mm overlap between PEDOT:PSS and the metal is chosen to provide a stable interface between the two materials.

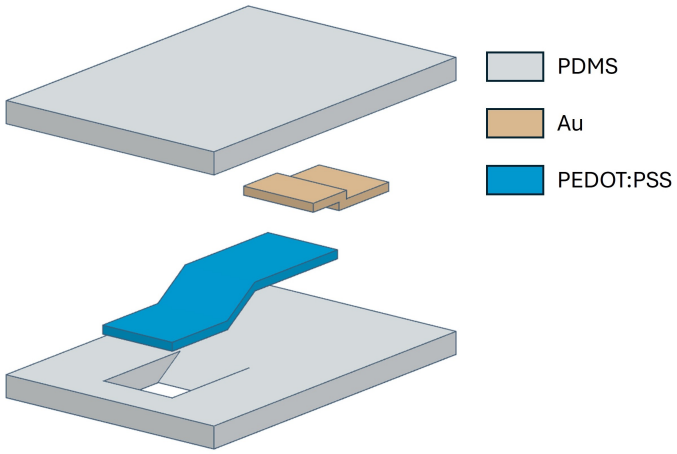

Figure 4.6: An exploded view of the PEDOT:PSS electrode on PDMS substrate with tracks of partly PEDOT:PSS and partly Au. The dimensions are illustrative and not representative of the design.

4.4. Back-end connection

The function of a microelectrode array is to translate electrochemical signals into the electronic domain. For further processing, the signal from the microelectrode array should be connected with the back-end. The connection also should be adaptable since the device can preferably be connected to different machines, such as potentiostats or signal generators. Furthermore, the connection has to be reliable. Summing these reasons led to choosing an Omnetics 16-pin connector (OMNETICS A24001-016) with cable leads as endings. The connector will be soldered to connection pads of the device. There were concerns about soldering onto metal pads on PDMS, since there is a soft layer under the metal that can cause failure if the metal pads break. The greyscale lithography will therefore be performed also for the connection pads, so that the metal is bonded directly onto the substrate glass. It will be further discussed in the next chapter.

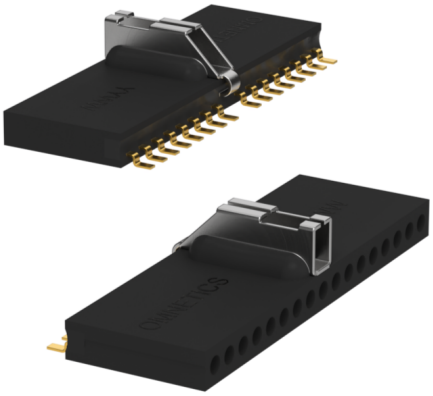

Figure 4.7: The selected connector from Omnetics to connect the flexible microelectrode array device to other instruments.

Additionally, test structures including electrical line measurement (ELM) of PEDOT:PSS and Au and Van der Pauw structures for PEDOT:PSS were included to characterize material resistivity.

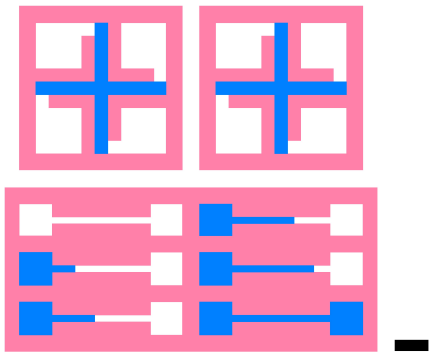

Figure 4.8: The test structures incorporated in the wafer design. Included are: Van der Pauw structures to measure the sheet conductivity and electrical line measurement (ELM) structures to gain insight in the hypothesized trade-offs between PEDOT:PSS and Au for track resistances. The pink part is to expose negative photoresist and perform a metal lift-off. The blue part is to expose negative photoresist to etch PEDOT:PSS. These processes are discussed in more detail in the next chapter about fabrication.

5
Device Fabrication

5.1. Microfabrication process flow

The corresponding cleanroom flowchart can be found at the end of this document after the appendices. The materials used are silicon (P-type, 100), LOR5b [112] and ECL3007 [113] for bilayer photoresist, hexamethyldisilane (HMDS) for improving photoresist adhesion, NLOF2070 for grey-scale lithography [98], H,1H,2H,2H-perfluorooctyl-trichlorosilane (PFOTCS) for an anti-adhesive layer, PDMS (Sylgard 184, Dow Corning), PEDOT:PSS (Hereaus Clevios PH-1000) mixed with ethylene glycol (EG), dodecylbenzene sulfonic acid (DBSA), and (3-glycidyloxypropyl)trimethoxysilane (GOPS) purchased from Sigma Aldrich. The process steps are shown in Figure 5.1.

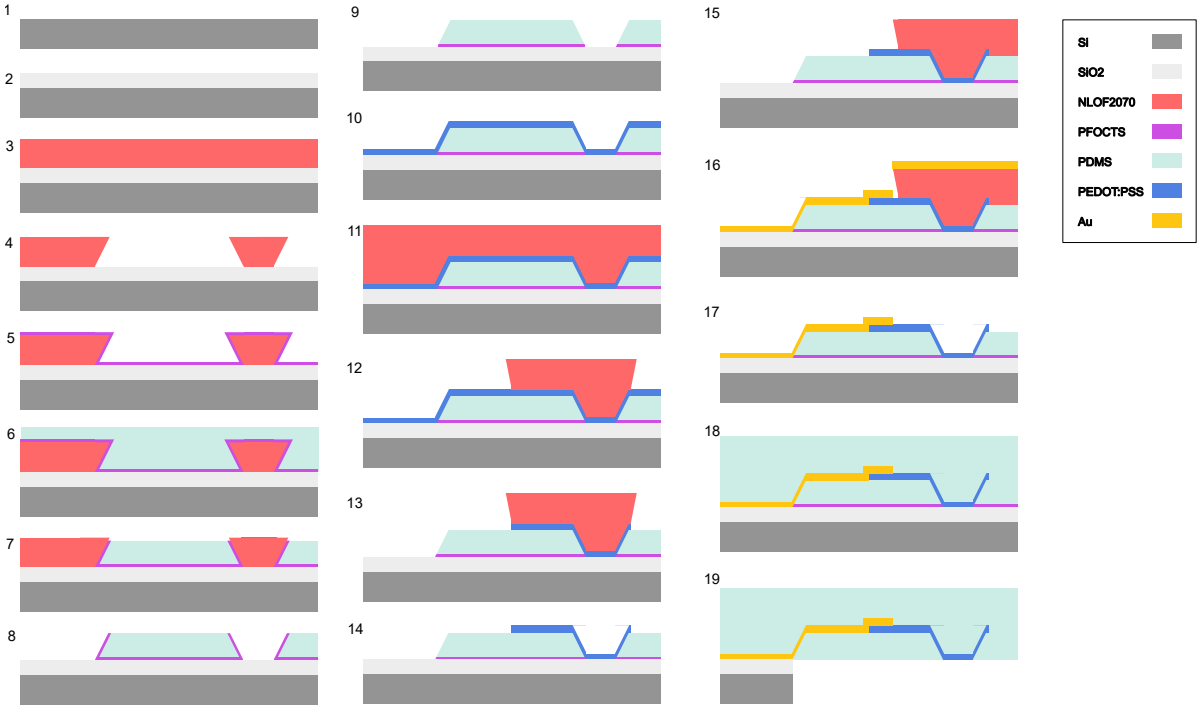

Figure 5.1: The microfabrication process flow, illustrated. It starts with (**1**) a 4-inch silicon wafer, on which (**2**) a SiO_2 layer is thermally grown. Patterning the zero layer is not shown here, but is done through bilayer photoresist and an Al lift-off process. Grey scale lithography (**3-4**) is used to pattern large overhang photoresist structures, after which (**5**) PFOTCS is isotropically deposited. (**6**) PDMS is spin coated and patterned using these resist structures. Due to issues with the spin coater, PDMS could not be spin coated thinner than the photoresist. Therefore, (**7**) PDMS is etched with SF_6, after which (**8**) the photoresist structure is stripped. (**9**) O_2 plasma removes exposed PFOTCS and makes the PDMS surface hydrophilic before (**10**) spin coating PEDOT:PSS. (**11-12**) A lithography step is needed to (**13**) O_2 RIE etch PEDOT:PSS. (**14-17**) The photoresist is stripped and another lithography step is performed for gold lift-off. After lift-off, (**18**) PDMS is spin coated on top and (**19**) the device is (partly) peeled off and part of the substrate is removed by cutting it.

5.2. Thermal oxidation

The first step is to thermally grow an oxide layer on top of the silicon wafer. A 4-inch silicon wafer was chosen as substrate because it reflects light, making visual inspection of thin films easier. Dry oxidation was selected due to its higher quality of oxide and availability of machinery, though both wet and dry oxidation should suffice as substrate SiO_2. A Woollam ellipsometer yielded 219 nm thick SiO_2 layers.

5.3. Zero layer

On five silicon 4-inch wafers were SiO_2 layers thermally grown in the Else Kooi cleanroom. They were taken to the Kavli Nanolab cleanroom, where the lithography steps were taken. Two types of alignment markers were patterned: a custom alignment cross that can be used by the MLA 150, and an extensive alignment marker provided by the Else Kooi staff that can be used by a MA6 mask aligner. The extensive alignment marker is shown in Figure 5.2a. The markers will be fabricated by a Al lift-off process. For a lift-off process, a photoresist pattern with undercut is necessary to fabricate high-resolution metal patterns. Usually, two photoresist types can be used: negative photoresist, which during (over)development shows an undercut, or a bilayer photoresist, where a positive photoresist is applied on top of a rapidly dissolving layer to create an undercut under positive photoresist. Negative photoresist should expose everywhere except on the patterned structures, since the photoresist will be removed where negative photoresist is not exposed. For small patterns, this implies exposing a whole wafer, which takes significant time. Therefore, bilayer photoresist was selected for patterning the zero layer. LOR5b was used a rapidly dissolving layer and ECL3007 was used as positive photoresist. A μMLA (Heidelberg) was used for exposing the patterns. A detailed recipe can be found in Appendix E.1.

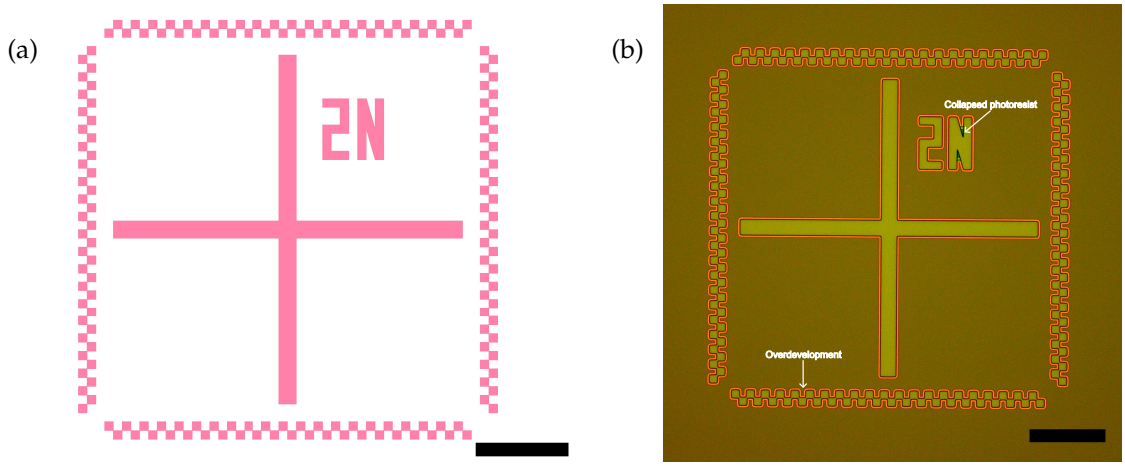

Figure 5.2: The (a) designed alignment marker where the scale bar is 100 μm and (b) the result after exposing and developing the bilayer photoresist where the scale bar is 100 μm. Using bilayer photoresist enables positive photoresist-like exposure, which speeds up the exposure significantly for the alignment markers. Some parts of the resist have collapsed and rounded features indicate minor overdevelopment.

After the bilayer photoresist is applied and patterned, 10 nm Ti and 100 nm Al can be evaporated onto the substrate using a CHA solutions e-beam evaporator. The result is shown Figure 5.3.

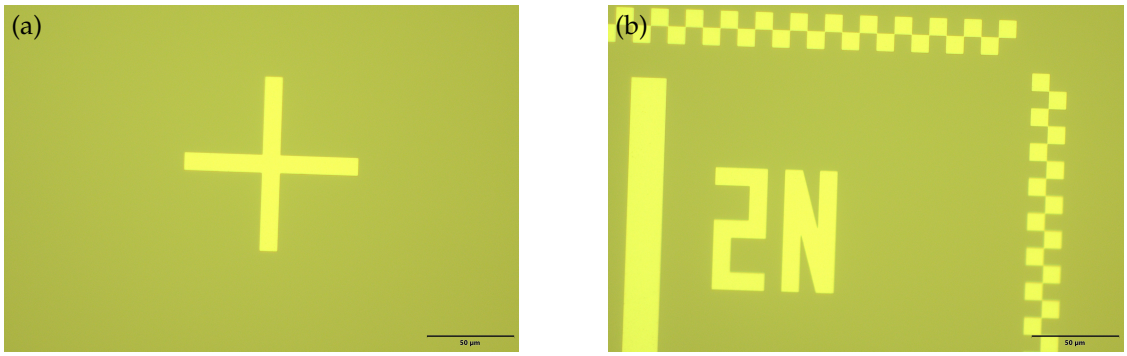

Figure 5.3: The two types of Al alignment markers after lift-off, with (a) a custom cross alignment marker and (b) the EKL alignment marker. The patterns look sharp, indicating a successful lift-off.

5.4. Grey-scale lithography

The next step, grey-scale lithography, introduces a novel fabrication technique to pattern sub 100 μm diameter electrodes on PDMS. Grey scale lithography is a technique that exposes photoresist with different doses at different locations and can therefore create height profiles in photoresist. This is also called 2.5-dimensional lithography. The grey-scale exposure is performed with a laser writer (MLA 150, Heidelberg) and were not performed before at the TU Delft. The process itself encountered significant troubleshooting due to grey-scale exposure not being optimized or explored before. Within the time constraint of this project, not all issues could be resolved and will be discussed in the discussion.

The starting point for grey-scale lithography was a dose test, followed by scanning electron microscopy (SEM) imaging of the resist. Small silicon dies (2cm x 2cm) were cleaned with HNO_3 and treated with HMDS. AZNLOF2070 was spin coated and a scratch test with a profilometer (Bruker Dektak XT) was performed. The thickness at 2000 rpm was 10.2 μm. Next, the photoresist was exposed with the MLA 150. Here, the first issues started appearing. First, the grey-scale exposure option was hidden away and could only be activated by loading designs with the format `.DXF - Greyscale`. The tool owner was not aware of it, since the company had not demonstrated the machine's capability of grey-scale exposure. Having resolved it, the next issue appeared: dose test exposure took more than five hours. It restricted dose tests to overnight exposures. At this time, the grey-scale table with values from 0 to 255 was not correctly understood, leading to linear input values between 0 and 255. This does not account for the Beer-Lambert law and exponential decay of exposure dose, and should therefore give non-linear sloped overhanging structures. Two attempts are shown in Figure 5.4a and 5.4b. In Figure 5.4a, the bottom corners can be seen to curl up, indicating the photoresist not adhering well to silicon. Consequently, development could not be completed. It was later found that an issue with the HMDS machine caused the poor adhesion. A second attempt is shown in Figure 5.4b with longer development time and good adhesion. An overhang can be seen on the right side, but is not clearly defined. Undercut of the photoresist can also be seen, which is characteristic for negative photoresist. However, not fully crosslinked photoresist causes the undercut and with it, a loss of dimensional control. The absorption coefficient was also not fixed, but ranged between 0.3 and 0.4 μm^{-1}. A higher dose, corresponding to 0.4 μm−1, was tried and its result is shown in Figure 5.4c. Here, the photoresist is fully crosslinked and a defined slope can be observed, though the dose may have been too high since the slope is too steep. The grey-scale exposure should ideally be optimized before continuing. However, due to time constraints and the long exposure duration of dose tests, the grey-scale lithography is not further optimized. A final dose of 700 mJ/cm^2 was selected, but no SEM images were take of this exposure.

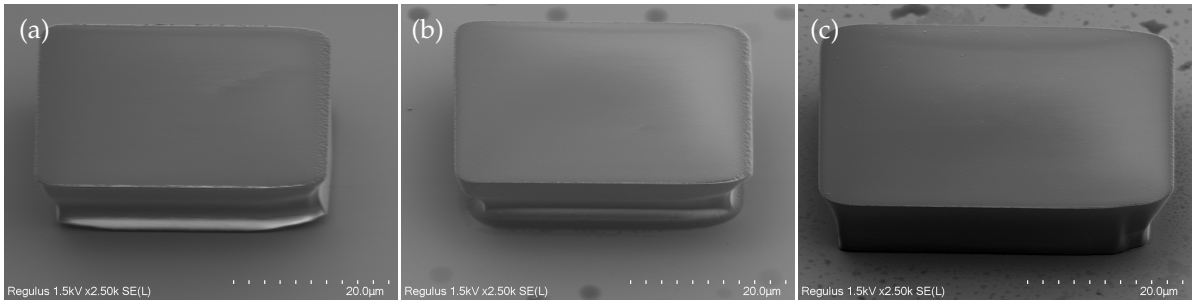

Figure 5.4: Three imaged photoresist pillars where (a) the exposure time is 11 minutes and 20 seconds, dose is 230 mJ/cm^2, and the defocus is -25, (b) the exposure time is 13 minutes and 45 seconds, dose is 230 mJ/cm^2, and the defocus is -25, (c) the exposure time is 14 minutes, dose is 800 mJ/cm^2, and the defocus is -21. (a-b) show not fully crosslinked photoresists with an undercut, where (c) shows fully crosslinked photoresist.

Another issue was encountered during device fabrication and was not resolved during the project. The issue was that full-wafer exposure would not start without an error being raised and the system freezing for 10 minutes. A similar issue is reported by [114], but the workaround proposed did not resolve the issue. The issue did not appear when exposing only one microelectrode pattern without pads. Therefore, the microelectrode arrays were exposed one by one and the pads discarded. The full recipe for the photoresist patterning is given in Appendix E.2. The patterned pillars for the device were imaged with a microscope (Olympus) and are shown in Figure 5.5.

In the 100x magnified images, a slight undercut can be observed in both the bright field and dark field

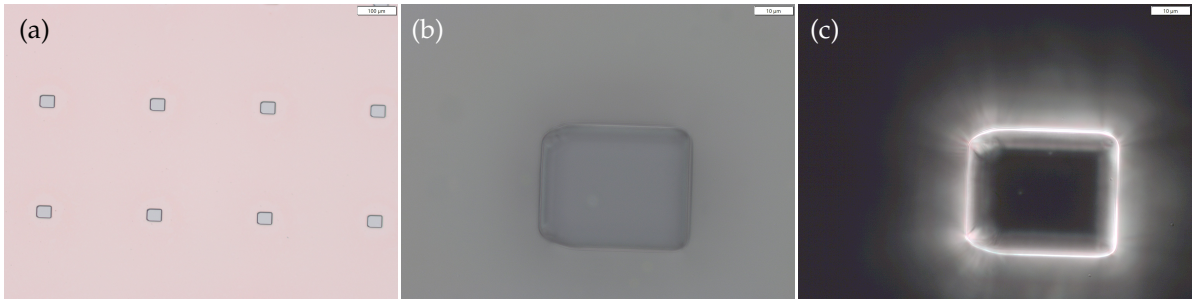

Figure 5.5: The final photoresist structures imaged by a microscope with (a) two rows of a microelectrode array at 10x magnification, (b) a bright field image of one pillar for electrode patterning, (c) a dark field image of one pillar for electrode patterning.

images. The dark field image in Figure 5.5c shows a transitioning pattern, indicating an overhang. For such thick resist, microscope imaging is hard since the focal plane cannot focus on the bottom and top at the same time. Confocal microscopy might solve this issue, but has not been tried and might lack spatial resolution.

5.5. PDMS bottom layer

Having patterned the photoresist pillars, the next step is to coat the wafer with H,1H,2H,2H-perfluorooctyl- trichlorosilane (PFOTCS) as anti-adhesive layer for PDMS. This is done by putting a wafer together with three drops of PFOTCS into a vacuum chamber. The chamber is left at vacuum overnight and the wafer is taken out the next morning and inspected. Then, PDMS (Sylgard 184) is prepared in a 10:1 ratio. The mixture is mixed and degassed using a Thinky ARE-250 at 2000 rpm for 2 minutes. The PDMS was applied on the sample and spin coated at 3000 rpm, since that was the highest safe rotational speed for the spin coater at the time. The process was first attempted with two die-scale samples from the dose tests and the results after spin coating are shown in Figure 5.6.

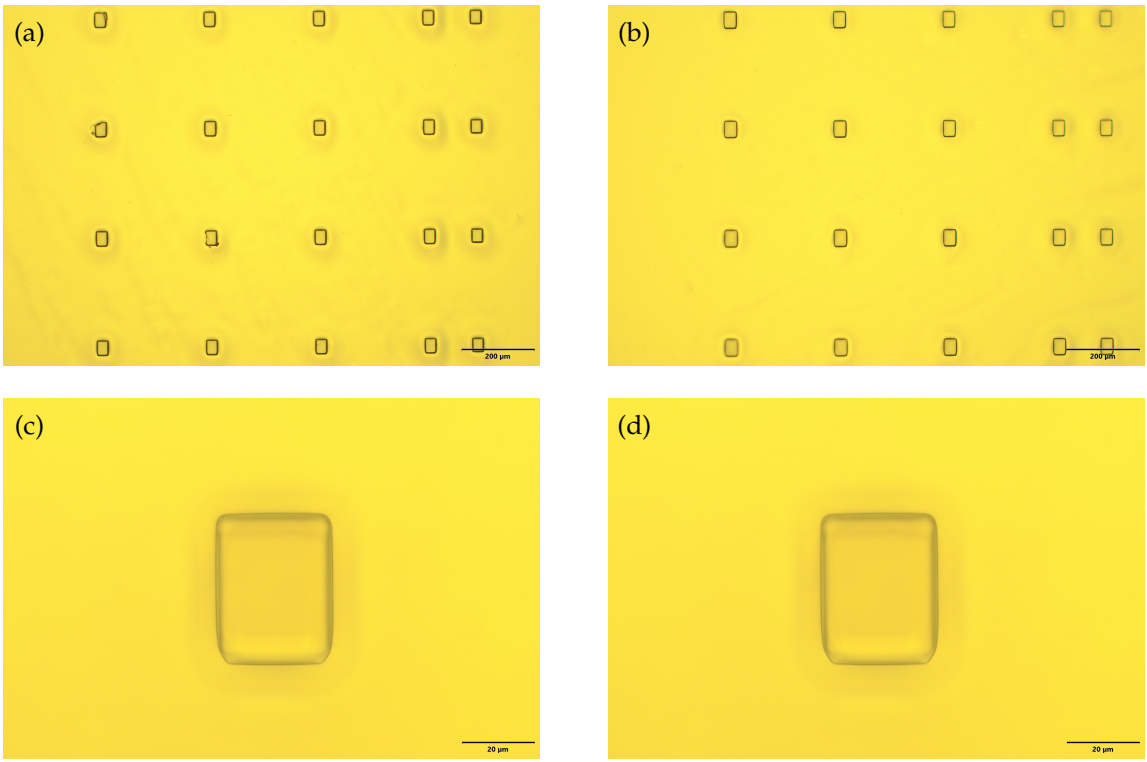

Figure 5.6: The photoresist pillars after spin coating PDMS with (a,c) 300 mJ/cm^2 and (b,d) 800 mJ/cm^2. Small circles around the pillars can be seen, indicating non-uniformities. It was therefore chosen to let the PDMS sit for 2 minutes before starting spin coating.

After the test with die-scale samples, the wafers were spin coated with PDMS as well at 3000 rpm. Based on the results of the die-scale, the PDMS was applied and allowed to spread for 2 minutes. From the spin curve from Figure 3.8b, 3000 rpm results in 15 μm. The pillars are $\approx 10\mu m$, meaning that PDMS covers them fully. To create a thinner PDMS layer, a SF_6 RIE etching step was performed. The etch rate was determined to be 1 μm/min and performed with an AMS110. The etch recipe contained low contents of O_2, so there were concerns that the photoresist would be etched rapidly upon contact with the plasma. However, the O_2 content was too low to etch the photoresist significantly. The profile of the PDMS and a photoresist pillar are shown in Figures 5.7.

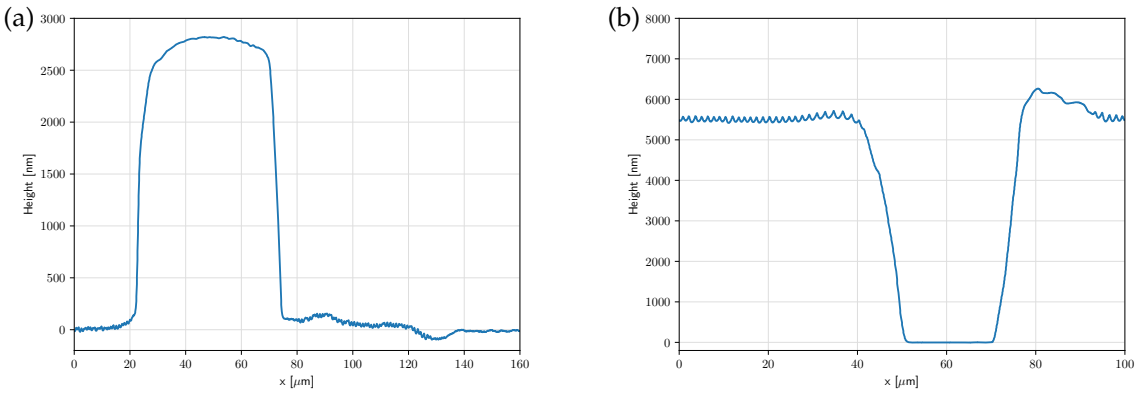

Figure 5.7: The profiles after PDMS spin coating measured with a profilometer with (a) the profile after SF_6 RIE and (b) after NI555 photoresist removal.

After the RIE step, the photoresist pillars should be removed. NI555 is a photoresist stripper and was used to remove the pillars. A first attempt was to leave the die-scale sample in NI555 at 60°C overnight. Inspection with a profilometer determined that the pillars were not removed. A possible explanation is that the RIE step altered the exposed photoresist and made it hard to remove [115]. To achieve removal, the samples were placed in NI555 again and sonicated at low power. This removed the pillars successfully on the die-scale samples. Afterwards, the removal was tried for the wafer-scale samples for 10 minutes and inspected for potential PDMS lifting off, since sonication could disturb the adhesion between PDMS and PFOTCS. No signs of lift-off were detected. The wafers were then placed in NI555 for 2.5 hours and inspected. Unfortunately, the longer duration caused fluid to get trapped under the PDMS layer and caused great non-uniformities. A dehydration bake at 110°C after soaking in DI water was tried to minimize the non-uniformities. However, most microelectrode arrays were rendered unusable for further processing, leaving two arrays for further processing. At this point in the project, starting another process run would not allow me to finish on time. Hence, the processing of the non-uniform devices was pursued while being aware that it impacted further processing negatively.

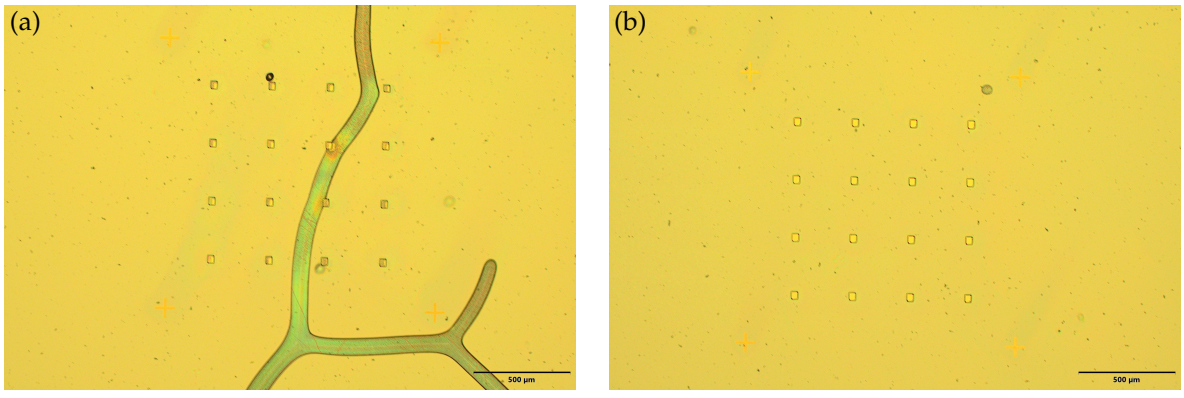

Figure 5.8: The impact of sonication during photoresist stripping with NI555. Some MEAs (a) had folds in the PDMS layer, while (b) others did not.

In Figure 5.7b, the profile of PDMS and the patterned hole is shown. A slope is visible from 40 μm to 50 μm. Assuming it a linear slope, the angle can be computed and compared to the designed angle (8 μm height, 16 μm width).

$$\theta = tan^{-1}(\frac{h}{w}) = 28.8° \quad \text{compared to} \quad 26.6°\text{(designed)} \tag{5.1}$$

The patterning of the PDMS passivation layer can therefore be said to have been successful.

5.6. PEDOT:PSS

After the patterning of PDMS, the sample is treated with a O_2 plasma surface treatment at low power (20W) for 60s. The O_2 plasma removes remaining exposed PFOTCS and creates hydrophilic groups at the PDMS surface, which is necessary before spin coating PEDOT:PSS. PEDOT:PSS is a hydrophilic nanodispersion and would not spread uniformly on hydrophobic surfaces. PEDOT:PSS is mixed with EG (5% v/v), DBSA (0.5% m/m) and degassed with the Thinky ARE-250. Then GOPS (1% v/v) is added and the mixture is again degassed. Before applying the liquid on the PDMS substrate, it is filtered with a 0.45 μm-polytetrafluoroethylene (PTFE) filter. The top-side of the wafer was fully covered with PEDOT:PSS and spin coated at 2000 rpm. The wafer was then soft-baked at 100°C for 1 minute and again the wafer was covered in PEDOT:PSS and spin coated at 2000 rpm. This was done to increase the thickness of PEDOT:PSS while maintaining uniformity. The wafer was then hard-baked in an oven (Memmert) at 110°C for 1 hour.

An important aspect of spin coating PEDOT:PSS was the question: will PEDOT:PSS connect well through the passivation layer? The result is shown in Figure 5.9. PEDOT:PSS seemed to have spread evenly over the array, as no color difference outside the electrode holes are seen. In an electrode hole, the step height of PEDOT:PSS is indicated by the color difference. Interesting is that the color pattern is similar in every direction, hinting that the undercut of the photoresist supported a similar sloped profile. Looking at Figure 5.7b, the slope at the right side is angled at $\approx 36.9°$, which might be sufficient for a PEDOT:PSS connection. Another explanation is that PEDOT:PSS filled the electrode hole and during the evaporation stage of spin coating, this profile emerged with the most evaporation occuring in the middle (and most exposed to air) part. More investigation into PEDOT:PSS spin coating across height differences is needed to understand this phenomenon fully. For now, the result seems satisfactory for creating a 30 μm by 30 μm PEDOT:PSS electrode on PDMS.

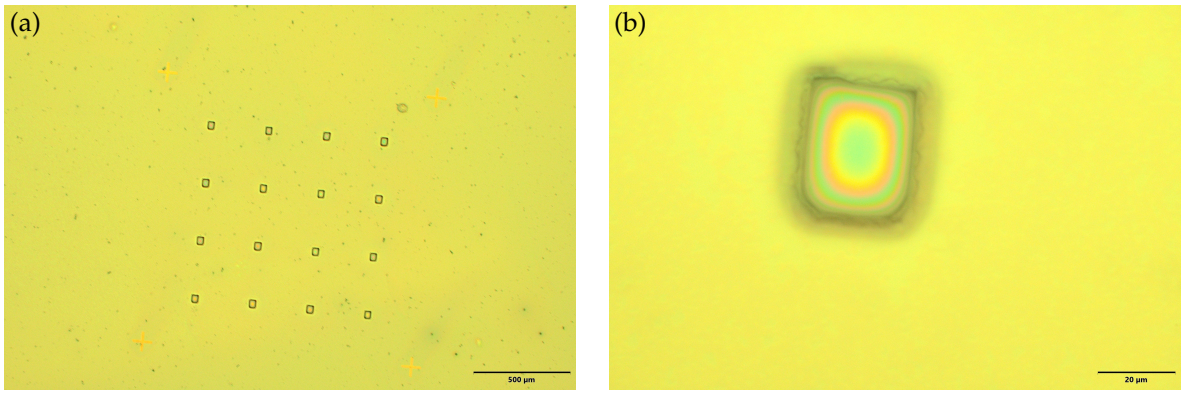

Figure 5.9: The result of the spin coating step of PEDOT:PSS on patterned PDMS with (a) the full MEA and (b) a single electrode.

In the process flow, step 10 is achieved at this point. The next step is to pattern the PEDOT:PSS with lithography. A dehydration bake was performed at 110°C for 10 minutes, followed by a HMDS treatment for 1 minute and 30 seconds. The HMDS is used to make the surface of PEDOT:PSS more hydrophobic so photoresist spreads uniformly. The HMDS hypothetically bonds with the silane groups in GOPS and was demonstrated to work before by M. Shah. AZNLOF2020 was used as photoresist to minimize exposure times. The elaborate recipe for this step can be found in Appendix E.3. A microelectrode array before O_2 RIE etch and after are shown in Figure 5.10.

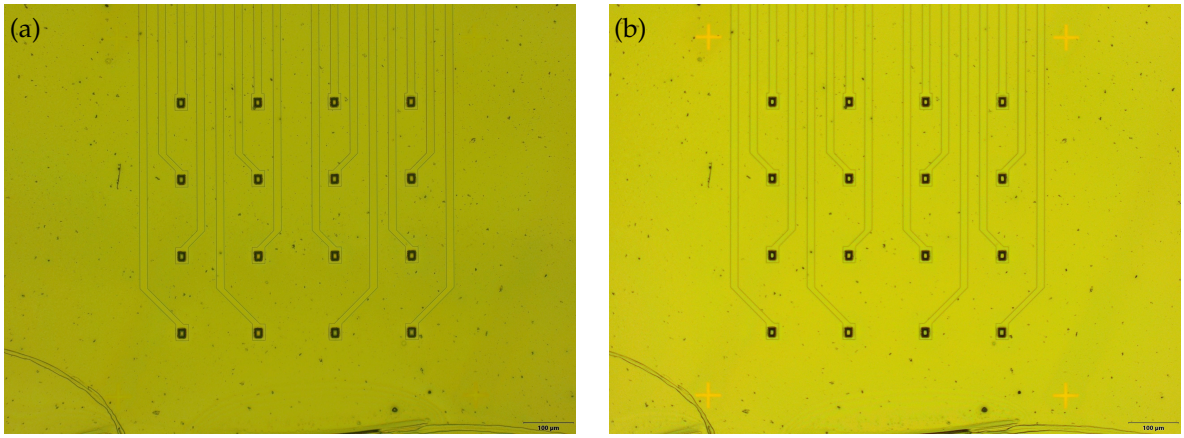

Figure 5.10: A microelectrode array (a) before and (b) after the O_2 RIE step. The PEDOT:PSS tracks can be dinstinguished well after etching and are well aligned with the array.

The process has achieved patterned PEDOT:PSS electrodes and tracks on PDMS so far. The next step is to connect the PEDOT:PSS to Au tracks and create a back-end connection for device characterization.

5.7. Metal layer

In the microfabrication process, steps 15-17 should now be taken. The issue with trapped liquid under the PDMS was mentioned before and came up again after the photoresist stripping with DMSO. DMSO is a flammable liquid and has a flashpoint temperature of 87◦C. Soaking in DI water for 10 minutes seemed to have flushed out DMSO. A dehydration bake at 110°C for 10 minutes was preceded by a test bake at 90°C to test if no DMSO was present. The 10 minute dehydration bake did not remove trapped DI water under PDMS. HMDS was therefore not attempted, since HMDS requires water to be removed to be successful. AZNLOF2020 photoresist was spin coated and exposed according to the recipe in Appendix E.4. However, after the exposure with the laser writer, it was discovered that the pneumatic focusing damaged the PDMS layer and blew off particles, shown in Figure 5.11. It was decided that no reattempts could be made with the current wafer. Unfortunately, inspection of the wafer after development showed that the photoresist layer had lifted off fully from the PDMS. The metallization step was therefore unsuccesful and requires more optimization of PDMS adhesion and photoresist adhesion.

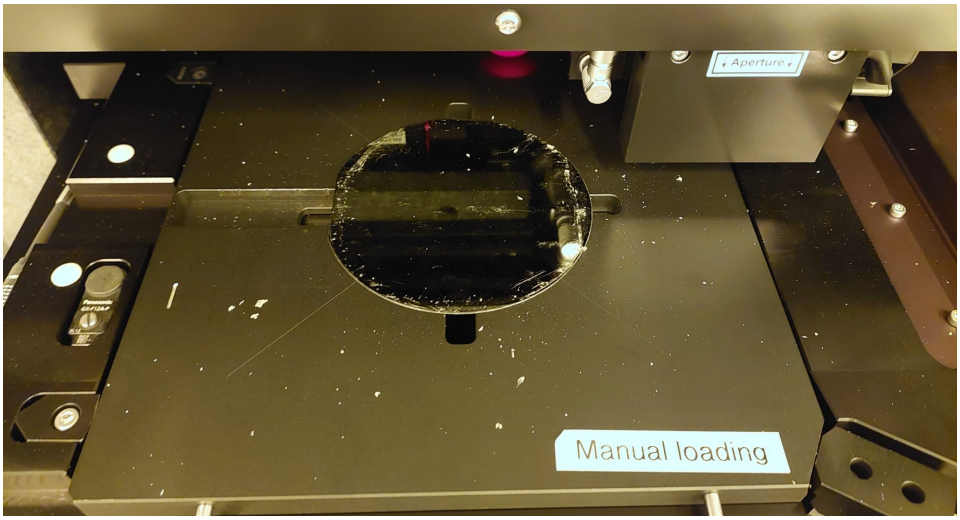

Figure 5.11: The result of pneumatic focusing on the PDMS substrate on PFOTCS. PDMS particles are spread everywhere due to the pneumatic airflow.

5.8. Device lift-off

Since the device did not have any metal traces, connecting to the microelectrode array and its 30 μm thick traces proved difficult. Thermal bonding of the device to glass was tried [116] . A clean glass wafer was surface treated with O_2 plasma at 200 W for 2 minutes. The glass wafer was then laid on top of the PDMS layer, pressed together by placing a glass beaker on top and put on a hotplate at 80°C for 2 hours. The thermal bonding was not successful and the glass wafer came off without PDMS. The non-uniformity of the PDMS layer may cause poor adhesion. Next, Kapton tape was used to pull off devices and flip them for characterization. The Kapton tape succesfully peeled of the PDMS layer, but proved a mistake upon inspection of the silicon wafer. Since the PEDOT:PSS electrodes did not have a supporting PDMS layer on the back, most electrodes remained on the silicon wafer. It is shown in Figure 5.12.

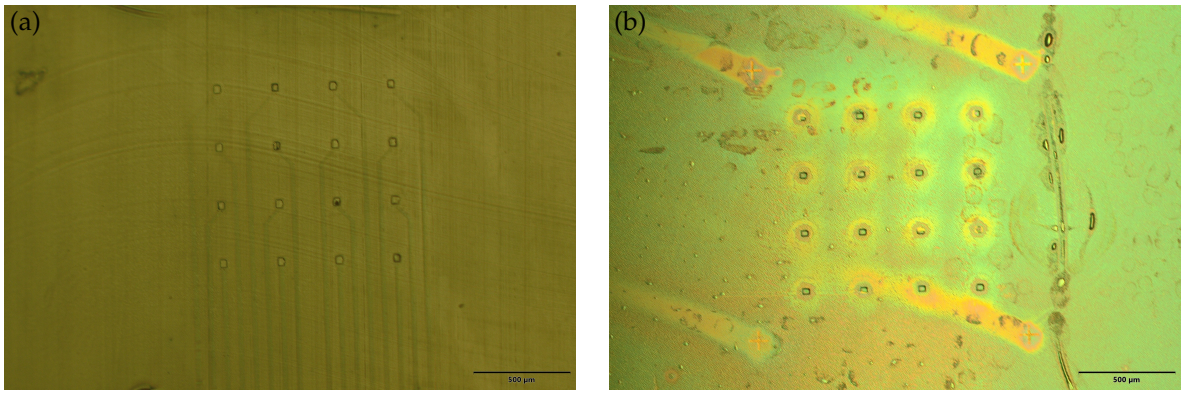

Figure 5.12: The outcome of the Kapton peel-off. (a) The PDMS layer and PEDOT:PSS tracks came off well, but (b) most PEDOT:PSS electrodes remained on the silicon substrate. It is most likely due to no supporting layer on the back of the PEDOT:PSS electrodes, which in the flowchart would have been PDMS. For thermal bonding it seemed best to not have an additional PDMS layer, so the PEDOT:PSS tracks would lay on a rigid substrate and be easier to connect to with rigid probes. Before the Kapton peel-off, spin coating PDMS on top of the wafer would have been better as it is expected to improve the peel-off of PEDOT:PSS electrodes. However, the electrode sizes that would be in contact with the electrolyte can be observed well and show sub 100 μm dimensions, which was the goal of this project.

5.9. Summary

The new workflow to fabricate 30 μm by 30 μm PEDOT:PSS electrodes on PDMS was shown and discussed in this chapter. The patterning of PDMS using grey-scale lithography was successful and PEDOT:PSS seemed to connect through the passivation layer, which is the main interest of this study. Back-end connections were not successful within the set timeframe and requires more optimization, but other projects have shown successful connections between Au and PEDOT:PSS [102] and Au and PDMS [103]. It is therefore not a critical step in understanding PEDOT:PSS and PDMS microelectrode array devices and is expected to be solvable with more time.

6
Conclusion

6.1. Conclusion

PEDOT:PSS is a well established conducting polymer with incredible potential for neural interface applications due to its mixed ionic-electronic conduction. Meanwhile, PDMS is an established biocompatible and soft material in microfluidic devices. Few studies exist that combine the two materials for neural interface applications with state-of-the-art spatial resolution. The main objective of this project was to contribute to an understanding of the materials PEDOT:PSS and PDMS for microelectrode array devices. The main research question was formulated as:

How can sub-100 μm diameter PEDOT:PSS-only electrodes be fabricated on PDMS substrates thinner than 70 μm for neural interface applications?

and served as an explorative question. The project was started with an exploration of the materials PEDOT:PSS and PDMS and their interface. Extensive characterization showed that PEDOT:PSS behaved similarly on PDMS compared to SiO_2 and Au and that the adhesion between PEDOT:PSS with GOPS as crosslinker and PDMS is stronger than PDMS and Ti/Au. Next, a microelectrode array design was proposed with a new patterning technique: overhanging photoresist structures using grey-scale lithography can pattern vias for thin films through thick (>5 μm) layers. Sixteen 30 μm by 30 μm electrodes, PEDOT:PSS and Au hybrid traces, and a backend connector were designed and selected. A completely novel microfabrication flowchart was created and executed with success, though partially due to time constraints. A backend connection could not be made due to a photoresist adhesion failure and therefore characterization of the microelectrode array was not possible. However, the main research question can be answered by showing the results up to patterning PEDOT:PSS traces, demonstrating a fabrication method to create sub-100 μm diameter PEDOT:PSS electrodes on a PDMS passivation layer thinner than 10 μm. The research question is therefore satisfactorily answered. Future work is heartily recommended, as the timeframe proved too short for optimization of all steps. The potential of state-of-the-art PEDOT:PSS and PDMS devices is clear and worth investigating and characterizing in more detail.

6.2. Recommendations

The project demonstrated PDMS patterning with spatial resolution comparable to state-of-the-art microelectrode array devices. A novel microfabrication workflow was established and executed. However, due to time constraints the workflow is not fully optimized yet. What follows are the issues encountered during the fabrication and recommendations on how to solve them. They are listed following the order of the microfabrication steps in Figure 5.1.

- The process does not include contaminating metals (Fe, Au, Cu, etc) until PEDOT:PSS is spin coated. Therefore, the process can be treated as non-contaminated in the EKL cleanroom until PEDOT:PSS spin coating. This enables the usage of more tools and generally a faster and more adaptable workflow in a shared user facility.
- The grey-scale lithography can and should be optimized more. Dose testing takes significant exposure time (up to 10 hours!) with the MLA 150, which was not known before embarking on this project. Dose testing was therefore not fully optimized. The absorption coefficient of AZNLOF2070 was also defined in the range of 0.3-0.4 μm^{-1}. This led to uncertainty about the initial exposure dose and multiple attempts to pinpoint the correct dose for crosslinking 10 μ thick NLOF2070 resist fully. The dose tests were not fully completed and a knowledge gap is left between 400 and 800 mJ/cm^2. Scanning electron microscopy (SEM) is the best way of determining the quality of the grey-scale lithography but also takes significantly more time than other inspection methods.

- Optimize the PDMS spin coating step. An issue with the spin coater, which was the only one allowed for PDMS spin coating, prevented spin coating at rotational speeds higher than 3000 rpm. Consequently, PDMS layers thinner than 15 μ were not achievable. Exploring PDMS spin coating at, for example, 8000 rpm would allow direct fabrication of thin PDMS layers and skip an extra etching step. Low ramp speeds should still be used to let PDMS flow around the photoresist pillars.
- The photoresist removal after spincoating/etching PDMS needs optimization. The issue that significantly distorted the microfabrication process was liquid ingress under the PDMS layer. Initial attempts showed that the adhesion between PDMS and PFOTCS can withstand low power sonication at 60°C for 10 minutes. However, prolonged treatment caused NI555 to get under the PDMS and cause non-uniformities, even after a dehydration bake. Removal of the photoresist without distorting the PDMS layer should be investigated and optimized.
- The adhesion between PDMS and photoresist (AZNLOF2020) was poor and prevented successful development. HMDS treatment was ignored in this project due to trapped water caused by the previously mentioned issue. If this issue is resolved, HMDS treatment of PDMS is possible and should improve the adhesion between PDMS and photoresist. Additionally, if the uniformity of the PDMS layer is not distorted, optical focussing of the laser writer is possible and should not damage the PDMS layer by air pressure.

These recommendations are tailored to the microfabrication process of the PEDOT:PSS/PDMS microelectrode arrays. However, more can be said on the potential behind this work and possible future work. Possible lines of continuation include:

- PEDOT:PSS integration with PDMS microfluidic devices. The combination of PEDOT:PSS and PDMS into a microelectrode array can be further developed into a microelectrode array embedded into a microfluidic device.
- Cell culture measurements with a PEDOT:PSS/PDMS microelectrode array to establish biocompatibility and investigate single-unit activity recording.
- Long-term reliability testing of PEDOT:PSS/PDMS devices. An indication of strong adhesion and long-term reliability has been demonstrated in this project but is limited in its scope. Following setups proposed in Nature Protocols [16] can establish and quantify the long-term reliability in more detail.

References

[1] P. Kennedy, R. Bakay, M. Moore, K. Adams, and J. Goldwaithe, "Direct control of a computer from the human central nervous system," *IEEE Transactions on Rehabilitation Engineering*, vol. 8, no. 2, pp. 198–202, Jun. 2000. DOI: 10.1109/86.847815.

[2] P. Doggers (PeterDoggers). "Paraplegic Plays Chess Helped By Neuralink Chip In Brain," Chess.com. [Online]. Available: https://www.chess.com/news/view/paraplegic-plays-chess-helped-by-neuralink-chip-in-brain.

[3] L. N. Ayton et al., "An update on retinal prostheses," *Clinical Neurophysiology*, vol. 131, no. 6, pp. 1383–1398, Jun. 2020. DOI: 10.1016/j.clinph.2019.11.029.

[4] R. P. Carlyon and T. Goehring, "Cochlear Implant Research and Development in the Twenty-first Century: A Critical Update," *Journal of the Association for Research in Otolaryngology*, vol. 22, no. 5, pp. 481–508, Oct. 2021. DOI: 10.1007/s10162-021-00811-5.

[5] H. Lorach et al., "Walking naturally after spinal cord injury using a brain–spine interface," *Nature*, vol. 618, no. 7963, pp. 126–133, Jun. 1, 2023. DOI: 10.1038/s41586-023-06094-5.

[6] J. D. Steinmetz et al., "Global, regional, and national burden of disorders affecting the nervous system, 1990–2021: A systematic analysis for the Global Burden of Disease Study 2021," *The Lancet Neurology*, vol. 23, no. 4, pp. 344–381, Apr. 2024. DOI: 10.1016/S1474-4422(24)00038-3.

[7] World Health Organization, *Intersectoral Global Action Plan on Epilepsy and Other Neurological Disorders 2022–2031*. World Health Organization, 2023.

[8] *The BRAIN Initiative Alliance*, https://www.braininitiative.org/.

[9] G. Pipa, M. Chiappalone, H. H. Pol, F. Newell, and A. Soria-frisch, "Human Brain Project," Publications Office of the European Union, Tech. Rep., 2024, p. 61.

[10] M.-m. Poo, J.-l. Du, N. Y. Ip, Z.-Q. Xiong, B. Xu, and T. Tan, "China Brain Project: Basic Neuroscience, Brain Diseases, and Brain-Inspired Computing," *Neuron*, vol. 92, no. 3, pp. 591–596, Nov. 2016. DOI: 10.1016/j.neuron.2016.10.050.

[11] L. M. Biga et al., "12.5 The Action Potential," *Anatomy & Physiology*, Sep. 26, 2019. [Online]. Available: https://open.oregonstate.education/aandp/chapter/12-5-the-action-potential/.

[12] J. T. Robinson et al., "Developing Next-Generation Brain Sensing Technologies—A Review," *IEEE Sensors Journal*, vol. 19, no. 22, pp. 10 163–10 175, Nov. 2019. DOI: 10.1109/JSEN.2019.2931159.

[13] J. Rivnay, H. Wang, L. Fenno, K. Deisseroth, and G. G. Malliaras, "Next-generation probes, particles, and proteins for neural interfacing," *Science Advances*, vol. 3, no. 6, e1601649, Jun. 2017. DOI: 10.1126/sciadv.1601649.

[14] C. M. Proctor, J. Rivnay, and G. G. Malliaras, "Understanding volumetric capacitance in conducting polymers," *Journal of Polymer Science Part B: Polymer Physics*, vol. 54, no. 15, pp. 1433–1436, 2016. DOI: 10.1002/polb.24038.

[15] C. M. Lewis, C. Boehler, R. Liljemalm, P. Fries, T. Stieglitz, and M. Asplund, "Recording Quality Is Systematically Related to Electrode Impedance," *Advanced Healthcare Materials*, p. 2 303 401, Feb. 2024. DOI: 10.1002/adhm.202303401.

[16] C. Boehler, S. Carli, L. Fadiga, T. Stieglitz, and M. Asplund, "Tutorial: Guidelines for standardized performance tests for electrodes intended for neural interfaces and bioelectronics," *Nature Protocols*, vol. 15, no. 11, pp. 3557–3578, Nov. 2020. DOI: 10.1038/s41596-020-0389-2.

[17] P. Campbell, K. Jones, R. Huber, K. Horch, and R. Normann, "A silicon-based, three-dimensional neural interface: Manufacturing processes for an intracortical electrode array," *IEEE Transactions on Biomedical Engineering*, vol. 38, no. 8, pp. 758–768, Aug. 1991. DOI: 10.1109/10.83588.

[18] R. Biran, D. C. Martin, and P. A. Tresco, "Neuronal cell loss accompanies the brain tissue response to chronically implanted silicon microelectrode arrays," *Experimental Neurology*, vol. 195, no. 1, pp. 115–126, Sep. 2005. DOI: 10.1016/j.expneurol.2005.04.020.

[19] J. C. Barrese et al., "Failure mode analysis of silicon-based intracortical microelectrode arrays in non-human primates," *Journal of Neural Engineering*, vol. 10, no. 6, p. 066 014, Nov. 2013. DOI: 10.1088/1741-2560/10/6/066014.

[20] I. Uguz and K. L. Shepard, "Spatially controlled, bipolar, cortical stimulation with high-capacitance, mechanically flexible subdural surface microelectrode arrays," *Science Advances*, vol. 8, no. 42, eabq6354, Oct. 2022. DOI: 10.1126/sciadv.abq6354.

[21] L. Ma, D. J. Wisniewski, C. Cea, D. Khodagholy, and J. N. Gelinas, "High-Density, Conformable Conducting Polymer-Based Implantable Neural Probes for the Developing Brain," *Advanced Healthcare Materials*, p. 2 304 164, Apr. 2024. DOI: 10.1002/adhm.202304164.

[22] Y. Wu et al., "Ultraflexible electrodes for recording neural activity in the mouse spinal cord during motor behavior," *Cell Reports*, vol. 43, no. 5, p. 114 199, May 2024. DOI: 10.1016/j.celrep.2024.114199.

[23] "Saline, Silicone Gel, and Alternative Breast Implants - Guidance for Industry and Food and Drug Administration Staff,"

[24] A. K. Waafi, N. Gaio, W. F. Quiros-Solano, P. Dijkstra, P. M. Sarro, and R. Dekker, "Low-Impedance PEDOT:PSS MEA Integrated in a Stretchable Organ-on-Chip Device," *IEEE Sensors Journal*, vol. 20, no. 3, pp. 1150–1157, Feb. 2020. DOI: 10.1109/JSEN.2019.2946854.

[25] G. Li et al., "PEDOT:PSS/Grafted-PDMS Electrodes for Fully Organic and Intrinsically Stretchable Skin-like Electronics," *ACS Applied Materials & Interfaces*, vol. 11, no. 10, pp. 10 373–10 379, Mar. 2019. DOI: 10.1021/acsami.8b20255.

[26] C. M. Tringides et al., "Viscoelastic surface electrode arrays to interface with viscoelastic tissues," *Nature Nanotechnology*, vol. 16, no. 9, pp. 1019–1029, Sep. 2021. DOI: 10.1038/s41565-021-00926-z.

[27] D. Won et al., "Digital selective transformation and patterning of highly conductive hydrogel bioelectronics by laser-induced phase separation," *SCIENCE ADVANCES*, 2022.

[28] A. J. Boys and S. T. Keene, "Bioelectronic interfacial matching for superior implant design," *Cell Reports Physical Science*, vol. 5, no. 8, p. 101 877, Aug. 2024. DOI: 10.1016/j.xcrp.2024.101877.

[29] P. Oldroyd, J. Gurke, and G. G. Malliaras, "Stability of Thin Film Neuromodulation Electrodes under Accelerated Aging Conditions," *Advanced Functional Materials*, vol. 33, no. 1, p. 2 208 881, Jan. 2023. DOI: 10.1002/adfm.202208881.

[30] A. Blau et al., "Flexible, all-polymer microelectrode arrays for the capture of cardiac and neuronal signals," *Biomaterials*, vol. 32, no. 7, pp. 1778–1786, Mar. 2011. DOI: 10.1016/j.biomaterials.2010.11.014.

[31] G. Filho, C. Júnior, B. Spinelli, I. Damasceno, F. Fiuza, and E. Morya, "All-Polymeric Electrode Based on PEDOT:PSS for In Vivo Neural Recording," *Biosensors*, vol. 12, no. 10, p. 853, Oct. 2022. DOI: 10.3390/bios12100853.

[32] P. Oldroyd et al., "Stretchable Device for Simultaneous Measurements of Contractility and Electrophysiology of Neuromuscular Tissue in the Gastrointestinal Tract," *Advanced Materials*, vol. 36, no. 19, p. 2 312 735, May 2024. DOI: 10.1002/adma.202312735.

[33] J. E. B. Randles, "Kinetics of rapid electrode reactions," *Discussions of the Faraday Society*, vol. 1, p. 11, 1947. DOI: 10.1039/df9470100011.

[34] M. Hill et al., "Quantitative simulation of extracellular single unit recording from the surface of cortex," *Journal of Neural Engineering*, vol. 15, no. 5, p. 056 007, Jul. 2018. DOI: 10.1088/1741-2552/aacdb8.

[35] G. Hong and C. M. Lieber, "Novel electrode technologies for neural recordings," *Nature Reviews Neuroscience*, vol. 20, no. 6, pp. 330–345, Jun. 2019. DOI: 10.1038/s41583-019-0140-6.

[36] M. Ferguson, D. Sharma, D. Ross, and F. Zhao, "A Critical Review of Microelectrode Arrays and Strategies for Improving the Neural Interface," *Advanced healthcare materials*, vol. 8, no. 19, e1900558, Oct. 2019. DOI: 10.1002/adhm.201900558.

[37] M. Zhang, Z. Tang, X. Liu, and J. Van der Spiegel, "Electronic neural interfaces," *Nature Electronics*, vol. 3, no. 4, pp. 191–200, Apr. 2020. DOI: 10.1038/s41928-020-0390-3.

[38] S. M. Wellman et al., "A Materials Roadmap to Functional Neural Interface Design," *Advanced Functional Materials*, vol. 28, no. 12, p. 1 701 269, Mar. 2018. DOI: 10.1002/adfm.201701269.

[39] Z. Lu, A. Pavia, A. Savva, L. Kergoat, and R. M. Owens, "Organic microelectrode arrays for bioelectronic applications," *Materials Science and Engineering: R: Reports*, vol. 153, p. 100 726, May 2023. DOI: 10.1016/j.mser.2023.100726.

[40] M. Mierzejewski, H. Steins, P. Kshirsagar, and P. D. Jones, "The noise and impedance of microelectrodes," *Journal of Neural Engineering*, vol. 17, no. 5, p. 052 001, Oct. 2020. DOI: 10.1088/1741-2552/abb3b4.

[41] A. A. Faisal, L. P. J. Selen, and D. M. Wolpert, "Noise in the nervous system," *Nature Reviews Neuroscience*, vol. 9, no. 4, pp. 292–303, Apr. 2008. DOI: 10.1038/nrn2258.

[42] J. P. Neto et al., "Does Impedance Matter When Recording Spikes With Polytrodes?" *Frontiers in Neuroscience*, vol. 12, p. 715, Oct. 8, 2018. DOI: 10.3389/fnins.2018.00715.

[43] K. A. Ludwig, J. D. Uram, J. Yang, D. C. Martin, and D. R. Kipke, "Chronic neural recordings using silicon microelectrode arrays electrochemically deposited with a poly(3,4-ethylenedioxythiophene) (PEDOT) film," *Journal of Neural Engineering*, vol. 3, no. 1, pp. 59–70, Mar. 2006. DOI: 10.1088/1741-2560/3/1/007.

[44] S. P. Lacour, G. Courtine, and J. Guck, "Materials and technologies for soft implantable neuroprostheses," *Nature Reviews Materials*, vol. 1, no. 10, p. 16 063, Sep. 2016. DOI: 10.1038/natrevmats.2016.63.

[45] A. Carnicer-Lombarte, S.-T. Chen, G. G. Malliaras, and D. G. Barone, "Foreign Body Reaction to Implanted Biomaterials and Its Impact in Nerve Neuroprosthetics," *Frontiers in Bioengineering and Biotechnology*, vol. 9, p. 622 524, Apr. 2021. DOI: 10.3389/fbioe.2021.622524.

[46] T. D. Y. Kozai, A. S. Jaquins-Gerstl, A. L. Vazquez, A. C. Michael, and X. T. Cui, "Brain Tissue Responses to Neural Implants Impact Signal Sensitivity and Intervention Strategies," *ACS Chemical Neuroscience*, vol. 6, no. 1, pp. 48–67, Jan. 2015. DOI: 10.1021/cn500256e.

[47] J. K. Nguyen et al., "Mechanically-compliant intracortical implants reduce the neuroinflammatory response," *Journal of Neural Engineering*, vol. 11, no. 5, p. 056 014, Oct. 1, 2014. DOI: 10.1088/1741-2560/11/5/056014.

[48] J. P. Seymour and D. R. Kipke, "Neural probe design for reduced tissue encapsulation in CNS," *Biomaterials*, vol. 28, no. 25, pp. 3594–3607, Sep. 2007. DOI: 10.1016/j.biomaterials.2007.03.024.

[49] C. Orlemann, C. Boehler, R. N. Kooijmans, B. Li, P. R. Roelfsema, and M. Asplund, "Flexible Polymer Electrodes for Stable Prosthetic Visual Perception in Mice," *Advanced Healthcare Materials*, vol. 13, no. 15, p. 2 304 169, Jun. 2024. DOI: 10.1002/adhm.202304169.

[50] A. Ramirez, D. Van der Laan, M. Shah, L. Wang, E. Zeglio, and A. Savva, "Pedot:pss - a key material for bioelectronics," Submitted.

[51] G. Heywang and F. Jonas, "Poly(alkylenedioxythiophene)s—new, very stable conducting polymers," *Advanced Materials*, vol. 4, no. 2, pp. 116–118, Feb. 1992. DOI: 10.1002/adma.19920040213.

[52] H. Yamato, M. Ohwa, and W. Wernet, "Stability of polypyrrole and poly(3,4-ethylenedioxythiophene) for biosensor application," *Journal of Electroanalytical Chemistry*, vol. 397, no. 1-2, pp. 163–170, Nov. 1995. DOI: 10.1016/0022-0728(95)04156-8.

[53] X. Cui and D. C. Martin, "Electrochemical deposition and characterization of poly(3,4-ethylenedioxythiophene) on neural microelectrode arrays," *Sensors and Actuators B: Chemical*, vol. 89, no. 1-2, pp. 92–102, Mar. 2003. DOI: 10.1016/S0925-4005(02)00448-3.

[54] M. Berggren and A. Richter-Dahlfors, "Organic Bioelectronics," *Advanced Materials*, vol. 19, no. 20, pp. 3201–3213, Oct. 2007. DOI: 10.1002/adma.200700419.

[55] B. D. Paulsen, K. Tybrandt, E. Stavrinidou, and J. Rivnay, "Organic mixed ionic–electronic conductors," *Nature Materials*, vol. 19, no. 1, pp. 13–26, Aug. 2019. DOI: 10.1038/s41563-019-0435-z.

[56] A. Elschner, S. Kirchmeyer, W. Lovenich, U. Merker, and K. Reuter, *PEDOT: Principles and Applications of an Intrinsically Conductive Polymer*, 0th ed. CRC Press, Nov. 2010. DOI: 10.1201/b10318.

[57] S. T. Keene et al., "Efficient Electronic Tunneling Governs Transport in Conducting Polymer-Insulator Blends," *Journal of the American Chemical Society*, vol. 144, no. 23, pp. 10 368–10 376, Jun. 2022. DOI: 10.1021/jacs.2c02139.

[58] X. Crispin et al., "The Origin of the High Conductivity of Poly(3,4-ethylenedioxythiophene)-Poly(styrenesulfonate) (PEDOT-PSS) Plastic Electrodes," *Chemistry of Materials*, vol. 18, no. 18, pp. 4354–4360, Sep. 2006. DOI: 10.1021/cm061032+.

[59] H. Shi, C. Liu, Q. Jiang, and J. Xu, "Effective Approaches to Improve the Electrical Conductivity of PEDOT:PSS: A Review," *Advanced Electronic Materials*, vol. 1, no. 4, p. 1 500 017, Apr. 2015. DOI: 10.1002/aelm.201500017.

[60] N. Kim et al., "Highly Conductive PEDOT:PSS Nanofibrils Induced by Solution-Processed Crystallization," *Advanced Materials*, vol. 26, no. 14, pp. 2268–2272, 2014. DOI: 10.1002/adma.201304611.

[61] R. Noriega et al., "A general relationship between disorder, aggregation and charge transport in conjugated polymers," *Nature Materials*, vol. 12, no. 11, pp. 1038–1044, Nov. 2013. DOI: 10.1038/nmat3722.

[62] E. Hosseini, V. O. Kollath, and K. Karan, "The key mechanism of conductivity in PEDOT:PSS thin films exposed by anomalous conduction behaviour upon solvent-doping and sulfuric acid post-treatment," *Journal of Materials Chemistry C*, vol. 8, no. 12, pp. 3982–3990, Mar. 2020. DOI: 10.1039/C9TC06311K.

[63] E. Stavrinidou et al., "Direct Measurement of Ion Mobility in a Conducting Polymer," *Advanced Materials*, vol. 25, no. 32, pp. 4488–4493, Aug. 2013. DOI: 10.1002/adma.201301240.

[64] S. T. Keene, A. Rao, and G. G. Malliaras, "The relationship between ionic-electronic coupling and transport in organic mixed conductors," *Science Advances*, vol. 9, no. 35, eadi3536, Sep. 2023. DOI: 10.1126/sciadv.adi3536.

[65] J. Rivnay et al., "Structural control of mixed ionic and electronic transport in conducting polymers," *Nature Communications*, vol. 7, no. 1, p. 11 287, Apr. 2016. DOI: 10.1038/ncomms11287.

[66] A. Savva et al., "Balancing Ionic and Electronic Conduction for High-Performance Organic Electrochemical Transistors," *Advanced Functional Materials*, vol. 30, no. 11, p. 1 907 657, Mar. 2020. DOI: 10.1002/adfm.201907657.

[67] A. Savva, S. Wustoni, and S. Inal, "Ionic-to-electronic coupling efficiency in PEDOT:PSS films operated in aqueous electrolytes," *Journal of Materials Chemistry C*, vol. 6, no. 44, pp. 12 023–12 030, 2018. DOI: 10.1039/C8TC02195C.

[68] S.-M. Kim et al., "Influence of PEDOT:PSS crystallinity and composition on electrochemical transistor performance and long-term stability," *Nature Communications*, vol. 9, no. 1, p. 3858, Sep. 2018. DOI: 10.1038/s41467-018-06084-6.

[69] A. Savva et al., "3D organic bioelectronics for electrical monitoring of human adult stem cells," *Materials Horizons*, vol. 10, no. 9, pp. 3589–3600, 2023. DOI: 10.1039/D3MH00785E.

[70] J. Rivnay, R. M. Owens, and G. G. Malliaras, "The Rise of Organic Bioelectronics," *Chemistry of Materials*, vol. 26, no. 1, pp. 679–685, Sep. 2013. DOI: 10.1021/cm4022003.

[71] M. Ganji, A. Tanaka, V. Gilja, E. Halgren, and S. A. Dayeh, "Scaling Effects on the Electrochemical Stimulation Performance of Au, Pt, and PEDOT:PSS Electrocorticography Arrays," *Advanced Functional Materials*, vol. 27, no. 42, p. 1 703 019, Nov. 2017. DOI: 10.1002/adfm.201703019.

[72] D. Khodagholy et al., "Highly Conformable Conducting Polymer Electrodes for In Vivo Recordings," *Advanced Materials*, vol. 23, no. 36, Sep. 2011. DOI: 10.1002/adma.201102378.

[73] D. Khodagholy et al., "NeuroGrid: Recording action potentials from the surface of the brain," *Nature Neuroscience*, vol. 18, no. 2, pp. 310–315, Feb. 2015. DOI: 10.1038/nn.3905.

[74] G. Dijk, A. Kaszas, J. Pas, and R. P. O'Connor, "Fabrication and in vivo 2-photon microscopy validation of transparent PEDOT:PSS microelectrode arrays," *Microsystems & Nanoengineering*, vol. 8, no. 1, p. 90, Aug. 2022. DOI: 10.1038/s41378-022-00434-7.

[75] C. Boehler, F. Oberueber, S. Schlabach, T. Stieglitz, and M. Asplund, "Long-Term Stable Adhesion for Conducting Polymers in Biomedical Applications: IrOx and Nanostructured Platinum Solve the Chronic Challenge," *ACS Applied Materials & Interfaces*, vol. 9, no. 1, pp. 189–197, Jan. 2017. DOI: 10.1021/acsami.6b13468.

[76] C. Böhler et al., "Multilayer Arrays for Neurotechnology Applications (MANTA): Chronically Stable Thin-Film Intracortical Implants," *Advanced Science*, vol. 10, no. 14, p. 2 207 576, May 2023. DOI: 10.1002/advs.202207576.

[77] J. S. Ordonez, C. Boehler, M. Schuettler, and T. Stieglitz, "Long-term Adhesion Studies of Polyimide to Inorganic and Metallic Layers," *MRS Online Proceedings Library*, vol. 1466, no. 1, pp. 1–7, 1 Dec. 1, 2012. DOI: 10.1557/opl.2012.1198.

[78] Y. Mao, I. Pechenizkiy, T. Stieglitz, and T. Doll, "Numerical Evaluation on Residual Thermal Stress-Induced Delamination at PDMS–Metal Interface of Neural Prostheses," *Micromachines*, vol. 12, no. 6, p. 669, 6 Jun. 2021. DOI: 10.3390/mi12060669.

[79] A. Inoue, H. Yuk, B. Lu, and X. Zhao, "Strong adhesion of wet conducting polymers on diverse substrates," *Science Advances*, vol. 6, no. 12, eaay5394, Mar. 2020. DOI: 10.1126/sciadv.aay5394.

[80] S. Narayan, L. Stoica, A. Liess, and A. Reisinger, "Amplicoat® – Conductive Polymer Coating with Enhanced Durability and Performance for Chronic Implants," in *2021 Design of Medical Devices Conference*, Minneapolis, MN, USA: American Society of Mechanical Engineers, Apr. 2021, V001T08A001. DOI: 10.1115/DMD2021-1082.

[81] R. Moučka, M. Sedlačík, J. Osička, and V. Pata, "Mechanical properties of bulk Sylgard 184 and its extension with silicone oil," *Scientific Reports*, vol. 11, no. 1, p. 19 090, Sep. 27, 2021. DOI: 10.1038/s41598-021-98694-2.

[82] S. H. Tan, N.-T. Nguyen, Y. C. Chua, and T. G. Kang, "Oxygen plasma treatment for reducing hydrophobicity of a sealed polydimethylsiloxane microchannel," *Biomicrofluidics*, vol. 4, no. 3, p. 032 204, Sep. 30, 2010. DOI: 10.1063/1.3466882.

[83] B. Jiang, H. Guo, D. Chen, and M. Zhou, "Microscale investigation on the wettability and bonding mechanism of oxygen plasma-treated PDMS microfluidic chip," *Applied Surface Science*, vol. 574, p. 151 704, Feb. 1, 2022. DOI: 10.1016/j.apsusc.2021.151704.

[84] D. J. Lipomi, J. A. Lee, M. Vosgueritchian, B. C.-K. Tee, J. A. Bolander, and Z. Bao, "Electronic Properties of Transparent Conductive Films of PEDOT:PSS on Stretchable Substrates," *Chemistry of Materials*, vol. 24, no. 2, pp. 373–382, Dec. 2011. DOI: 10.1021/cm203216m.

[85] S. Middya et al., "Conducting Polymer Microelectrode Arrays for Simultaneous Electrophysiology and Advanced Brain Imaging," *Advanced Functional Materials*, p. 2 417 312, Jan. 2025. DOI: 10.1002/adfm.202417312.

[86] L. Luan et al., "Ultraflexible nanoelectronic probes form reliable, glial scar–free neural integration," *Science Advances*, vol. 3, no. 2, e1601966, Feb. 15, 2017. DOI: 10.1126/sciadv.1601966.

[87] R. Traeger, "Nonhermeticity of Polymeric Lid Sealants," *IEEE Transactions on Parts, Hybrids, and Packaging*, vol. 13, no. 2, pp. 147–152, Jun. 1977. DOI: 10.1109/TPHP.1977.1135193.

[88] K. Nanbakhsh et al., "On the longevity and inherent hermeticity of silicon-ICs: Evaluation of bare-die and PDMS-coated ICs after accelerated aging and implantation studies," *Nature Communications*, vol. 16, no. 1, p. 12, Jan. 2, 2025. DOI: 10.1038/s41467-024-55298-4.

[89] R. Komeri, N. Kasoju, and P. Anil Kumar, "In vitro cytotoxicity and cytocompatibility assays for biomaterial testing under regulatory platform," in *Biomedical Product and Materials Evaluation*, Elsevier, 2022, pp. 329–353. DOI: 10.1016/B978-0-12-823966-7.00009-8.

[90] J. Dolbow and M. Gosz, "Effect of out-of-plane properties of a polyimide film on the stress fields in microelectronic structures," *Mechanics of Materials*, vol. 23, no. 4, pp. 311–321, Aug. 1996. DOI: 10.1016/0167-6636(96)00021-X.

[91] unknown, *SCS Parylene Properties*, Specialty Coating Systems. [Online]. Available: https://scscoatings.com/technical-library/en/download/2249/?tmstv=1745409029.

[92] unknown, *Kapton® Summary of Properties*, DuPont. [Online]. Available: https://www.dupont.com/content/dam/electronics/amer/us/en/electronics/public/documents/en/EI-10142_Kapton-Summary-of-Properties.pdf.

[93] Y. Zhang, M. Ishida, Y. Kazoe, Y. Sato, and N. Miki, "Water-vapor permeability control of PDMS by the dispersion of collagen powder," *IEEJ Transactions on Electrical and Electronic Engineering*, vol. 4, no. 3, pp. 442–449, 2009. DOI: 10.1002/tee.20429.

[94] G. Soza, R. Grosso, C. Nimsky, P. Hastreiter, R. Fahlbusch, and G. Greiner, "Determination of the elasticity parameters of brain tissue with combined simulation and registration," *The International Journal of Medical Robotics and Computer Assisted Surgery*, vol. 1, no. 3, pp. 87–95, Sep. 2005. DOI: 10.1002/rcs.32.

[95] W. Zhang, G. Ferguson, and S. Tatic-Lucic, "Elastomer-supported cold welding for room temperature wafer-level bonding," in *17th IEEE International Conference on Micro Electro Mechanical Systems. Maastricht MEMS 2004 Technical Digest*, Jan. 2004, pp. 741–744. DOI: 10.1109/MEMS.2004.1290691.

[96] Edward Kang et al., "Large-scale, ultrapliable, and free-standing nanomembranes.," *Advanced Materials*, vol. 25, no. 15, pp. 2167–2173, Apr. 2013. DOI: 10.1002/adma.201204619.

[97] S. Hellstrom, *Basic models of spin coating*, Oct. 2007. [Online]. Available: http://large.stanford.edu/courses/2007/ph210/hellstrom1/.

[98] *Cnr_AZ_nLOF2000*, Instituto Nanoscienze Consiglio Nazionale Delle Richerche. [Online]. Available: https://litho.nano.cnr.it/wp-content/datasheets/AZ_nLOF2000.pdf.

[99] *Post Exposure Bake (PEB)*, MicroChemicals. [Online]. Available: http://www.microchemicals.com/downloads/application_notes.html.

[100] "ScanAsyst - Air | Silicon Nitride Probes. "[Online]. Available: https://www.brukerafmprobes.com/p-3726-scanasyst-air.aspx.

[101] A. Chelly, S. Glass, J. Belhassen, and A. Karsenty, "Broad review of four-point probe correction factors: Enhanced analytical model using advanced numerical and experimental cross-examination," *Results in Physics*, vol. 48, p. 106 445, May 2023. DOI: 10.1016/j.rinp.2023.106445.

[102] S. Middya et al., "Microelectrode Arrays for Simultaneous Electrophysiology and Advanced Optical Microscopy," *Advanced Science*, vol. 8, no. 13, p. 2 004 434, Jul. 2021. DOI: 10.1002/advs.202004434.

[103] L. Guo, G. S. Guvanasen, X. Liu, C. Tuthill, T. R. Nichols, and S. P. DeWeerth, "A PDMS-Based Integrated Stretchable Microelectrode Array (isMEA) for Neural and Muscular Surface Interfacing," *IEEE Transactions on Biomedical Circuits and Systems*, vol. 7, no. 1, pp. 1–10, Feb. 2013. DOI: 10.1109/TBCAS.2012.2192932.

[104] Liang Guo and S. DeWeerth, "Implementation of integratable PDMS-based conformable microelectrode arrays using a multilayer wiring interconnect technology," in *2009 Annual International Conference of the IEEE Engineering in Medicine and Biology Society*, Minneapolis, MN: IEEE, Sep. 2009, pp. 1619–1622. DOI: 10.1109/IEMBS.2009.5333218.

[105] M. Zia, B. Chung, S. Sober, and M. S. Bakir, "Flexible Multielectrode Arrays With 2-D and 3-D Contacts for In Vivo Electromyography Recording," *IEEE Transactions on Components, Packaging and Manufacturing Technology*, vol. 10, no. 2, pp. 197–202, Feb. 2020. DOI: 10.1109/TCPMT.2019.2963556.

[106] D. Khodagholy et al., "High transconductance organic electrochemical transistors," *Nature Communications*, vol. 4, no. 1, p. 2133, Jul. 2013. DOI: 10.1038/ncomms3133.

[107] E. Musk and Neuralink, *An Integrated Brain-Machine Interface Platform With Thousands of Channels (Preprint)*, Sep. 2019. DOI: 10.2196/preprints.16194.

[108] A. E. Rochford et al., "Functional neurological restoration of amputated peripheral nerve using biohybrid regenerative bioelectronics," *Science Advances*, vol. 9, no. 12, eadd8162, Mar. 2023. DOI: 10.1126/sciadv.add8162.

[109] A. Lunghi et al., "Ultra-Flexible μ-ECoG Arrays Based on PEDOT:PSS Micropillars," *Advanced Materials Interfaces*, p. 2 500 051, Mar. 20, 2025. DOI: 10.1002/admi.202500051.

[110] L. Guo, K. W. Meacham, S. Hochman, and S. P. DeWeerth, "A PDMS-Based Conical-Well Microelectrode Array for Surface Stimulation and Recording of Neural Tissues," *IEEE Transactions on Biomedical Engineering*, vol. 57, no. 10, pp. 2485–2494, Oct. 2010. DOI: 10.1109/TBME.2010.2052617.

[111] S. H. Chang, C.-H. Chiang, F.-S. Kao, C.-L. Tien, and C.-G. Wu, "Unraveling the Enhanced Electrical Conductivity of PEDOT:PSS Thin Films for ITO-Free Organic Photovoltaics," *IEEE Photonics Journal*, vol. 6, no. 4, pp. 1–7, Aug. 2014. DOI: 10.1109/JPHOT.2014.2331254.

[112] *KAM-LOR-PMGI-Datasheet-4.30.24-final-1*, Kayaku Advanced Materials. [Online]. Available: https://kayakuam.com/wp-content/uploads/2023/06/KAM-LOR-PMGI-Datasheet-4.30.24-final-1.pdf.

[113] "AZ® ECI 3007 Photoresist MicroChemicals GmbH," MicroChemicals GmbH. [Online]. Available: https://www.microchemicals.com/AZ-ECI-3007-Photoresist-3.785-l/1A003007.

[114] "MLA150 - Design Guidelines - UCSB Nanofab Wiki. "[Online]. Available: https://wiki.nanofab.ucsb.edu/wiki/MLA150_-_Design_Guidelines#Limitations_.26_Workarounds.

[115] *Dry_etching_photoresist*, MicroChemicals. [Online]. Available: https://www.microchemicals.com/dokumente/application_notes/dry_etching_photoresist.pdf.

[116] S. Cargou, "Soft lithography: Glass/PDMS bonding," *Elveflow*, Dec. 14, 2020. [Online]. Available: https://www.elveflow.com/microfluidic-reviews/soft-lithography-glass-pdms-bonding/.

A

Justification Thermal Noise

Here follows the justification for taking the thermal noise as white noise along the frequency range of interest, based on the circuit in 2.1. It is referred to from Subsection 2.1.2.

Under the assumption that the output resistance is much larger than the source or electrode resistance and that the counter electrode has a very large surface so that its impedance is negligible, analyzing the transfer function circuit in Figure 2.1 yields

$$H(j\omega) = \frac{V_o}{V_s} = \frac{R_o}{Z_{total}} = \frac{j\omega C_{WE} R_o}{j\omega C_{WE} R_o + 1} \quad R_o >> R_s + R_{RE} \tag{A.1}$$

where $H(j\omega)$ is the transfer function, R_o the output resistance, Z_{total} the total impedance, and ω the radial frequency. Calculating the volumetric capacitance of a circular PEDOT:PSS electrode with a diameter of $20\mu m$ and a thickness of $30\mu m$, the electrode capacitance is

$$C_{CE} = C^* 2\pi r^2 h = (39 F cm^{-3})(2\pi(10^{-3} cm)^2)(300 \cdot 10^{-7} cm) = 7.4 nF \tag{A.2}$$

where C^* is the constant volumetric capacitance of PEDOT:PSS, r the electrode radius, and h the electrode layer thickness. The transfer function is a high-pass filter and by taking $R_o = 10^{12}\Omega$, the corner frequency can be computed by

$$f_{-3dB} = \frac{1}{2\pi R_o C_{WE}} = \frac{1}{2\pi(10^{12})(7.4 \cdot 10^{-9})} = 2.2 \cdot 10^{-5} Hz \tag{A.3}$$

Since the corner frequency is below the minimal frequency of interest $0.1Hz$, the thermal noise is approached as white noise in the frequency range of interest. $\frac{k_B T}{C}$ noise is not applicable.

B

Supporting images

B.1. Blue color of PEDOT:PSS samples

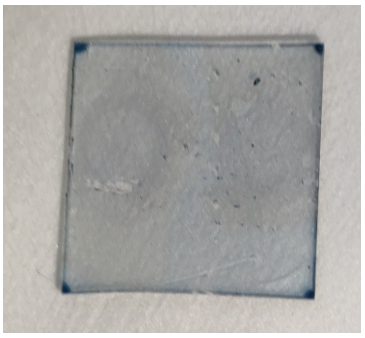

Figure B.1: Outside the cleanroom, thin PEDOT:PSS layers show a faint blue color.

B.2. FIB-SEM images of PEDOT:PSS on PDMS

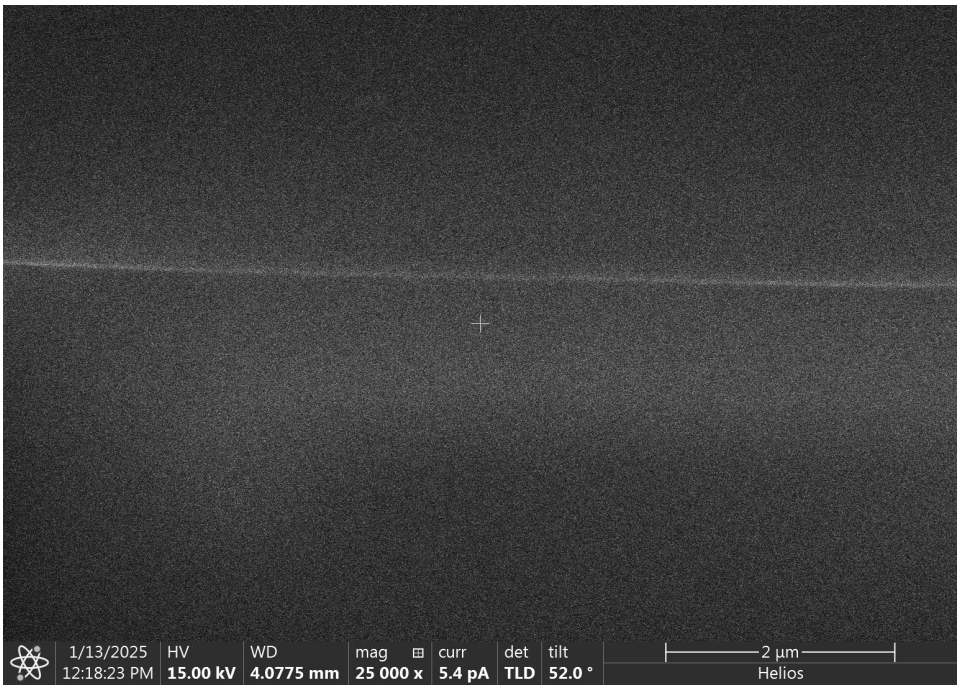

Figure B.2: A FIB-SEM picture taken of the spin coated PDMS with PEDOT:PSS on top. A faint layer of ≈ 100nm thick can be observed, but nothing definitive could be concluded from it.

C

Charge storage capacity calculation

The charge storage capacity can be calculated from a cyclic voltammetry diagram and indicates the charge an electrode material can store per unit area. It is obtained by integrating the current from the cathodic phase as

$$CSC = \int_{0.4}^{-0.4} i(V)dV \mid_{\frac{dV}{dt}=0.1V/s} \tag{C.1}$$

D
Patterns

D.1. 4-inch wafer pattern

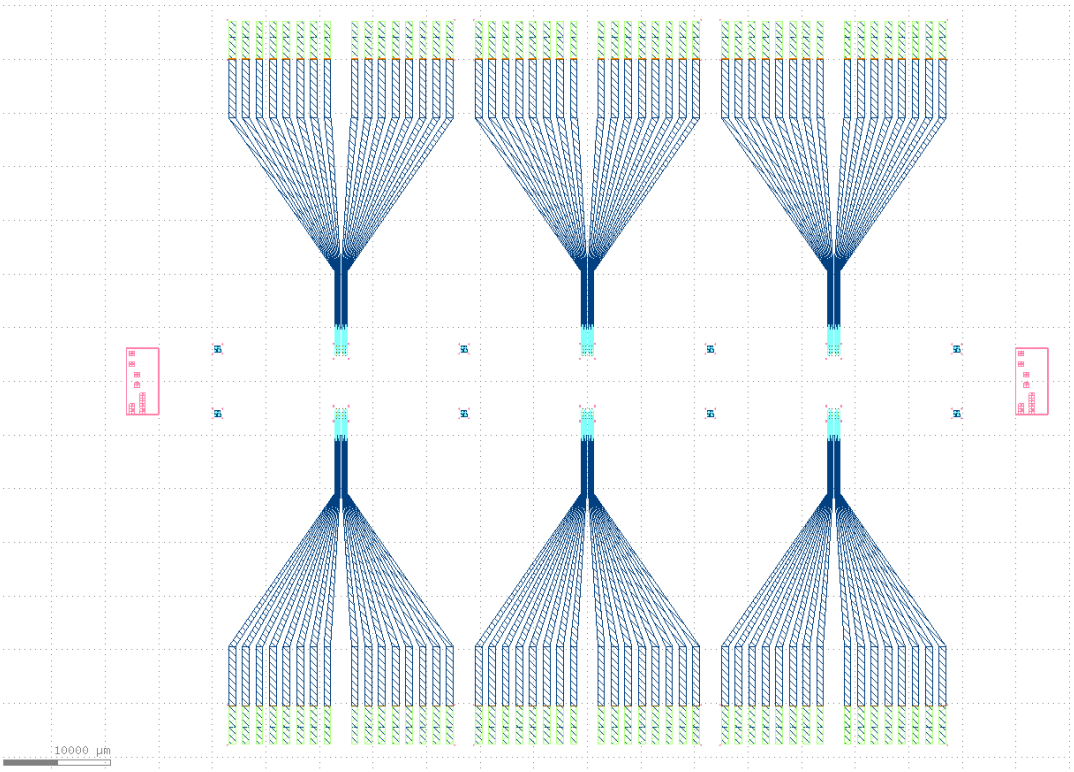

Figure D.1: The lithography pattern for a 4-inch wafer.

E

Recipes

E.1. Bilayer photoresist

1. Perform a dehydration bake at 150°C for 10 minutes.
2. Expose the wafer to HMDS vapor at 150°C for 1 minute and 30 seconds.
3. Spin coat LOR5B (unfiltered) at 4000 rpm for 55 seconds.
4. Bake the wafer on a hotplate at 230^{c}ircC for 5 minutes.
5. Spin coat AZ ECL3007 at 4000 rpm for 55 seconds.
6. Soft bake the wafer at 100°C for 1 minute.
7. Expose with the μMLA at a dose of 200 mJ/cm^2.
8. Post-exposure bake at 110°C for 1 minute and 30 seconds.
9. Develop with AZ 726MIF for 45 seconds.

E.2. Grey-scale lithography

1. Perform a dehydration bake at 150°C for 10 minutes.
2. Expose the wafer to HMDS vapor at 150°C for 1 minute and 30 seconds.
3. Spin coat AZNLOF2070 (unfiltered) at 2000 rpm for 55 seconds.
4. Soft bake at 100°C for 10 minutes.
5. Expose with the MLA 150 following the values in Table 4.1. Exposure dose is 700mJ/cm^2 and defocus is -21.
6. Post-exposure bake at 110°C for 1 minute and 30 seconds.
7. Develop with AZ726MIF for 14 minutes.
8. Rinse in DI water for 2 minutes.
9. Dry the wafer by spinning at 2000 rpm for 1 minute and 30 seconds.

E.3. PEDOT:PSS patterning

1. Perform a dehydration bake at 110°C for 10 minutes.
2. Expose the wafer to HMDS vapor at 110°C for 1 minute and 30 seconds.
3. Spin coat AZNLOF2020 (filtered with a 0.45μm-PTFE filter) at 4000 rpm for 55 seconds.
4. Soft bake at 100°C for 1 minute and 30 seconds.
5. Expose with the MLA 150 with dose 150 mJ/cm^2 and defocus -6. Focus mode was pneumatic, since optical failed.
6. Post-exposure bake at 110°C for 2 minutes and 15 seconds.
7. Develop in AZ726MIF for 2 minutes and 30 seconds.
8. Rinse in DI water for 2 minutes.
9. Dry the wafer by spinning at 2000 rpm for 1 minute and 30 seconds.
10. Inspect patterning under a microscope
11. Perform RIE O_2 with the F2 Sentech for 30 seconds.
12. Strip photoresist with DMSO at 80°C for 2.5 hours.

E.4. Au patterning

1. Perform a dehydration bake at 110°C for 10 minutes.
2. Spin coat AZNLOF2020 (filtered with a 0.45μm-PTFE filter) at 4000 rpm for 55 seconds.
3. Soft bake at 100°C for 1 minute and 30 seconds.
4. Expose with the MLA 150 with dose 150 mJ/cm^2 and defocus -6. Focus mode was pneumatic, since optical failed.
5. Post-exposure bake at 110°C for 2 minutes and 15 seconds.
6. Develop in AZ726MIF for 2 minutes and 30 seconds.
7. Rinse in DI water for 2 minutes.
8. Dry the wafer by spinning at 2000 rpm for 1 minute and 30 seconds.
9. Evaporate Ti/Au 10nm/100nm with an e-beam evaporator.
10. Lift-off in DMSO at 80° for 2.5 hours.

F

Oxygen plasma treatment PDMS

F.1. Cracking

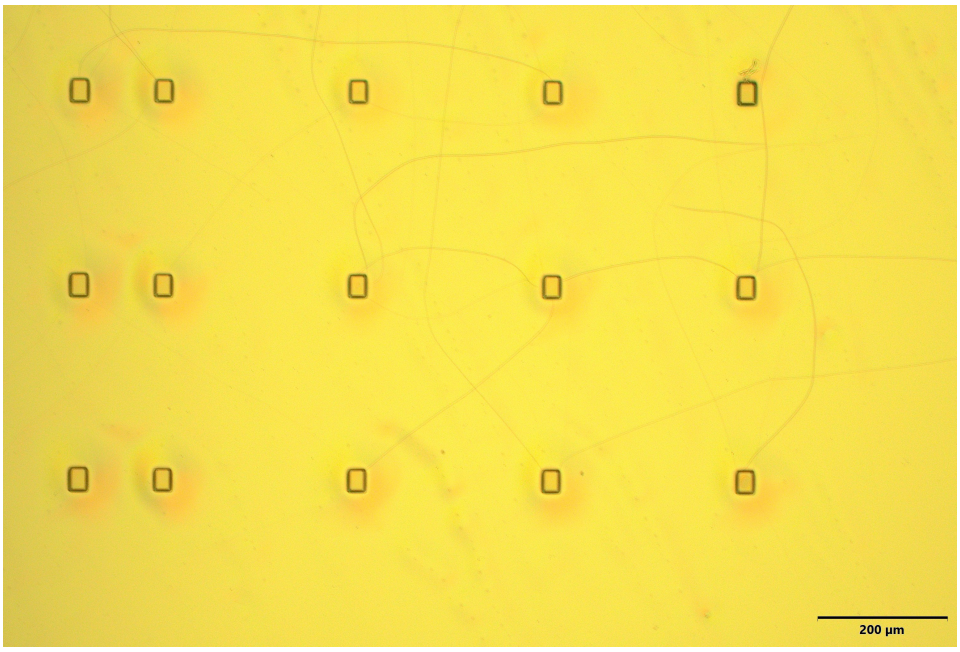

Figure F.1: Cracking behavior of PDMS after high power (>70W) O_2 plasma treatment.

Polymeric Microelectrode Array

Flow chart

David van der Laan

Run number:

Process engineer: David van der Laan

Mentor: Mustafeez Shah

Start: April 2025

Contamination: Yes

Labs: Polymer, Lithography, CR10000

EKL (Else Kooi Laboratory)

DELFT UNIVERSITY OF TECHNOLOGY

Address Feldmannweg 17, 2628 CT Delft,
P.O. 5053, 2600 GB Delft, The
Phone +31 - (0)15 - 2783868
Fax : +31 - (0)15 - 2622163
Website http://ekl.tudelft.nl/EKL/Home.php

PART 0: STARTING MATERIAL

Use **P-type silicon wafers** from EKL cleanroom

Type:	P
Orientation:	100
Resistivity:	NA
Thickness:	525 μm
Diameter:	100.0 mm

PROCESS DESCRIPTION

The aim is to create an all-polymeric microelectrode array, consisting of PEDOT:PSS, PDMS, and gold contact pads. A silicondioxide layer is grown and PDMS is patterned using photoresist micropillars with an anti-adhesive layer between PDMS and SiO2. PEDOT:PSS/GOPS is spin coated as interconnect layer and has strong adhesion to PDMS. PEDOT:PSS/GOPS is etched with O2 RIE. Another lithography step is needed for patterning Au using lift-off. Another PDMS layer is spin coated on top, after which the device is peeled off.

The process is schematically shown below.

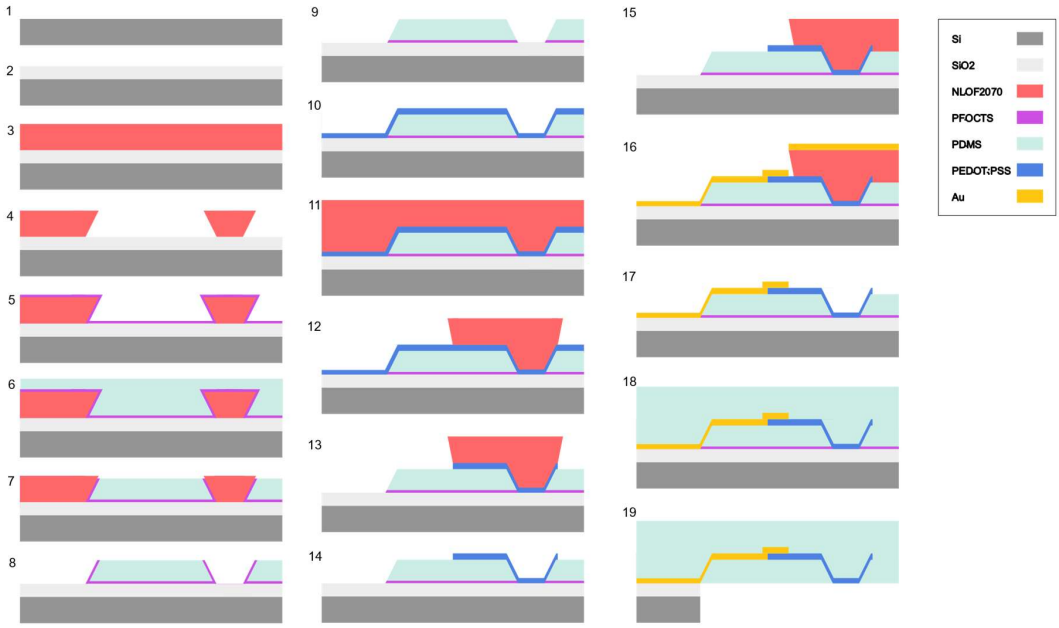

The process consists of 36 steps:

Step	Description	Location / Device
1	Clean wafers	HNO3 99% Green/Red wet bench
2	Thermal oxidation	Tempress
3	Treat with HMDS	HMDS station
4	Spin coat bilayer photoresist	Kavli – Wet bench
5	Expose photoresist	Kavli – LW MLA 150
6	Develop photoresist	Kavli – Wet bench
7	Evaporate Ti/Al	CHA std.
8	Lift off	EKL 10k Wet benches
9	Treat with HMDS	HMDS station
10	Spin coat photoresist	Kavli – Wet bench
11	Expose photoresist	Kavli – LW MLA 150
12	Develop photoresist	Kavli – Wet bench
13	PFOTCS treatment	Poly 2 fume hood
14	Prepare PDMS	PDMS fume hood – Polymer lab
15	Spin coat PDMS	Poly 2 fume hood
16	O2 RIE etch PDMS	AMS 110
17	Remove photoresist	EKL 10k Wet benches
18	Prepare PEDOT:PSS/GOPS	Poly 3 fume hood
19	O2 treatment	Diener Atto
20	Spin coat PEDOT:PSS/GOPS	Poly 2 fume hood
21	Treat with HMDS	HMDS station
22	Spin coat photoresist	Poly 1
23	Expose photoresist	SUSS Microtec
24	Develop photoresist	Poly 3
25	O2 etching PEDOT:PSS	AMS 110
26	Remove photoresist	EKL 10k Wet benches
27	Treat with HMDS	HMDS station
28	Spin coat photoresist	Poly 1
29	Expose photoresist	SUSS Microtec
30	Develop photoresist	Poly 3
31	O2 plasma treatment	Diener Atto
32	Evaporate Ti/Au	CHA std.
33	Lift off	CR10k wet bench / chemical area
34	Prepare PDMS	PDMS fume hood – Polymer lab
35	Spin coat PDMS	Poly 2 fume hood
36	Peel off device	Polymer lab

PART 1: CLEANING

1. CLEAN WAFERS

Silicon can be cleaned with the GREEN wet benches.

a. 10 minutes in fuming nitric acid (Merck: HNO3 99% green) at ambient temperature. Use wet bench "HNO3 (99%) ".
b. QDR: Rinse in the Quick Dump Rinser using the correct chuck (no CU/CU) with the standard program until the resistivity is 5 MΩ. Use the Semitool "rinser/dryer" with the standard program.

2. THERMAL OXIDATION

a. Open the Tempress accordingly. Wait till the holder is fully extracted.
b. Load the wafers on the holder.
c. Select oxidation parameters (only duration) and start the process.
d. When the process is done, let the Tempress unload and take out the wafers. Put the Tempress in standby.

PART 2: ALIGNMENT MARKERS

3. TREAT WITH HMDS

a. Put the wafer in the machine and perform a dehydration bake at 150C for 10 minutes.
b. Initialize the system and open the HMDS valve.
c. Run process number 3 two times (total of 1m30s).
d. Take out the wafer.

4. SPIN COAT PHOTORESIST

a. Set up a contaminated hot plate and monitor the temperature of the carrier using the contaminated thermometer. Take a chuck and prepare the spin coater.
b. Take LOR5b from the cupboard and pour it into a plastic cup. Clean the bottle with a tissue if needed. Place the LOR5b bottle back into the cupboard.
c. Center the wafer on the chuck. Check if it is centered and if the vacuum works well. Perform a test run to see if the spin coater functions correctly.
d. Apply the LOR5b and spin coat at 4000 rpm.
e. Put the wafer on the hotplate and soft bake at 230C for 5 minutes. After the soft bake, let it cool and place it in the wafer box.
f. Clean the spin coater and the chuck thoroughly with special cleaning solution for LOR5b.
g. Spin coat AZ ECL3007 at 4000 rpm.
h. Soft bake at 100C for 1 minute.
i. Clean the spin coater and the chuck thoroughly with acetone.

5. EXPOSE PHOTORESIST

a. Start the exposure wizard of the MLA 150. Set correct parameters.
b. Convert the correct design and load it.
c. Load the wafer and position it with the aid tool.
d. Wait till focusing is done. Perform alignment.

e. Set the exposure parameters and start exposure.
f. After exposure, unload the wafer.
g. Fill in the logbook.

6. DEVELOP PHOTORESIST

a. Perform a post-exposure bake at 110C for 1m30s.
b. Take glass beakers from the Wet bench area and write AZ726MIF and H2O on them with your name.
c. Pour AZ726MIF into the beaker and fill the other beaker with DI water.
d. Place the wafer in AZ726MIF for 45 seconds.
e. Put the wafer in the DI water for 2 minutes.
f. Spin dry the wafer for 1m30s and put it in the wafer box.
g. Clean up the glass beakers accordingly.

7. EVAPORATE ALUMINUM

a. Turn on the CHA solutions according to the manual.
b. After the system is turned on, vent the vacuum chamber to load your samples.
c. Ensure the clean shutters are in place (check the label). Ask the device owner to replace the shutters if needed. Check the clean dome and replace it yourself if needed.
d. Check the crystal lifetime and notate it in the logbook. Check the pockets and ensure the materials are as required.
e. Select the correct recipe to deposit 10nm/100nm Ti/Al. Pump down the system.
f. Start the deposition. During deposition, remain with the machine to monitor the chamber temperature and the process.
g. After deposition, vent the system. Remove the samples, make sure the chamber is sufficiently clean. After closing the system, pump down.
h. Turn off the system according to the manual.

8. LIFT OFF

a. Pour DMSO in an envelope beaker.
b. Place the wafer in the beaker with a wafer holder
c. Place the beaker in a bain-Marie bath at 80C.
d. Place the wafer in DI water for 10 minutes after all resist has come off.
e. Spin dry the wafer at 2000 rpm for 1m30s.
f. Pour the DMSO in an organic waste container.
g. Clean the beaker thoroughly using DI water. Blow dry with N2 and place in the dirty glassware cabinet.

PART 3: PATTERN PDMS LAYER

9. TREAT WITH HMDS

a. Put the wafer in the machine and perform a dehydration bake at 150C for 10 minutes.
b. Initialize the system and open the HMDS valve.
c. Run process number 3 two times (total of 1m30s).

d. Take out the wafer.

10. SPIN COAT PHOTORESIST

a. Set up a contaminated hot plate and monitor the temperature of the carrier using the contaminated thermometer. Take a chuck and prepare the spin coater.
b. Take AZNLOF2070 from the cupboard and pour it into a plastic cup. Clean the bottle with a tissue if needed. Place the AZNLOF2070 bottle back into the cupboard.
c. Center the wafer on the chuck. Check if it is centered and if the vacuum works well. Perform a test run to see if the spin coater functions correctly.
d. Apply the AZNLOF2070 and spin coat at 2000 rpm.
e. Put the wafer on the hotplate and soft bake at 110C for 10 minutes. After the soft bake, let it cool and place it in the wafer box.
f. Clean the spin coater and the chuck thoroughly with acetone.

11. EXPOSE PHOTORESIST

a. Start the exposure wizard of the MLA 150. Set correct parameters.
b. Convert the correct design and load it.
c. Load the wafer and position it with the aid tool.
d. Wait till focusing is done. Perform alignment.
e. Set the exposure parameters and start exposure.
f. After exposure, unload the wafer.
g. Fill in the logbook.

12. DEVELOP PHOTORESIST

a. Perform a post-exposure bake at 110C for 1m30s.
b. Take glass beakers from the Wet bench area and write AZ726MIF and H2O on them with your name.
c. Pour AZ726MIF into the beaker and fill the other beaker with DI water.
d. Place the wafer in AZ726MIF for 14 minutes
e. Put the wafer in the DI water for 2 minutes.
f. Spin dry the wafer for 1m30s and put it in the wafer box.
g. Clean up the glass beakers accordingly

13. TREAT WITH PFOTCS

a. Load the wafer into a vacuum chamber.
b. Take out PFOTCS (handle carefully!) and put three drops into the holder in the vacuum chamber.
c. Pump down the vacuum chamber and check whether PFOTCS evaporates.
d. Clean up the fume hood and seal the waste in a CMR bag.

14. PREPARE PDMS

a. Mix Sylgard 184 Base and Sylgard 184 Curing agent (located in chemical storage cupboard 17 ORG) in a 10:1 ratio by weight in a plastic bottle.
b. Place in ARE-250 CE and mix for 2 minutes.

15. SPIN COAT PDMS

a. Cover the manual spinner with aluminum foil all around the spinning area.

b. Use the contaminated chuck. Dispense PDMS on glass wafer (5 ml).
c. Perform spin-coating at 1000 rpm for 240 seconds. Acceleration 300 rpm/s.
d. Check the chuck after each wafer and, if necessary, clean it with acetone followed by IPA
e. Dispose all waste in the designated organic waste bin with exhaust.
f. Clean the poly-2 thoroughly (especially the chuck). Use IPA to clean mixer holders and the PDMS kit bottles. Everything needs to be clean.
g. Degas in vacuum chamber for 120 min. Leave a note to inform other users.
h. Bake 90°C – 60 min in the Salvis Vacuum oven.
i. Insert the wafers in the MEMMERT oven and bake (time and temperature specified on datasheet).

16. SF6 REACTIVE ION ETCH PDMS

a. Check the status and temperature. Load the wafer in the AMS110.
b. Edit the recipe ETCH step – PDMS.
c. Set the time to 10 minutes.
d. Start etching process and monitor it.
e. Unload the wafer.

17. REMOVE PHOTORESIST

a. Pour DMSO in an envelope beaker.
b. Place the wafer in the beaker with a wafer holder
c. Place the beaker in a bain-Marie bath at 80C.
d. Place the wafer in DI water for 10 minutes after all resist has come off.
e. Spin dry the wafer at 2000 rpm for 1m30s.
f. Pour the DMSO in an organic waste container.
g. Clean the beaker thoroughly using DI water. Blow dry with N2 and place in the dirty glassware cabinet.

PART 4: PATTERN PEDOT:PSS

18. PREPARE PEDOT:PSS

a. PEDOT:PSS (Clevious PH1000) solution is prepared in the Poly 3 fume hood. The bottle containing PEDOT:PSS is taken from the fridge near the HMDS Vapor station to the fume hood.
b. 5 mL per wafer is pipetted into a 60 mL plastic beaker.
c. Ethylene glycol is added using a pipette (5% v/v) and DBSA is added (0.5% m/m)
d. The mixture is mixed and degassed in the Thinky ARE-250 at 2000 rpm for 2 min.
e. GOPS is added (1% v/v).
f. The mixture is again mixed and degassed in the Thinky ARE-250 with same settings.

19. TREAT WITH OXYGEN PLASMA

a. Load the wafers on the glass boat of the Diener Atto.
b. Gently open the door, insert the boat with wafers, and gently close the door.
c. Select the correct program. Ensure the SCCM and power are correctly set. Press start and wait till it is finished.
d. Open the door and take out the wafers. Gently close the door.

20. SPIN COAT PEDOT:PSS

a. Check the organic waste bin under the spin coater before starting. Prepare the spin coater. Use the contaminated chuck. Set up a contaminated hot plate and monitor the temperature of the carrier using the contaminated thermometer.
b. Center the wafer on the chuck. Check if it is centered and if the vacuum works well. Perform a test run to see if the spin coater functions correctly.
c. Take the PEDOT:PSS mixture. Use a syringe and 0.45um-PTFE filter to apply PEDOT:PSS on the wafer.
d. Spin coat at 2000 rpm for 1 minute.
e. Put the wafer on the hotplate and soft bake at 110C for 1 minute. Then hard bake the layer in the oven (Memmert) at 110C for 1 hour. After the hard bake, let it cool and place it in the wafer box.
f. Clean the spin coater and the chuck thoroughly with water.

21. TREAT WITH HMDS

a. Put the wafer in the machine and perform a dehydration bake at 150C for 10 minutes.
b. Initialize the system and open the HMDS valve.
c. Run process number 3 two times (total of 1m30s).
d. Take out the wafer.

22. SPIN COAT PHOTORESIST

a. Set up a contaminated hot plate and monitor the temperature of the carrier using the contaminated thermometer. Take a chuck and prepare the spin coater.
b. Take NLOF2020 from the cupboard and pour it into a plastic cup. Clean the bottle with a tissue if needed. Place the AZNLOF2020 bottle back into the cupboard.
c. Center the wafer on the chuck. Check if it is centered and if the vacuum works well. Perform a test run to see if the spin coater functions correctly.
d. Apply the NLOF2020 after filtering with a 0.45um-PTFE filter and spin coat at 4000 rpm.
e. Put the wafer on the hotplate and soft bake at 100C for 2m15s. After the soft bake, let it cool and place it in the wafer box.
f. Clean the spin coater and the chuck thoroughly with acetone.

23. EXPOSE PHOTORESIST

a. Start the exposure wizard of the MLA 150. Set correct parameters.
b. Convert the correct design and load it.
c. Load the wafer and position it with the aid tool.
d. Wait till focusing is done. Perform alignment.
e. Set the exposure parameters and start exposure.
f. After exposure, unload the wafer.
g. Fill in the logbook.

24. DEVELOP PHOTORESIST

a. Perform a post-exposure bake at 110C for 1m30s.
b. Take glass beakers from the Wet bench area and write AZ726MIF and H2O on them with your name.
c. Pour AZ726MIF into the beaker and fill the other beaker with DI water.

d. Place the wafer in AZ726MIF for 2m30s.
e. Put the wafer in the DI water for 2 minutes.
f. Spin dry the wafer for 1m30s and put it in the wafer box.
g. Clean up the glass beakers accordingly.

25. O2 REACTIVE ION ETCH PEDOT:PSS

a. Check if the F2 Sentech has completed a pumpdown.
b. Vent the chamber.
c. Load the wafer.
d. Pumpdown the chamber.
e. Select the O2 clean recipe and run for 30 seconds.
f. Vent the system after etching is completed and unload the wafer.
g. Run the O2 clean step for 15 minutes.

26. REMOVE PHOTORESIST

a. Pour DMSO in an envelope beaker.
b. Place the wafer in the beaker with a wafer holder
c. Place the beaker in a bain-Marie bath at 80C.
d. Place the wafer in DI water for 10 minutes after all resist has come off.
e. Spin dry the wafer at 2000 rpm for 1m30s.
f. Pour the DMSO in an organic waste container.
g. Clean the beaker thoroughly using DI water. Blow dry with N2 and place in the dirty glassware cabinet.

PART 5: GOLD LAYER

27. TREAT WITH HMDS

a. Put the wafer in the machine and perform a dehydration bake at 150C for 10 minutes.
b. Initialize the system and open the HMDS valve.
c. Run process number 3 two times (total of 1m30s).
d. Take out the wafer.

28. SPIN COAT PHOTORESIST

a. Set up a contaminated hot plate and monitor the temperature of the carrier using the contaminated thermometer. Take a chuck and prepare the spin coater.
b. Take NLOF2020 from the cupboard and pour it into a plastic cup. Clean the bottle with a tissue if needed. Place the AZNLOF2020 bottle back into the cupboard.
c. Center the wafer on the chuck. Check if it is centered and if the vacuum works well. Perform a test run to see if the spin coater functions correctly.
d. Apply the NLOF2020 after filtering with a 0.45um-PTFE filter and spin coat at 4000 rpm.
e. Put the wafer on the hotplate and soft bake at 100C for 2m15s. After the soft bake, let it cool and place it in the wafer box.
f. Clean the spin coater and the chuck thoroughly with acetone.

29. EXPOSE PHOTORESIST

a. Start the exposure wizard of the MLA 150. Set correct parameters.
b. Convert the correct design and load it.
c. Load the wafer and position it with the aid tool.
d. Wait till focusing is done. Perform alignment.
e. Set the exposure parameters and start exposure.
f. After exposure, unload the wafer.
g. Fill in the logbook.

30. DEVELOP PHOTORESIST

a. Perform a post-exposure bake at 110C for 1m30s.
b. Take glass beakers from the Wet bench area and write AZ726MIF and H2O on them with your name.
c. Pour AZ726MIF into the beaker and fill the other beaker with DI water.
d. Place the wafer in AZ726MIF for 2m30s.
e. Put the wafer in the DI water for 2 minutes.
f. Spin dry the wafer for 1m30s and put it in the wafer box.
g. Clean up the glass beakers accordingly.

31. TREAT WITH OXYGEN PLASMA

a. Load the wafers on the glass boat of the Diener Atto.
b. Gently open the door, insert the boat with wafers, and gently close the door.
c. Select the correct program. Ensure the SCCM and power are correctly set. Press start and wait till it is finished.
d. Open the door and take out the wafers. Gently close the door.

32. EVAPORATE GOLD

a. Turn on the CHA solutions according to the manual.
b. After the system is turned on, vent the vacuum chamber to load your samples.
c. Ensure the clean shutters are in place (check the label). Ask the device owner to replace the shutters if needed. Check the clean dome and replace it yourself if needed.
d. Check the crystal lifetime and notate it in the logbook. Check the pockets and ensure the materials are as required.
e. Select the correct recipe to deposit 10nm/100nm Ti/Au. Pump down the system.
f. Start the deposition. During deposition, remain with the machine to monitor the chamber temperature and the process.
g. After deposition, vent the system. Remove the samples, make sure the chamber is sufficiently clean. After closing the system, pump down.
h. Turn off the system according to the manual.

33. LIFT OFF

a. Pour DMSO in an envelope beaker.
b. Place the wafer in the beaker with a wafer holder
c. Place the beaker in a bain-Marie bath at 80C.
d. Place the wafer in DI water for 10 minutes after all resist has come off.

e. Spin dry the wafer at 2000 rpm for 1m30s.
f. Pour the DMSO in an organic waste container.
g. Clean the beaker thoroughly using DI water. Blow dry with N2 and place in the dirty glassware cabinet.

34. PREPARE PDMS

c. Mix Sylgard 184 Base and Sylgard 184 Curing agent (located in chemical storage cupboard 17 ORG) in a 10:1 ratio by weight in a plastic bottle.
d. Place in ARE-250 CE and mix for 2 minutes.

35. SPIN COAT PDMS

j. Cover the manual spinner with aluminum foil all around the spinning area.
k. Use the contaminated chuck. Dispense PDMS on glass wafer (5 ml).
l. Perform spin-coating at 1000 rpm for 240 seconds. Acceleration 300 rpm/s.
m. Check the chuck after each wafer and, if necessary, clean it with acetone followed by IPA .
n. Dispose all waste in the designated organic waste bin with exhaust.
o. Clean the poly-2 thoroughly (especially the chuck). Use acetone to clean mixer holders and the PDMS kit bottles. Everything needs to be clean.
p. Degas in vacuum chamber for 120 min. Leave a note to inform other users.
q. Remove PDMS on the connection pads using a swab with acetone.
r. Bake 90°C – 60 min in the Salvis Vacuum oven.
s. Insert the wafers in the MEMMERT oven and bake (time and temperature specified on datasheet).

36. PEEL-OFF DEVICE

e. Using a razor blade, cut out a shape around the device.
f. Solder the Omnetics connector to the connection pads.
g. Using tweezers, carefully peel off the PDMS substrate.